University of Groningen

Ultra-high-resolution quantitative multi-pinhole small-animal SPECT

Wu, Chao

IMPORTANT NOTE: You are advised to consult the publisher's version (publisher's PDF) if you wish to cite from it. Please check the document version below.

Document Version
Publisher's PDF, also known as Version of record

Publication date:
2013

Link to publication in University of Groningen/UMCG research database

Citation for published version (APA):
Wu, C. (2013). *Ultra-high-resolution quantitative multi-pinhole small-animal SPECT*. s.n.

Copyright
Other than for strictly personal use, it is not permitted to download or to forward/distribute the text or part of it without the consent of the author(s) and/or copyright holder(s), unless the work is under an open content license (like Creative Commons).

The publication may also be distributed here under the terms of Article 25fa of the Dutch Copyright Act, indicated by the “Taverne” license. More information can be found on the University of Groningen website: https://www.rug.nl/library/open-access/self-archiving-pure/taverne-amendment.

Take-down policy
If you believe that this document breaches copyright please contact us providing details, and we will remove access to the work immediately and investigate your claim.

Downloaded from the University of Groningen/UMCG research database (Pure): http://www.rug.nl/research/portal. For technical reasons the number of authors shown on this cover page is limited to 10 maximum.

Download date: 05-05-2023

Ultra-High-Resolution Quantitative Multi-Pinhole Small-Animal SPECT

Chao Wu

The printing of this thesis was financially supported by Graduate School of Medical Sciences, University Medical Center Groningen, University of Groningen and MILabs B.V.

Cover image: SPECT/CT image of a rat with radioactive sources
Feynman diagram for Compton scattering
Cover design: C. Wu, O. Ivashchenko, F. J. Beekman

Printed by: Proefschriftmaken.nl || Uitgeverij BOXPress

ISBN: 978-90-367-6357-8

RIJKSUNIVERSITEIT GRONINGEN

Ultra-High-Resolution Quantitative Multi-Pinhole Small-Animal SPECT

Proefschrift

ter verkrijging van het doctoraat in de
Medische Wetenschappen
aan de Rijksuniversiteit Groningen
op gezag van de
Rector Magnificus, dr. E. Sterken,
in het openbaar te verdedigen op
woensdag 11 september 2013
om 12.45 uur

door

Chao Wu

geboren op 9 februari 1982
te Yichang, China

Promotores:	Prof.dr. F.J. Beekman Prof.dr. R.A.J.O. Dierckx
Copromotor:	Dr. J.R. de Jong
Beoordelingscommissie:	Prof.dr. A.M.J. Paans Prof.dr. R. Boellaard Prof.dr. M. de Jong

ISBN: 978-90-367-6357-8

Content

Chapter I

General introduction

Today, single-photon emission computed tomography (SPECT) is one of the most applied clinical imaging techniques. It allows imaging the dynamic 3-D distribution of radiolabelled molecules (“tracers”) in vivo, thus offering the possibility to characterize pathological and functional properties of organs and tissues non-invasively and longitudinally [1, 2]. The radionuclides used in SPECT tracers usually allow long-distance transportation from the production site (most times a reactor) to hospitals and research centres, and relatively long-time storage in contrast with most positron emission tomography (PET) tracers. As a result, many common SPECT tracers are now commercially available. PET usually requires a costly on-site cyclotron and associated personnel to produce the most often used positron-emitting tracers. (Nevertheless, for a subset of applications, a few PET tracers labelled with long-lived isotopes such as ^{89}Zr are also available.)

In addition to clinical SPECT, pre-clinical SPECT (for imaging of laboratory animals) plays an increasingly important role in biomedical research [3–7]. In order to e.g. study models of human disease in small animals—usually rodents—novel SPECT devices with ultra-high resolution are required, to obtain sufficient detail in the small target organs. In most small-animal SPECT systems, the high spatial resolution is achieved by using pinhole collimation [8–13]. Although the principles of pinhole camera and pinhole magnification are quite simple and well known, many different technologies need to be developed in order to obtain high-resolution 3D and 4D images based on pinhole SPECT.

1.1 Pinhole imaging

Photons travel in straight lines, thus an inverted image of the illuminated field-of-view (FOV) is produced when photons are passing through a pinhole. This effect has been mentioned for the first time in *Mozi*, the philosophical text compiled by Mohists in ancient China in the 5th century BCE. In the 9th century CE, during the Tang Dynasty, the image of an inverted Chinese pagoda is mentioned in Duan Chengshi’s book *Miscellaneous Morsels from Youyang*. Later, the Song Dynasty Chinese scientist Shen Kuo experimented with camera obscura in the 11th century and was the first to establish its geometrical and quantitative attributes [14]. Similar discoveries were also made in the West and the Middle East, by Aristotle, Euclid, Ibn al-Haytham, Robert Grosseteste, Roger Bacon, Leonardo da Vinci, Gemma Frisius, Giambattista della Porta and so on [15–19]. After that, the pinhole technique was tried several times by photographers such as Sir William Crookes and William de Wiveleslie Abney; Sir David Brewster, a Scottish scientist, took the first photograph with a pinhole camera in 1850 [20]. Actually, pinhole cameras are not only used by scientists, photographers or artists. Pinhole imaging is a common phenomenon in nature, e.g. through holes in the leaf canopy of trees. (Figure 1.1). More data about the history of pinholes and their occurrence in nature can be found in [13].

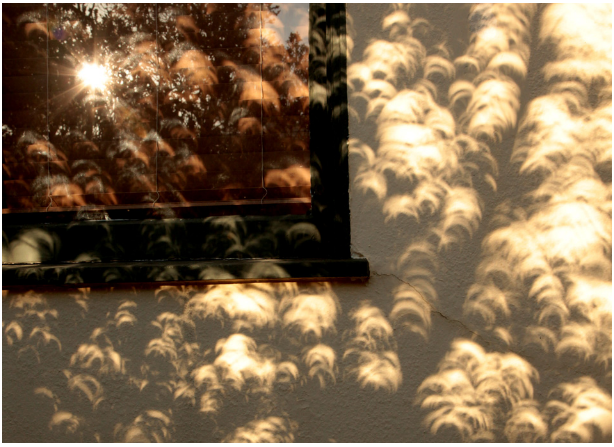

Figure 1.1 Images of a solar eclipse on a wall, projected through holes in leaf canopy. The sun and the leaves can be seen in the window reflection. (by torbakhopper, San Francisco, CA, USA, 20 May 2012)

The pinhole camera model has been studied thoroughly. One simple but important feature is that the image can be either magnified or de-magnified compared to the original object, depending on the ratio of the distance between pinhole and image plane to the distance between pinhole and object. This creates the opportunity to use pinhole cameras for the imaging of tiny objects and the obtaining of significantly magnified images showing many details. When interests are shifted from optical wavelengths to X-rays or gamma rays, pinhole cameras become a powerful tool in nuclear medicine.

A pinhole gamma camera shares a very similar structure with the optical pinhole camera. The film, CCD or CMOS sensor at the image plane in optical cameras is most often replaced by a scintillation crystal coupled on to a position-sensitive light detector

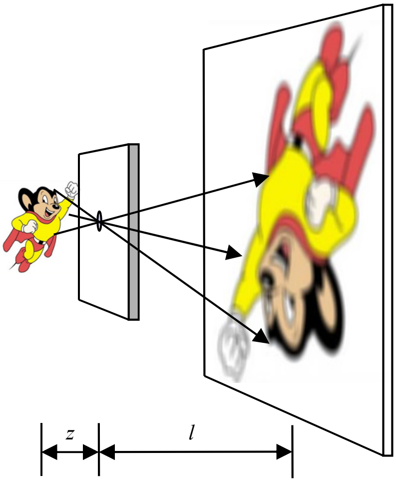

Figure 1.2 With pinhole camera, magnified projection suppresses information loss that is due to intrinsic camera blurring.

array. When a gamma photon hits the scintillation crystal, a light flash is produced and subsequently read out by the detectors. The position and energy of the gamma-photon interaction can be determined from the intensity and position of the light flash.

Pinhole collimators usually consist of a radiation-absorbing wall with one or more pinholes. While optical light can be blocked easily with a piece of thick paper, an absorbing wall for gamma rays must be made from materials with high atomic numbers, typically tungsten or lead.

When an object is imaged with a pinhole gamma camera, the projection can be magnified by a factor of l/z, in which z denotes the object-to-pinhole distance, and l the detector-to-pinhole distance. This is illustrated in Figure 1.2 as a very simple geometric relationship. If the intrinsic resolution of the gamma camera is R_i, then the equivalent resolution of the total system with an ideal pinhole projection becomes $(z/l)R_\mathrm{i}$. On the other hand, the resolution of a pinhole system with an ideal detector, which is also called the geometric resolution R_g, is described in (1.1):

$$R_\mathrm{g} \approx D\left(l+z\right)/l \qquad (1.1),$$

where D is the effective pinhole diameter that accounts for penetration of gamma rays through the pinhole edges. Therefore, the total system resolution R of a real pinhole gamma camera is approximately

$$R \approx \sqrt{\left(\frac{z}{l}R_\mathrm{i}\right)^2 + R_\mathrm{g}^2} \quad [13] \qquad (1.2).$$

1.2 Pinhole SPECT and image reconstruction

A 3-D volume of transaxial slices can be reconstructed from a set of 2-D projections. This technology is called “tomography”. At present, almost all dedicated small-animal SPECT systems use pinhole collimation, benefiting from the high resolution of pinhole gamma cameras [21–27]. Because a sufficient number of angular views are required for reconstructing a tomogram, a SPECT device usually contains a rotating component, either the animal bed or the detectors with collimators. There can be more than one camera in the system in order to obtain more projections at a single detector position, and in each camera there can be multiple pinholes to increase the number of gamma photons that pass through the collimator and to acquire more angular information with a single detector position. Besides rotation-based systems, there are also stationary systems. They often have multiple pinholes and detectors surrounding the object to acquire projections from all available angles simultaneously. The properties of such type of systems will be discussed in a following separate section.

According to the central slice theorem, 3-D image reconstruction from 2-D projections can be performed analytically based on Fourier transform [28]. A family of filtered-back-projection-like algorithms such as the Feldkamp algorithm [29] is derived from the theorem and widely used in different tomography systems. The main advantage of these analytical algorithms is their computational speed. However, they are usually sensitive to noise level, and can hardly compensate for image blurring effects on the detector and projection truncation. Moreover, the actual form of calculation is tightly related to the projection geometry of the systems. In pinhole SPECT, especially in multi-pinhole systems, the pinhole and detector placements are complicated and not fixed (i.e. the placement can be optimized differently for variable imaging tasks), but analytical methods generally lack flexibility to handle those different situations. Therefore, images of the majority of pinhole SPECT systems are reconstructed with statistical algorithms, such as the maximum likelihood expectation maximization (MLEM) [30] or its accelerated versions. These algorithms perform image reconstruction iteratively. The MLEM algorithm can incorporate models to compensate for different types of image degradation, such as pinhole and detector blurring, distant-dependent pinhole sensitivity and photon scatter. In addition, these statistical algorithms take the characteristics of the noise in the projections into account, which makes them more robust to image noise.

1.3 Statistical image reconstruction

A SPECT image system can be modelled as a linear transformation:

$$\boldsymbol{P} = \boldsymbol{M}\,\boldsymbol{V} \tag{1.3}$$

In this equation, $\boldsymbol{V}$ is an unknown vector of voxels that represent the discrete distribution of activity concentration in the object. $\boldsymbol{P}$ is the pixel vector of the projections that are acquired with the detectors. The transformation matrix $\boldsymbol{M}$ is usually called system matrix. A certain element m_{ij} of $\boldsymbol{M}$ models the system response from the j-th voxel to the i-th pixel, i.e. $P_i = m_{ij}\ V_j$. If we omit the effects of photon scattering and absorption within the object, the system matrix becomes object-independent, thus needs to be measured only once for each collimator and can be used for each reconstruction.

Solving the vector $\boldsymbol{V}$ in Equation (1.3) analytically is not an easy task or not even possible, since it actually contains hundreds of thousands of linear equations and unknowns, and the exact solution may not even exist in practice. The statistical reconstruction method, such as the MLEM algorithm, can solve the problem by means of iterative loops employing estimation–comparison–update, which is illustrated in Figure 1.3. At initialization, $\boldsymbol{V}$ can be simply set to be a non-zero constant vector or any other better estimation depending on the object imaged, denoted by $\boldsymbol{V}^{e}$. Then an estimated pixel vector $\boldsymbol{P}^{e}$ of the projection space is computed with the transformation $\boldsymbol{M}$ which simulates the projection process. $\boldsymbol{P}^{e}$ is compared with the real $\boldsymbol{P}$ of the measured projection. The difference of the comparison is back-projected to the object space as an error map and this map is subsequently used for updating the vector $\boldsymbol{V}^{e}$. With proper methods for the comparison and update, the difference between $\boldsymbol{P}^{e}$ and $\boldsymbol{P}$ can decrease during repetition of the loop, thus the error map for updating $\boldsymbol{V}^{e}$ becomes smaller. In situations of low noise and an accurate matrix, it is

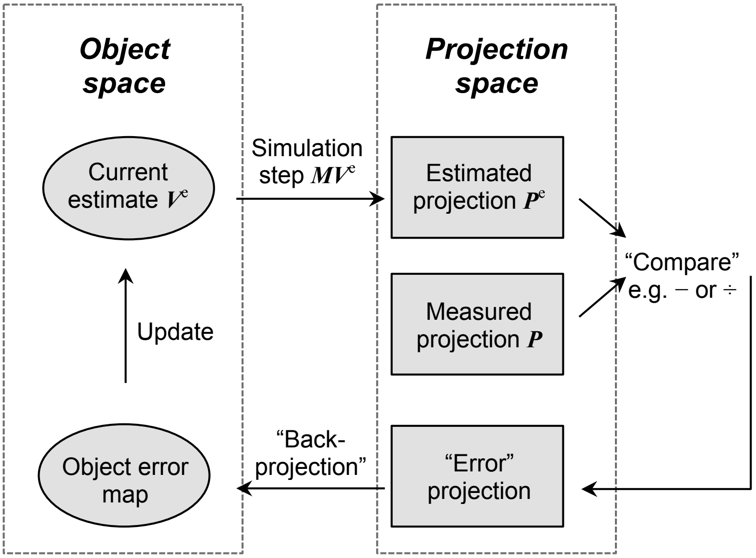

Figure 1.3 Scheme of iterative reconstruction. In MLEM or OSEM, division is used in the comparison step.

possible that at the end of the iterative process $\boldsymbol{P}^e$ is very close to $\boldsymbol{P}$. $\boldsymbol{V}^e$ is then a good estimation of $\boldsymbol{V}$, because they produce almost the same projections.

MLEM has been proven to converge to the tracer distribution that has maximum likelihood that is caused by the measured data, but the convergence rate is relatively low. Therefore, acceleration has been developed. A popular one is ordered subset expectation maximization (OSEM) [31]. It shares the same iterative loop as that used by MLEM, but in one loop the calculation is applied only to a subset of the projection data, and in the next loop the algorithm goes to another subset and so on. A complete update using all the projection data one time is defined as a single iteration of OSEM. It is easy to see that the amount of computation in one iteration of OSEM and MLEM are comparable, but with OSEM the estimated voxel values are updated as many times as there are N subsets, instead of only once with MLEM. Consequently, the OSEM algorithm is expected to be approximately N times as fast as MLEM.

Although OSEM can greatly speed up the reconstruction process, its convergence close to the maximum likelihood is not always guaranteed. In order to prevent inaccurate or divergent results, the segmentation of subsets must be carefully designed. The number of subsets N should be limited and the distribution of subsets should be "balanced", so that a photon emitted from a certain voxel can be detected in each subset with equal probabilities. A recently proposed method that improves realization of OSEM is pixel-based OSEM or POSEM [32], in which the pixels in each subset are spread out regularly over projections and are spatially separated as much as possible.

1.4 Stationary multi-pinhole SPECT

As described above, some pinhole SPECT devices contain rotating gantry or animal beds for acquiring angular projections, while others are stationary systems with multiple pinholes. In such stationary multi-pinhole systems, each pinhole and its corresponded detector surface form a mini pinhole gamma camera that samples the projection from one angle. To acquire sufficient angular projections without any rotation of the heavy detectors, there are usually a high number of pinholes spread around the object, which also provide a high sensitivity for the system. Moreover, the number of viewing angles can be increased by smart use of different bed positions [33].

Because the projections from all viewing angles at a single bed position are sampled simultaneously in stationary systems, the time of acquiring a complete data set for reconstructing a tomogram can be arbitrarily short, despite the noise level. Therefore, stationary systems are able to perform dynamic imaging with very short time frames, which is very important for assessing tracer and pharmaceutical kinetics in small animals.

Another advantage of stationary systems is that the mechanisms are inherently very stable over time. During acquisition, not hundreds of kilos of detectors are being rotated but only a small animal between about 10 and 500 grams is translated in a fraction of the time and with much more precision [33]. This also means relatively low expenses for maintenance, as compared with rotation-based systems.

U-SPECT-II (MILabs, Utrecht, the Netherlands) is a typical stationary multi-pinhole SPECT system. It has 75 pinholes on its cylindrical collimator that focus on a small area inside the collimator. For imaging larger volumes such as the total body of an animal, an XYZ stage shifts the animal bed during data acquisition, which is equivalent to moving the focused imaging area on the animal. The large volumes are reconstructed with all acquired data from all bed positions by means of a scan focus method (SFM) [33]. A detailed description of the U-SPECT-II system is given in [26] and will also be partly covered in following chapters.

A notable supplementary introduction to stationary multi-pinhole SPECT is that this technique can also be used for imaging the regional distribution of PET tracers if the collimator and pinhole apertures are designed to handle 511 keV photons. In this case, the photons created by annihilation are treated as single photons and traced not by line-of-response but by collimation [34]. Thanks to pinhole magnification, such "pinhole PET" (e.g. VECTor, MILabs, Utrecht, the Netherlands) can reach higher spatial resolution than traditional micro-PET systems, with a trade-off regarding the sensitivity and the size of the field-of-view that can be seen in a single bed position.

1.5 Applications of small-animal SPECT

Small-animal SPECT systems are capable of clarifying molecular interactions that are important for assessment of drug candidates and imaging agents, for investigation of disease progression, and for monitoring therapeutic effectiveness of pharmaceuticals in longitudinal studies.

Small-animal SPECT is able to perform cardiovascular imaging of rodents well. With ultra-high resolution and extremely fast acquisition speed of stationary pinhole systems, it is possible to perform gated imaging of tiny, fast-beating rodent hearts, which meets the basic requirements of cardiology studies in small animals and evaluation of new myocardial imaging agents in vivo [35].

Tumour imaging is another important application of small-animal SPECT. Imaging small-animal models of cancer can be used to investigate the interaction of a tumour with its microenvironment, monitor gene expression in a certain kind of tumour, and help to better define tumour volumes or identify sites of poor tissue oxygenation in radiation treatment plans [6].

Brain research can also benefit from small-animal SPECT. For instance, accurate imaging results could be provided by pinhole SPECT in studies of the dopaminergic system in mouse brain [36]. When combined with anatomic data such as MRI images, the functional SPECT images become particularly valuable for studying neural interactions in cerebral substructures.

1.6 Thesis outline

This thesis describes further development of quantitative multi-pinhole SPECT and some applications. First, a brief technical overview of small-animal SPECT and SPECT/CT systems is given in Chapter II, as well as a review of a list of applications in cardiovascular research. Chapter III focuses on myocardial perfusion imaging of mice with simultaneous cardiac and respiratory gating. This chapter shows heart images that were acquired with different gating schemes, different animal positioning, and filtered with different kernel sizes. The images and their derived cardiac parameters were compared.

In order to perform more accurate and complicated animal studies, quantitative small-animal SPECT images are required. An important issue in absolute quantification is attenuation correction, which is thoroughly discussed in Chapter IV and V. Chapter IV proposes an optical-contour-based modified first-order algorithm for uniform attenuation correction, and evaluates this method in U-SPECT-II. In Chapter V, the algorithm was extended to use X-ray CT information so that it can perform non-uniform attenuation correction. A comparison between these methods is also made. Chapter VI investigates the influence of attenuation map inaccuracy on micro-SPECT quantification. The final chapter provides a general summary and discussion.

Chapter II

Small-animal SPECT and SPECT/CT: application in cardiovascular research

Reza Golestani[1 *], Chao Wu[1,2 *], René A. Tio[3,4], Clark J. Zeebregts[4,5], Artiom D. Petrov[6],
Freek J. Beekman[2,7,8], Rudi A. J. O. Dierckx[1], Hendrikus H. Boersma[1,4,9],
Riemer H. J. A. Slart[1,4]

1 Department of Nuclear Medicine and Molecular Imaging, University Medical Center Groningen, Groningen, the Netherlands

2 Image Sciences Institute and Rudolf Magnus Institute of Neurosciences, University Medical Center Utrecht, Utrecht, the Netherlands

3 Thorax Center, Department of Cardiology, University Medical Center Groningen, Groningen, the Netherlands

4 Cardiovascular Imaging Group, University Medical Center Groningen, Groningen, the Netherlands

5 Department of Surgery, Division of Vascular Surgery, University Medical Center Groningen, Groningen, the Netherlands

6 Division of Cardiology, School of Medicine, University of California, Irvine, Irvine, California, USA

7 Faculty of Applied Sciences, Section Radiation Detection and Medical Imaging, Delft University of Technology, Delft, the Netherlands

8 MILabs B.V., Utrecht, the Netherlands

9 Department of Clinical and Hospital Pharmacy, University Medical Center Groningen, Groningen, the Netherlands

Eur J Nucl Med Mol Imaging (2010) 37:1766–1777
DOI 10.1007/s00259-009-1321-8

---

[*] Authors contributed equally to this work.

Abstract

Preclinical cardiovascular research using non-invasive radionuclide and hybrid imaging systems has been extensively developed in recent years. Single photon emission computed tomography (SPECT) is based on the molecular tracer principle and is an established tool in non-invasive imaging. SPECT uses gamma cameras and collimators to form projection data that are used to estimate (dynamic) 3D tracer distributions in vivo. Recent developments in multi-pinhole collimation and advanced image reconstruction have led to sub-millimetre and sub-half-millimetre resolution SPECT in rats and mice, respectively. In this article we review applications of micro-SPECT in cardiovascular research in which information about the function and pathology of the myocardium, vessels and neurons is obtained. We give examples on how diagnostic tracers, new therapeutic interventions, pre- and post-cardiovascular event prognosis, and functional and pathophysiological heart conditions can be explored by micro-SPECT, using small-animal models of cardiovascular disease.

Keywords: micro-SPECT, micro-SPECT/CT, cardiovascular imaging

2.1 Introduction

Small-animal models of cardiac disease play an important role in cardiovascular research, and the ability to translate the findings to the clinic has been proven in many cases [37–39]. The use of radionuclide imaging in small animals has provided many advantages for researchers to investigate in vivo molecular processes in cardiovascular pathology. Small-animal single photon emission computed tomography (SPECT) systems are now used by many centres for tracer development, therapy evaluation and pathophysiology investigations. Here we discuss the basic principles and preclinical applications of micro-SPECT and combined micro-SPECT/CT in cardiovascular research.

2.2 Background of micro-SPECT and micro-SPECT/CT

SPECT is based on the molecular tracer principle and detection of gamma rays by radiolabelled molecules. The suitable energy range of gamma rays for clinical SPECT is typically around 60–300 keV. Due to the small size of rats and mice, isotopes with much lower energies (e.g. ^{125}I, with 27–35 keV) can be employed in micro-SPECT, which would not be useful for imaging in patients. For obtaining tomographic images, tens up to hundreds of projection images of the animal are acquired with position-sensitive gamma-detectors. Today almost all small-animal SPECT is performed with pinhole collimators, since these collimators provide a much better noise resolution trade-off in small objects than parallel hole or fan-beam collimators that are commonly used in clinical cardiac SPECT. Most small-animal SPECT systems rotate either the detector and collimator or the object [8, 10, 21, 24, 25, 40–43]. Stationary small-animal pinhole SPECT systems [22, 23, 26, 44, 45] do not need to be rotated since they use detector set-ups that cover 360° and many pinholes to provide a large number of projection angles under which the animal is observed. They also have the advantage that dynamic imaging is possible with arbitrarily short frame lengths [22, 33, 46].

The full 360° coverage in combination with many focusing micro-pinholes and a high magnification factor to maximize the information content per photon provide a very high reconstructed image resolution. Multiple projections from different angles that can be acquired at the same time in such systems facilitate excellent ECG-gated myocardial imaging in rats and mice, which have heart rates of around 300 and 600 beats per minute, respectively. For instance, the U-SPECT-II system (MILabs, Utrecht, the Netherlands) has 75 pinholes on its interchangeable cylindrical collimators (Figure 2.1), and is based on three ultra-large NaI scintillation gamma-cameras. Reconstructed images can reach resolutions of ≤0.35 mm and 0.45 mm anywhere in the body using the mouse collimators with 0.35 mm and 0.6 mm gold pinhole apertures, respectively, and ≤0.8 mm with the standard total body rat collimator. It is expected that dedicated high-resolution detectors will contribute to further improvement in multi-pinhole SPECT resolution, thereby expanding the field of application of micro-SPECT. In addition, dedicated collimators to image specific organs are under development, and these can dramatically boost performance. Overviews and primers of pinhole SPECT technology have been provided by some investigators [4, 13].

In contrast to PET, dual-tracer or triple-tracer images can be readily obtained with SPECT. Multi-tracer imaging results in shorter acquisition times and perfect registration of images in space and time, and each tracer represents a different biological process. Another advantage of SPECT is that radiotracers can be produced more easily in the laboratory without the need for a cyclotron, so that the cost-effectiveness of SPECT is higher than that of PET. Clinical PET systems have a much higher resolution than SPECT, but this is

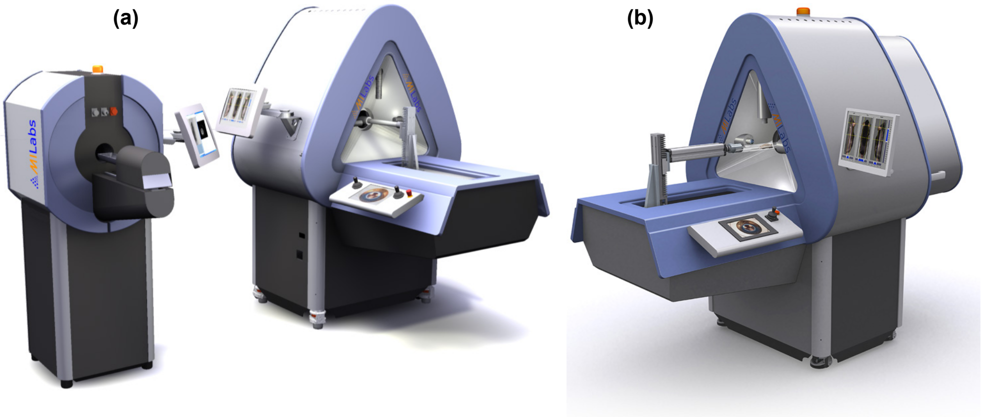

Figure 2.1 **(a)** Separate U-CT system and U-SPECT-II system. **(b)** Integrated U-SPECT-II/CT system.

reversed for micro-SPECT since the best resolution of commercial micro-PET systems is still above 1 mm [47, 48].

Perfusion SPECT provides valuable information for the diagnosis of patients with coronary artery disease (CAD). For example, in triple vessel disease, in which tracer delivery to the whole myocardium is diminished due to balanced hypoperfusion, SPECT images may be interpreted as normal in qualitative or semi-quantitative image analysis because comparison of the defective area with the region of the most intense uptake will not show any difference from normal. Absolute quantification of tracer uptake, which measures megabecquerels of tracer uptake per gram of tissue, can solve this problem [49]. The most prominent obstacles to absolute quantification in clinical SPECT used to be photon absorption and scattering, but today these problems are much smaller: SPECT systems equipped with transmission sources or, more recently, integrated with CT scanners are on the market [50–53]. These allow accurate correction for attenuation, and also use accurate methods to correct for scatter and collimator and detector blurring [54–63]. Cardiac and respiratory movements also degrade quantification, but both could be dealt with through (dual) gating as used in micro-PET imaging [64]. Although significant technical improvements for absolute quantification of myocardial perfusion using micro-SPECT have been introduced in recent years, the “roll-off” phenomenon with typical commercial SPECT perfusion agents under hyperaemic conditions, even in humans with less myocardial blood flow than mice, still remains a limitation for accurate measurement in myocardial perfusion imaging.

Quantification errors due to scatter and attenuation do degrade small-animal studies to a much lesser extent than in clinical SPECT because of less photon attenuation in small bodies (about 25% in the centre of a rat body when imaging with ^{99m}Tc [65]). Micro-CT imaging is able to provide photon attenuation information which can be used for non-uniform attenuation correction in micro-SPECT. However, several studies [65, 66] have shown that uniform attenuation correction (which may be based on the animal’s body contour) may reduce quantification errors from more than 10% to less than 5%. Therefore, a CT scan that adds dose and needs additional scanning equipment and scan time may be unnecessary. A webcam-based correction has been proposed [66].

Multimodal imaging can rely on separate devices (Figure 2.1a) in which images are fused through markers [67, 68], or marker-free methods in which the spatial relationship between beds is known through calibration [67, 69]. The accuracy of registration can be very satisfactory (0.2 mm), and an advantage is that SPECT and CT can be used in parallel, and are individually upgradable. Also registration with other systems such as MRI can be based on the same principles. The advantage and disadvantages of both approaches have been discussed [59, 70].

An attractive aspect of high-resolution integrated micro-SPECT/CT devices [71–74] (e.g. Figure 2.1b) is that the bed with the fixed animal does not have to be moved from one scanner to another. Integrated SPECT/CT, in which the bed moves through both the SPECT and the CT scanner is very convenient, although this approach is hard to extend to MRI, and image registration is still needed to obtain accurately matched combined images.

The translatability of the cardiovascular systems of small animals including mice and rats to the human cardiovascular system and the exceptional characteristics of modern micro-SPECT and multimodality imaging approaches provide promising opportunities in preclinical cardiovascular research. Novel micro-SPECT systems can provide quantitative images, and can perform longitudinal studies in the same animal, a high pinhole magnification factor resulting in high resolution, possibly dynamic imaging, and multi-tracer imaging. Micro-SPECT and micro-SPECT/CT systems have a wide range of applications in preclinical cardiovascular research, including investigation of myocardial left ventricular (LV) parameters such as ejection fractions and volumes, cardiac innervation parameters, vascular and atherosclerosis parameters, and the timing of administration and dose of novel radiotracers and biomarkers.

2.3 Myocardial applications

2.3.1 Left ventricular function

In order to assess the functional condition of the heart in transgenic mouse models in vivo, small-animal heart imaging can be used for verifying phenotypic differences as well as assessing the benefits of certain therapies. The ability to acquire gated images in small rodents which have high heart rates has eliminated the heart motion effect (Figure 2.2). It has been shown that ^{99m}Tc-labelled radiopharmaceuticals, which are routinely used for SPECT imaging in humans, can demonstrate viable tissue and perfusion status in animal models of ischaemia/reperfusion [45]. Further studies have demonstrated that myocardial perfusion defects are correlated with the true size of the defect, and can be analysed quantitatively as well as qualitatively [75, 76]. Liu et al. used animal models of myocardial ischaemia with coronary artery ligation and acquired images after ^{99m}Tc-sestamibi injection. The area where no uptake was seen corresponded with the infarcted tissue which was confirmed by triphenyl tetrazolium chloride (TTC) [45].

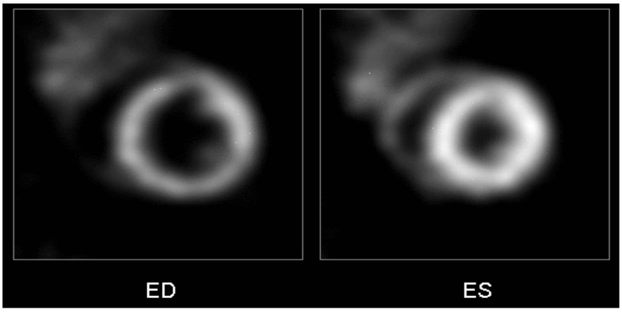

Figure 2.2 U-SPECT gated mouse cardiac perfusion images obtained in a normal C57BL/6 mouse (ED: end diastole, ES: end systole).

Cardiac and respiratory motion can always affect image resolution in SPECT and CT. In order to overcome this problem gating (cardiac and/or respiratory) is performed to synchronize the acquisition of projected data at the same time of the cardiac cycle. Gating also offers the chance to simultaneously map LV perfusion and assess LV function in clinical SPECT applications. ECG-gated micro-SPECT has been implemented in recent years. It has been shown that preclinical ECG-gated perfusion SPECT (in mice) permits quantification of LV volumes and motion as well. This is also a result of advances in image reconstruction software [77, 78]. The non-invasive nature of the test allows repeated studies in the same animal for follow-up studies [79].

2.3.2 Necrosis visualization

The development of necrotic tissue-avid tracers may help early detection of myocardial infarction (MI) noninvasively. In vivo visualization of necrotic tissue may also provide a quantitative index for evaluating the antinecrotic effect of drugs in development in animal models of ischaemic heart disease.

Glucarate is a small molecular weight compound, a six-carbon dicarboxylic acid sugar, which has affinity for histone proteins. In necrotic cells, due to lesions in the cellular and nuclear membranes, ^{99m}Tc-glucarate can bind to histone proteins and be retained in the tissue [80]. It has been shown that only minimal levels of glucarate bind to normal myocardial cells and viable ischaemic cells. Further studies have illustrated the possibility of immediate post-injection imaging with ^{99m}Tc-glucarate due to its rapid blood clearance [81]. Thus, by using ^{99m}Tc-glucarate as a SPECT tracer, necrotic cells can be depicted to provide data in acute coronary syndrome. Additionally, imaging of infarcts is possible within minutes of occlusion [82–84]. Moreover, it has been shown, by comparative investigations using TTC staining, that SPECT images of ^{99m}Tc-glucarate uptake allow accurate assessment of infarct size. Conversely, it has been shown that there is no glucarate uptake in old necrotic myocardial tissue. Although glucarate uptake in necrotic tissue occurs as early as 3 hours after ischaemia/reperfusion, at 10 days after necrosis there is no obvious tracer uptake in the heart [85].

Some studies have focused on other necrotic tissue-avid tracers than glucarate compounds. Porphyrin derivatives were initially developed as tracers for tumour cell tracking. Reports of the avidity of porphyrin derivatives for necrotic tissue [86–88] and studies on their use in visualization of infarcted tissue by MRI led to efforts to radiolabel hypericin. Hypericin is a natural substance with a biological activity similar to that of porphyrin. Both substances are known to be photosensitizers and have been used in antitumour therapies [89]. Ni et al. synthesized mono-[^{123}I]iodohypericin (MIH) and injected it into rabbit models of MI. SPECT imaging compared to TTC staining and autoradiography confirmed the accumulation of [^{123}I]MIH in the infarcted tissue [90]. In addition, due to the minimal levels of tracer uptake in normal myocardium, the target to non-target tracer concentration ratio was very high. In another study, Fonge et al. compared the results of [^{123}I]MIH micro-SPECT with the results of [^{13}N]ammonia micro-PET in rabbit models of MI. There was a correlation between areas with low blood flow in micro-PET and [^{123}I]MIH uptake in micro-SPECT [91].

2.3.3 Apoptosis visualization

Apoptotic cell death has been the subject of many studies investigating opportunities for therapeutic interventions. Apoptosis is an energy-requiring highly regulated form of cell death which is characterized by cell shrinkage, DNA fragmentation, caspase activation, membrane blebbing, and phosphatidyl serine (PS) externalization. It has been demonstrated that reperfusion injury in the heart leads to apoptotic cell death [92–95]. The role of apoptotic cell death in heart failure has also been investigated in many studies [96–98]. The development of radiopharmaceuticals that bind to apoptotic cells has been useful for in vivo evaluation of therapeutic efforts in apoptotic cell death in cardiomyocytes. Annexin A5, a 36 kDa physiological protein, has affinity for binding to the externalized PS. ^{99m}Tc-Annexin A5 has been used as a SPECT tracer in recent years for detecting apoptosis in the preclinical and clinical settings in vivo. ^{99m}Tc-Annexin A5 uptake has been confirmed by apoptosis-specific immunohistochemistry assays [99–105]. Nevertheless, PS exposure has been shown not to be specific for apoptotic cell death. In necrosis as well, due to leakage in the cell membrane, PS can be exposed and bound to annexin A5. Annexin A5 can visualize apoptotic PS externalization specifically, if used with a second marker showing an intact cell membrane [106].

More recently, a new ^{99m}Tc-bound, PS-avid agent has been developed. The C2A domain of synaptotagmin, which binds to PS in a calcium-dependent manner, has been shown to be sensitive for cell death detection [107]. False positive uptake, due to some extent to PS exposure in other forms of cell death, led investigations to find more specific tracers for apoptosis visualization. Caspase-3, altered membrane permeability, and several enzymes which are responsible for apoptosis, are appropriate potential targets for apoptosis imaging.

2.3.4 Stem cell therapy evaluation

The recent treatment strategy for cell-death-related heart disease, cellular cardiomyoplasty, needs to be evaluated in preclinical investigations. The most important objectives for the investigations are the optimal cell type, route of delivery, number of cells, suitable timing after infarction, and future monitoring of grafted cells. Imaging modalities may help stem cell therapy in the heart in three ways, including tracking and quantification of transplanted cells, assessment of function and differentiation, and monitoring of underlying tissue status, as well as in assessing the problems involved in the generation of suitable cell materials [108–110]. Zhou et al. used stem cell grafts labelled with ^{111}In-oxyquinoline and performed double tracer ultrahigh resolution SPECT with ^{99m}Tc-sestamibi to evaluate the engraftment of the stem cells in the infarcted area [111]. However, due to the half-life of ^{111}In-oxyquinoline (67.2 h) the imaging could be only done within 96 h of engraftment, and because radioactivity in stem cells remains in the area even after the cells have died, quantification of uptake may overestimate the survival fraction of injected stem cells. Thus, this method may be useful for short-term tracking of the cells and investigating homing strategies for engraftment.

To assess the function of the targeted cells by SPECT, gene imaging can also be used. Gene expression can be assessed by reporter genes. For imaging with a reporter system, a probe is administered to the subject and selectively bound or metabolized with the reported gene product. This interaction results in probe trapping by the transgenic cell and its level is proportional to the gene expression. The result shows the functionality of the cell. One of the reporter genes most used in this regard is herpes simplex virus tyrosine kinase (HSV1-tk), which is absent in mammalian cells and expresses the tyrosine kinase enzyme that converts cytosine to uracil. Hence, only transgenic cells which express this gene can convert 5-fluorocytosine to 5-fluorouracil, and administration of radiolabelled nucleoside to the subject and acquisition with SPECT will show the tracer uptake in the area of cells expressing the reporter gene [112].

A study on tumour cells has shown the sensitivity of the D-isomer of ^{123}I-2′-fluoro-2′-deoxy-1-beta-D-arabinofuranosy-5-iodo-uracil (d-FIAU) in detecting cells positive for HSV1-tk [102]. It has been shown in a study on Wistar rats injected with the adenovirus-expressing hNIS gene that imaging with iodine and technetium tracers can verify the activity of cardiomyocytes [113]. Thus, transferring the gene to the stem cells prior to myocardial cell transplantation can aid the further tracking and monitoring of the graft. Furthermore, for assessment of gene therapy, co-expression of the hNIS gene with the gene of choice has shown promise for future monitoring of cardiac gene therapy. However, one potential obstacle in the use of hNIS for stem cell tracking is gene silencing, which has been reported in neurological studies [110].

2.3.5 Remodelling investigations

LV remodelling after MI leads to LV dysfunction and failure. Matrix metalloproteinase (MMP), a proteolytic enzyme, has been shown to play a causal role in this process [114]. In vivo MMP activation imaging may provide data to quantify and localize MMP activity and its role in further LV remodelling. In addition, MMP imaging provides the opportunity to track therapeutic efforts directed at MMP inhibition to reduce post-MI remodelling. Su et al. investigated the activation of MMP enzymes with micro-SPECT/CT in mice models of MI. They used a ^{99m}Tc-bound radiotracer (RP805) to visualize MMP in vivo and compared it to in situ zymography, and found a good correlation between the results [115].

The role of blood coagulation factor XIII in post-MI healing has also been studied using ^{111}In-NQEQVSPLTLLK [102]. The non-invasive imaging of factor XIII may help further investigations on the assessment of factor XIII-targeted therapies [116].

2.3.6 Innovative pathophysiology investigations

A better understanding of pathophysiology can shed light on the pathological processes in cardiovascular diseases, and may lead to new therapeutic interventions. Animal models, especially mice and rats, have been used traditionally for the investigation of molecular processes in cardiovascular diseases. Radionuclide imaging has significantly improved our understanding of several aspects of pathophysiology in small animal models. For instance the role of sigma receptors in cardiomyocytes has been studied in recent years. Their role in blocking the potassium channel and decreasing neuroexcitability in intracardiac neurons has been reported by Zhang and Cuevas [117]. Sigma receptors are a largely unexplored area of cardiology, and should be studied. Recent efforts towards radionuclide imaging of sigma receptors in various organs can be expanded in cardiology to better distinguish sigma receptor function in cardiovascular systems [118].

In another investigation, ^{99m}Tc-losartan was used for non-invasive imaging of angiotensin receptors in mouse heart muscle cells after permanent ligation of the left anterior descending artery [119]. Increased tracer uptake in post-MI hearts and its correlation with remodelling showed the role of the renin-angiotensin axis in progression of heart failure after MI. In addition, this study demonstrated the potential role of non-invasive imaging strategies in identification of patients likely to develop heart failure.

2.4 Cardiac innervation imaging

The autonomic nervous system plays an important role in cardiovascular diseases. Disturbances in function and integrity, as well as enhanced sympathetic activity may lead to numerous heart pathologies. Therefore, evaluation of the sympathetic innervation of the heart could provide important data on the aetiology and progress of heart diseases. It might also provide a tool for non-invasive assessment of novel therapeutic approaches targeting sympathetic nervous system activity, and also assessment of the side effects of drugs on cardiac adrenergic function. ^{123}I-labelled metaiodobenzylguanidine (^{123}I-MIBG), an analogue of the false neurotransmitter guanethidine, has been used clinically for sympathetic neuronal activity and integrity since the 1980s. Presynaptic sympathetic nerve terminals can take up and store MIBG in the same way as norepinephrine. Thus, MIBG uptake and washout rate can be influenced by sympathetic tone and the integrity of nerve terminals. Studies using ^{123}I-MIBG in animal models of coronary artery occlusion have revealed more extended nerve damage than myocardial injury in MI [120]. Also, some investigations have focused on the role of denervation in diabetic heart disease and cardiomyopathy [121]. ^{123}I-MIBG uptake defects have also been shown to be related to arrhythmogenesis in the heart after CAD, cardiomyopathy and other cardiac pathologies [122]. Due to more favourable properties of ^{99m}Tc-bound radiopharmaceuticals compared with ^{123}I-based tracers, Samnick et al. labelled 1-(4-fluorobenzyl)-4-(2-mercapto-2-methyl-

4-azapentyl)-4-(2-mercapto-2-methylpropylamino)-piperidine (FBPBAT) with ^{99m}Tc and compared its characteristics in the assessment of cardiac adrenergic function in the rat with those of ^{123}I-MIBG [123]. They used rat models pre-treated with α1 and β1 inhibitors and acquired SPECT images after radiopharmaceutical incubation. ^{99m}Tc-FBPBAT showed higher uptake than ^{123}I-MIBG. ^{99m}Tc-FBPBAT also had more cardiac adrenergic specificity. Moreover, ^{99m}Tc-FBPBAT targeted postsynaptic adrenoreceptors, whereas ^{123}I-MIBG was absorbed via a presynaptic uptake I route. In another study, the average effective dose of ^{99m}Tc-FBPBAT was shown to be less than half that of ^{123}I-MIBG [124]. These studies encourage further investigations of ^{99m}Tc-based radiopharmaceuticals for SPECT studies of cardiac adrenergic innervation [122].

2.5 Vascular applications

2.5.1 Angiogenesis monitoring

Another field of study in ischaemic diseases, including ischaemic heart disease, is the stimulation of angiogenesis in the injured tissue. Angiogenesis is an important process in infarct healing and post-MI LV remodelling. Thus, non-invasive imaging of angiogenesis may improve risk stratification in post-MI patients. Angiogenesis imaging can also provide a tool to evaluate therapeutic interventions aimed at angiogenesis stimulation. Integrins, a family of cell surface receptors, are known to play a role in angiogenesis. αvβ3 integrin-avid agents have been used to visualize angiogenesis in post-infarct animal models. ^{111}In- or ^{123}I-labelled αvβ3 integrin-avid radiotracer has been shown to be focally retained in hypoperfused myocardial regions [83, 125]. Vascular endothelial growth factor (VEGF) also plays a key role in angiogenesis. The radiolabelled antibodies for VEGF have also been used for detecting angiogenesis, especially in tumour cells. Other detectable factors involved in the angiogenesis process, such as activated endothelial cells and MMP, are potential targets for radionuclide imaging of angiogenesis [125].

2.5.2 Plaque imaging

Rupture of atherosclerotic plaque results in severe cardiac events in 70% of acute MIs and sudden cardiac death. Anatomical methods of atherosclerosis imaging visualize coronary artery stenosis, which is responsible for 20% of plaque complications. However, the majority of acute coronary events are a consequence of rupture and further thrombotic occlusion in non-stenotic lesions. Criteria to regard a plaque as rupture-prone and vulnerable have been suggested by Naghavi et al. [126]. The important attributes regarding injury, inflammation, thrombogenicity, proteolysis, stenosis and morphology play a role in the prediction of plaque vulnerability. The major criteria for labelling a plaque as vulnerable include: active inflammation (monocyte/macrophage and T-cell infiltration), thin cap with large lipid core, superficial platelet aggregation, fissure, and stenosis >90%. Apart from CT-provided data on stenosis, molecular imaging techniques have been widely used in recent years to depict biological processes within plaque regarding other plaque vulnerability criteria as mentioned above [127]. It is particularly noteworthy that the characteristics of the most common type of vulnerable plaque are inflammatory cell infiltration, platelet aggregation, MMP activation, large lipid core content and apoptosis, but not significant stenosis [126]. Thus, addition of molecular imaging techniques to routine plaque assessment procedures can potentially provide better recognition of vulnerable atherosclerotic plaques.

2.5.2.1 Apoptosis in plaques

Apoptosis is one of the characteristics of a vulnerable atherosclerotic lesion. It has been shown that apoptosis occurs in smooth muscle cells and monocytes in the plaque, and is a good target for visualizing atherosclerotic plaque, in addition to categorizing plaques as vulnerable. In a study on the detection of atheroma in the aorta of balloon-injured rabbits, focal ^{99m}Tc-annexin A5 uptake was shown to be correlated with macrophage apoptosis in the plaque [128].

Isobe et al. demonstrated that SPECT/CT imaging with annexin A5 compounds provides appropriate correlation between tracer uptake and apoptosis in plaques [129]. They showed that in ApoE$^{-/-}$ mice, induced atherosclerotic plaque can be detected by ^{99m}Tc-annexin A5, and the quantitative uptake is related to the macrophage content of the plaque. Reduced ^{99m}Tc-annexin A5 uptake after diet modification and simvastatin therapy has been shown in another study [130].

2.5.2.2 Thrombogenicity

Thrombosis at the rupture site or the sites of superficial erosions on the plaque is another marker that predicts the vulnerability of plaque. Thrombosis visualization can help predict future events in CAD. Fibrin detection by CT using fibrin-targeted nanoparticles has recently been reported in humans [131]. It can also be used in animal models of cardiovascular diseases to evaluate therapeutic interventions for thrombosis formation and dissolution.

2.5.2.3 Lipoprotein accumulation

Vulnerable plaques contain more than 40% low-density lipoproteins in their core [126]. ^{99m}Tc-labelled oxidized low-density lipoproteins (oxLDL) allow visualization of lipid accumulation within macrophages and foam cells. Iuliano et al. showed rapid blood clearance and tracer uptake by atherosclerotic plaque in humans [132]. Further studies quantifying tracer uptake and its contribution to the vulnerability of plaques have been performed in small-animal models of CAD [133, 134].

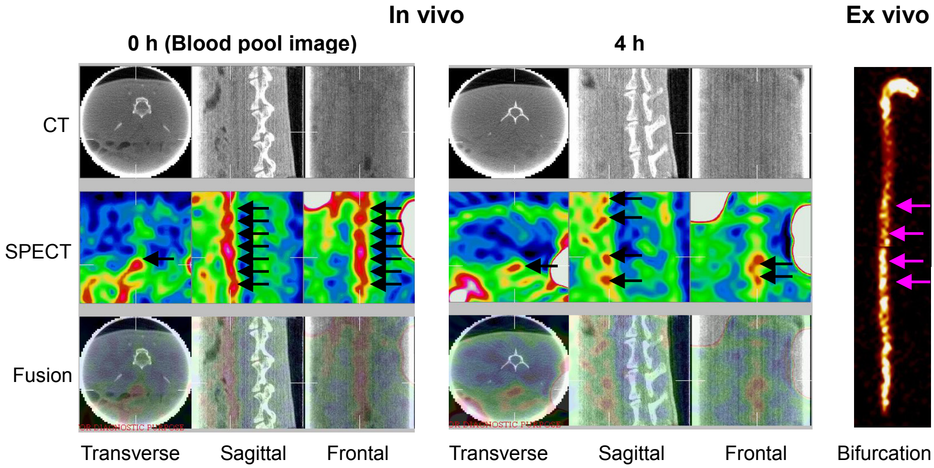

Figure 2.3 Uptake of RP805 (a broad-spectrum MMP ligand) demonstrating MMP expression in an atherosclerotic rabbit on an uninterrupted diet. The three columns display transverse, sagittal, and frontal projections, and the three rows display micro-CT, micro-SPECT, and fusion images. The left set of three columns displays images immediately (0 h) after radiotracer administration (representing blood pool images), and the right set of three columns displays images obtained at 4 h (representing tracer uptake in target tissue). The images were adapted from [137].

2.5.2.4 Inflammation

The inflammatory nature of atherosclerosis, due to infiltration of the plaque with macrophages/monocytes and T lymphocytes, provides a target for cell content imaging of atherosclerotic plaques. Interleukin-2 (IL-2), labelled with ^{99m}Tc, was used by Annovazzi et al. to demonstrate T-cell infiltration in human carotid artery atherosclerotic plaques [135]. This study showed the accumulation of tracer in vulnerable plaques and also demonstrated the consequent influence of lipid-lowering on uptake. Circulating monocyte recruitment in the plaque site and lipid phagocytosis by phagocytes have also been studied as approaches to inflammation visualization in atherosclerotic plaques. Although most investigations in this field have been done using micro-PET, the known advantages of SPECT systems and SPECT specific tracer labelling should stimulate more studies on plaque inflammation by micro-SPECT.

2.5.2.5 Proteolysis

Activation of MMP in the atherosclerotic plaque may lead to further instability and rupture. Schafer et al. studied the feasibility of using a ^{123}I-labelled MMP inhibitor in a known model of arterial remodelling and lesion development [136]. They showed that SPECT imaging using [^{123}I]I-HO-CGS 27023A can be an appropriate method for measurement of MMP activity within the plaque. In another study, a ^{99m}Tc-labelled broad MMP inhibitor was used to determine the effects of statin therapy and dietary modification on MMP activation in rabbit models of atherosclerosis [137]. The micro-SPECT/CT results were compared with histological and immunohistochemical results as well as the results of ex vivo autoradiography, and showed the feasibility of non-invasive MMP activity detection (Figure 2.3).

2.5.2.6 Angiogenesis in plaque

Angiogenesis in atherosclerotic plaque may cause intraplaque haemorrhage and therefore contribute to more risk of plaque rupture. Imaging of angiogenesis with specific tracers which are avid to angiogenic factors, by SPECT or SPECT/CT, can also reveal valuable information on plaque. Imaging of intraplaque haemorrhage, if possible, will also provide valuable information on plaque vulnerability. Davies et al. showed that a proportion of Annexin V uptake in atherosclerotic plaque is due to red blood cell remnants in the plaque after intraplaque haemorrhage [138]. However, specific tracers for tracking bleeding within the plaques have not yet been developed.

2.6 CT applications

2.6.1 Myocardial application

Micro-CT studies of the heart need blood-pool imaging to make the heart contour clear. Iodinated triglyceride is a blood-pool agent that remains in the blood for hours and is cleared slowly through the hepatobiliary systems. This contrast agent, due to its long circulation time, provides the opportunity to select the best post-injection time points for imaging and induces good contrast enhancement between myocardium and blood (500 HU) [139, 140]. Mukundan et al. [141] studied another iodinated agent for micro-CT which showed more contrast enhancement between myocardium and blood in the LV (650–700 HU). In another study, a novel polymer-coated Bi2S3 nanoparticle (BPNP) was used as contrast agent for CT scanning in mice. This agent showed high stability, high x-ray absorption (fivefold more than that of iodinated agents), and more than 2 hours of circulation time. CT scan of mice using BPNP as contrast agent showed clear delineation of ventricles and vascular structures [142].

In order to evaluate remodelling processes after MI in mouse models, Detombe et al. used retrospective gated micro-CT [143]. The ability to obtain dynamic images, and short scanning times (<1 min), quantification, and the ability to monitor the same animal during a longitudinal study are promising results of this study. More investigations in the future using hybrid imaging systems (e.g. micro-SPECT and micro-CT) will add more dimensions to current preclinical studies.

2.6.2 Vascular dynamics

To investigate the dynamics of myocardial microvessels, BaSO4 contrast micro-CT has been used for 3D visualization of the capacitance of intramyocardial vessels during systole and diastole [144]. In this study, the 3D architecture of microvessels was demonstrated. Images also showed that the vascular volume fraction is decreased from diastole to systole by 48%, but is not collapsed.

2.6.3 Vascular dynamics

Atherosclerotic plaque calcification is correlated with total plaque burden and future cardiovascular events [145]. Exploring the underlying pathology of plaque calcification will suggest the direction for future interventions. It has been shown that formation and progression of plaque calcification is correlated with inflammation and apoptosis in atherosclerotic plaques [145, 146]. Interestingly, it has been shown that micro-CT can detect plaque calcification in small rodents [129, 147]. Isobe et al. demonstrated the feasibility of micro-CT images in detecting plaque calcification in the aorta [129]. Although, they used ^{99m}Tc-annexin micro-SPECT/CT to detect apoptosis in ApoE$^{-/-}$ mice they did not investigate the correlation between calcification and tracer uptake. Further studies using SPECT/CT to correlate different parameters of plaque vulnerability, using SPECT, with calcification, detected by CT, can offer a better understanding on the pathology underlying plaque calcification.

Vascular wall calcification in rodents can also be detected by micro-CT. In one study on uraemic mice, which have been shown to be a suitable model for vascular calcification, calcification of the aorta was detected and quantified by micro-CT [148]. The quantification results proved to be reproducible and well-correlated with ex-vivo histological evaluation. This may provide investigators with a promising technique to follow-up and monitor the effects of therapies aiming to reverse vascular calcification in patients with chronic renal failure.

2.7 Conclusion

Micro-SPECT and micro-SPECT/CT are powerful tools for elucidating fundamental pathophysiological pathways of heart diseases. They provide information on cardiovascular processes at the molecular and cellular levels. They also offer the opportunity to monitor pharmacological and biological therapeutic interventions in preclinical investigations. Moreover, studies on radiotracer development for detecting new aspects of cardiovascular pathophysiological processes can be investigated in experimental models of cardiovascular pathology. The recent development of hybrid imaging systems, besides providing technical improvements in image quality, adds phenotypic data to functional radionuclide imaging information.

Acknowledgment

We thank Ralph Houston for his help during the preparation of the manuscript.

Chapter III

Influence of respiratory gating, image filtering and animal positioning on high-resolution ECG-gated murine cardiac SPECT

Chao Wu[1,2], Brendan Vastenhouw[1,2,3], Pieter E. B. Vaissier[1], Johan R. de Jong[4],
Riemer H. J. A. Slart[4], Freek J. Beekman[1,3]

1 Section Radiation, Detection & Medical Imaging, Delft University of Technology, Delft, the Netherlands

2 Rudolf Magnus Institute of Neuroscience, University Medical Center Utrecht, Utrecht, the Netherlands

3 MILabs B.V., Utrecht, the Netherlands

4 Department of Nuclear Medicine and Molecular Imaging, University Medical Center Groningen, University of Groningen, Groningen, the Netherlands

Abstract

Parameters obtained from cardiac SPECT are influenced by respiratory motion, image filtering and animal positioning. Here we investigate these effects in pre-clinical SPECT.

Methods: Five mice were injected with ^{99m}Tc-tetrofosmin and subsequently scanned in supine and prone positions using a U-SPECT-II scanner with simultaneous ECG and respiratory gating. ECG-gated myocardial perfusion images were reconstructed under three different strategies: by using gamma counts of (i) all respiratory gates without applying respiratory motion correction, (ii) only six out of eight respiratory gates (that have limited motion) without applying respiratory motion correction, and (iii) all respiratory gates with respiratory motion correction applied. All images were filtered with 3D Gaussian kernels ranging from 0.5–1.0 mm full width at half maximum (FWHM), and were analysed with Corridor4DM in order to compare cardiac parameters.

Results: The average left ventricular volume (LVV) over all mice was 50±11 µl at end diastole (ED) and 22±8 µl at end systole (ES), and the average left ventricular ejection fraction (LVEF) over all mice was 57±7%. The average LVEF differed <2.0% when changing reconstruction strategies, <4.6% when changing filter kernel sizes, and <2.8% with different animal positioning. However, relatively large LVV differences (>10 µl) were found in three mice as a consequence of their positioning.

Conclusion: In general, animal positioning can affect cardiac parameters obtained from some animals, while the influence of respiratory gating and different image filtering tested is showed to be limited.

Keywords: gating, cardiac imaging, small-animal SPECT

3.1 Introduction

In addition to tissue properties of the myocardium such as perfusion or viability, ECG-gated cardiac SPECT provides ventricular volumes, ventricular ejection fractions as well as myocardial wall-motion and thickness [149–152]. In such studies, image artefacts can be created due to respiratory motion. Respiratory gating has been applied for imaging lung areas to reduce image artefacts [153, 154]. Respiratory gating involves decomposition of the data into separate parts that represent different breathing phases. As the position and orientation of the heart is also affected by respiratory motion, it is prudent to investigate whether respiratory gating may also reduce image blur and may improve cardiac imaging quality. As early as 1998, the scheme and algorithm for simultaneous ECG and respiratory gating (“dual gating”) was already studied, developed and tested with a phantom in a clinical positron emission tomography (PET) scanner by Klein et al [155]. It was found that the extent of the motion induced by respiration is comparable to the myocardial wall thickness [156, 157]. As a result of this study, many clinical cardiac studies were performed with simultaneous ECG and respiratory gating in order to obtain better resolved myocardial walls [158, 159].

Development of gating techniques in small-animal cardiac imaging started relatively late, partly because the spatial resolution of early pre-clinical SPECT scanners was not high enough to benefit from the possible improvement of gating. However, ECG gating is extremely useful with sub-half-millimetre-resolution SPECT that has recently become available. ECG gating has already been evaluated for small animals for assessing their left ventricular function and has been applied in studies where new pharmaceuticals were tested [77, 79, 160–164]. Simultaneous ECG and respiratory gating has been assessed for an approximately 1-millimetre-resolution micro-PET system [64]. In this study, it was found that although respiratory motion was detectable in the images, it was small in spatial extent and duration, and could likely be ignored for most studies performed with millimetre-resolution PET. However, whether the assessment of cardiac function in SPECT with sub-half-millimetre resolution can benefit from simultaneous ECG and respiratory gating has not yet been investigated.

Two other factors may also influence the assessment of cardiac function. On the one hand, cardiac quantification software usually fits a flexible 3D model of the left ventricle to the reconstructed activity in the myocardium and calculates cardiac parameters via this model. Image filtering changes the smoothness and thickness of the reconstructed activity in the ventricular wall, which may result in changes of the fit of the 3D model to the left ventricle in the heart image and therefore may change cardiac parameters that are calculated from the fitted model. This effect has already been observed in clinical studies [165–169] in which changes to cardiac parameters were mainly induced by filter kernels applied to projection data before image reconstruction. On the other hand, the position of an animal (supine or prone) during scanning affects arterial filling, which may result in different restrictions on thoracic movement, and thus may result in different levels of heart motion due to respiration. In such case, people may find that respiratory motion correction has fewer efficacies with the animal in one position than with the animal in the other position and therefore which position is more suitable for cardiac research. This has already been investigated in clinical studies: changes in left ventricular volume were detected but no significant differences in ejection fraction were found [170–172]. However, no such study has been performed in small-animal imaging so far.

In this study we investigate the influence of respiratory gating, image filtering and mouse positioning on high resolution ECG-gated ^{99m}Tc-tetrofosmin myocardial perfusion SPECT.

3.2 Materials and methods

Animal studies were conducted following protocols approved by the Animal Research Committee of the University Medical Center Utrecht.

3.2.1 In vivo myocardial perfusion imaging of mice

U-SPECT-II (MILabs B.V., Utrecht, the Netherlands) [26] is a stationary focusing multi-pinhole SPECT imaging system designed for small-animal studies. When imaging with ^{99m}Tc, the highest possible spatial resolution of this system is about 0.35 mm achieved with using the general purpose mouse collimator (used in this study) that is equipped with 0.6 mm pinholes. The system can accept three transistor–transistor logic (TTL) trigger signals for gated studies through three Bayonet Neill–Concelman (BNC) connectors on the side panel. Trigger events are recorded together with photon-counting events in list mode.

In this study, five C57-BL6/J mice underwent scans. Each mouse was injected via the tail vein with about 200–250 MBq ^{99m}Tc-tetrofosmin in about 0.3–0.4 ml. Two cardiac SPECT scans focused on the heart were performed for each mouse, starting about 30 minutes post injection. The first scans lasted for 60 minutes and the second scans lasted for 70 minutes. The extra scan time of the second scan compensated for the decay of ^{99m}Tc in order to obtain approximately equal amounts of counts in both scans. For each mouse one scan was performed with the mouse in a supine position on the animal bed and the other scan was performed with the mouse in a prone position. To avoid that the order of the scans (supine/prone or prone/supine) disturbed our judgement on the influence of positioning, we alternated the positioning order for different mice. The mice were anaesthetized with a mixture of 1.6–2.0% isoflurane in medical air (Univentor, UNO B.V., Zevenaar, the Netherlands). The ECG signal was measured by using three ECG leads (Neonatal Monitoring Electrode, 3M, Maplewood, MN, USA) and the respiratory signal by using a respiration sensor (Graseby Respiration Sensor, Medicare, Kilmacanogue, Ireland). Both signals were sent to an animal monitoring and gating module (BioVet, m2m Imaging, Cleveland, OH, USA). Two channels of trigger signals for ECG and respiratory gating were produced by this device and were sent to the U-SPECT-II system via two BNC connectors.

3.2.2 Image reconstruction strategies

Trigger events were detected during list-mode data processing. Each temporal interval between two adjacent ECG trigger events was divided into eight cardiac phases, and each interval between two adjacent respiratory trigger events was also split into eight respiratory phases. This resulted in 64 possible combinations of cardiac and respiratory phases. Each photon count in the list-mode data was sorted into one of 64 projection data bins depending on how its time stamp located in the ECG and respiratory intervals, as is illustrated in Figure 3.1.

For each scan 64 dual-gated image frames were reconstructed by a pixel-based ordered subset expectation maximization (POSEM) algorithm [32] that used 16 subsets and 6 iterations for the reconstruction of each frame. Next, the eight frames of an ECG-gated heart image were reconstructed from these 64 dual-gated image frames by averaging frames corresponding to the same cardiac phases, during which three different strategies were

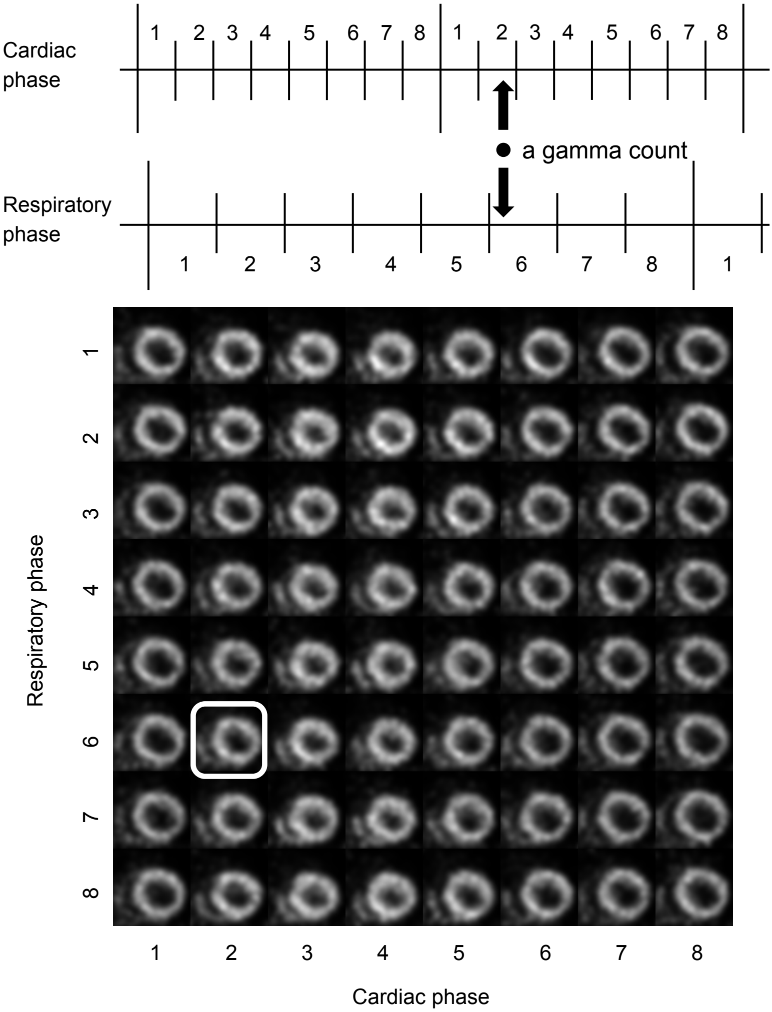

Figure 3.1 Dual gating scheme with 8 ECG and 8 respiratory gates. A count that is e.g. in the 2nd cardiac phase and the 6th respiratory phase will be sorted into the projection data bin corresponding to this combination of phases. The reconstructed image frame for this combination of phases is indicated by the white box.

employed to study the influence of respiratory motion.

Firstly, “standard reconstruction”: image frames of all eight respiratory gates that were in the same cardiac phase were averaged directly. This way, the counts in all respiratory gates were used and no respiratory motion correction was applied. The resulting images were equivalent to ECG-only-gated images.

Secondly, “motion-reduced reconstruction”: image frames of 2nd–7th respiratory gates that were in the same cardiac phase were averaged directly. This strategy is based on a hypothesis that significant motion only occurs when a trigger signal is created, which was revealed in [64]. This way we threw away the counts acquired in respiratory gates that correspond to the largest respiratory motions and the resulting images may be less influenced by respiration.

Thirdly, “motion-corrected reconstruction”: image frames of all eight respiratory gates that were in the same cardiac phase were firstly registered to each other, and then averaged. This way all respiratory gates were used. The purpose of image registration is to correct for heart motion due to respiration, and details of the registration procedure are discussed in the following section.

3.2.3 Image registration for motion-corrected reconstruction

Contraction associated with cardiac phases mainly changes the shape of the heart, while respiratory motion primarily changes the position and orientation of the heart as the diaphragm, the chest wall and the lungs move with breaths [155]. The differences between the cardiac images caused by the latter are mainly rigid translations and rotations of the heart; heart motion due to respiration can therefore be corrected by using a simple rigid registration procedure. In principle, a dual-gated image frame corresponding to any respiratory phase could serve as a reference image frame for the registration of the image frames that correspond to the same cardiac phase but to different respiratory phases. However, the noise level in the 64 individual dual-gated image frames was relatively high, because of the relatively low number of counts with which each image frame was reconstructed. Therefore, we did not determine the registration parameters from these image frames directly, rather we calculated these parameters from eight respiratory-only-gated images: each of these images was an average of the eight dual-gated image frames that corresponded to one respiratory phase but to different cardiac phases. The respiratory-only-gated image of the 5th respiratory phase served as the reference image, and the respiratory-only-gated images of the other seven respiratory phases were registered to this image. This resulted in seven sets of rigid transformation parameters. These transformations were then applied to the 56 dual-gated image frames that corresponded to the 1st–4th and 6th–8th respiratory phases.

The rigid transformation parameters were calculated by using the elastix toolbox [173]. The normalized correlation coefficient (NCC) between two images was selected as the metric for registration. To avoid influence of high activity uptake in the liver and the gall bladder on the registration procedure, a 3D elliptical mask was used that only covered the heart. This mask was fixed to the reference image and the transformation parameters were calculated using only the voxels inside the mask region.

3.2.4 Image processing and analysis

We analysed the images with the Corridor4DM software (INVIA, Ann Arbor, MI, USA). All ECG-gated images were spatially filtered with Gaussian kernels of 0.5 mm, 0.6 mm, 0.7

mm, 0.8 mm, 0.9 mm and 1.0 mm full width at half maximum (FWHM) and then filtered along temporal frames (cardiac phases) by means of a circular convolution with a [0.25, 0.5, 0.25] kernel function. In order for the clinical Corridor4DM software to accept mouse-heart images, the voxel size of the images was changed from 0.2 mm to 2 mm. The cardiac parameters calculated by the software were then rescaled so that they corresponded to the original voxel size.

In this study we tried to minimize our interference with the software analysis procedure. Corridor4DM is designed to automatically detect and perform the location and reorientation of the heart by using an iterative algorithm. However, due to the influence of high activity uptake in the liver and the gall bladder very close to the heart (which is not the case in human patients), this automatic procedure failed for a few images. Only for these images, we manually performed initial translations and rotations. After importing the images, a flexible 3D left ventricle (LV) model was fitted to the LV walls in the images. The left ventricular volume (LVV) in each cardiac phase was calculated using this model, and the maximum and minimum LVVs of all cardiac phases were defined as the end-diastolic volume (EDV) and end-systolic volume (ESV) of the left ventricle. The left ventricular ejection fraction (LVEF) was also provided by the software.

In addition to cardiac parameters, we also looked directly at the ventricular walls in the images. In order to compare images reconstructed under the three different strategies, we applied an extra registration between these images and examined line profiles along different positions and directions in the images.

3.3 Results

3.3.1 Respiratory motion and image profiles

When performing motion correction by means of image registration (motion-corrected reconstruction), we found that the resulting transformation matrices that contained the largest motions (about 1 mm translation) corresponded to the 8th respiratory phase in which the trigger signal was created. The second largest motions (about 0.4 mm) occurred in the 1st phase; during the rest of the respiratory phases, the translations were generally less than 0.2 mm (Figure 3.2). This is consistent with our hypothesis that was the precondition for the motion-reduced reconstruction strategy that only uses the 2nd–7th respiratory gates.

When inspecting cardiac slices from images reconstructed under the three reconstruction strategies, we found no visual differences in most cases, as can be seen in Figure 3.3 (top) from the short-axis (SA) slices and vertical-long-axis (VLA) slices of Mouse 2 at end diastole (ED) in both supine (left) and prone positions (right). The only obvious deviation was found in the VLA slice and profile of Mouse 5 (Figure 3.3, bottom) that was acquired in a supine position and reconstructed by the motion-reduced method (indicated by the arrow pointing to the green VLA profile in Figure 3.3): the intensity of

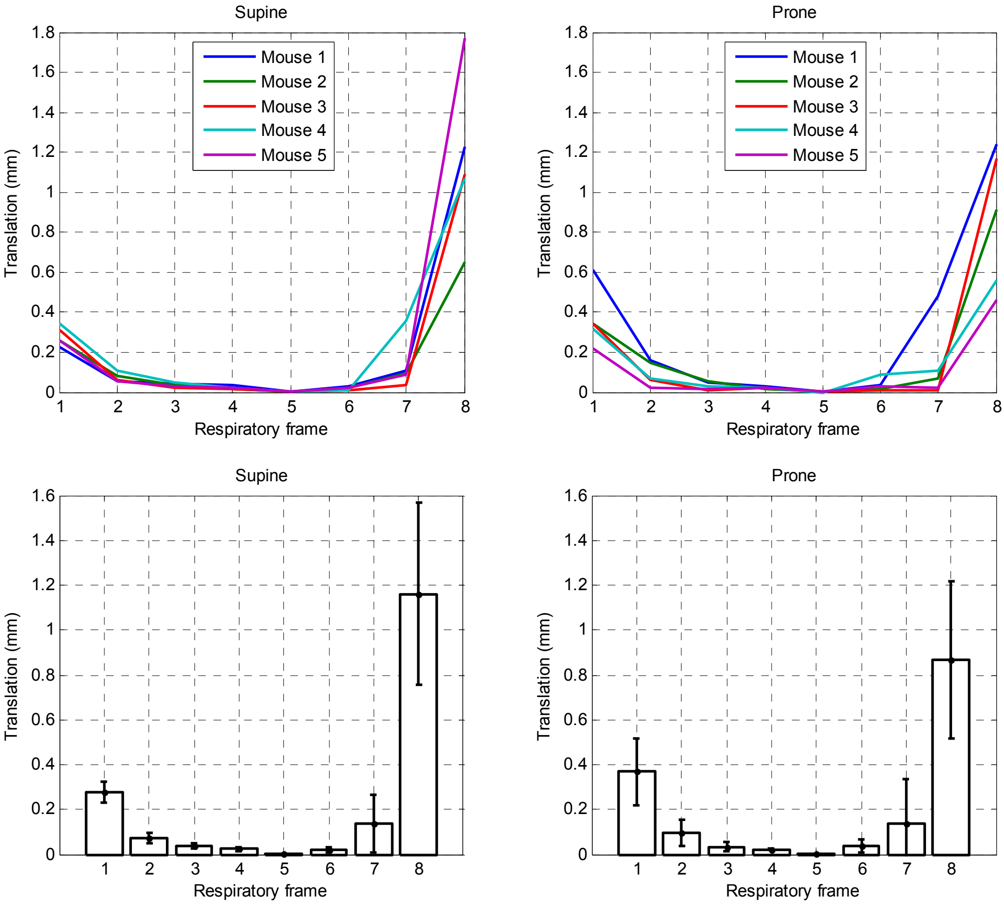

Figure 3.2 Respiratory heart translations of the five mice that were used for respiratory motion correction in the motion-corrected reconstruction method. The translations were calculated by an image registration procedure. Top row: Translations of individual mice in supine and prone positions. Bottom row: Average translations of mice in supine and prone positions. Relatively large translations were found in the 1st and 8th frame.

voxels that were close to heart's apex was higher in the motion-reduced reconstruction than in the other two images which contained counts from all respiratory phases. We suspect that this deviation from the other two reconstruction strategies is a resolution degradation effect due to the relatively low dose that was injected into Mouse 5 (which leads to relatively noisy dual-gated images) in combination with the reduced number of image frames that were used under the motion-reduced reconstruction strategy (which may lead to a more noticeable degraded average image when compared to the average images calculated by using all respiratory phases).

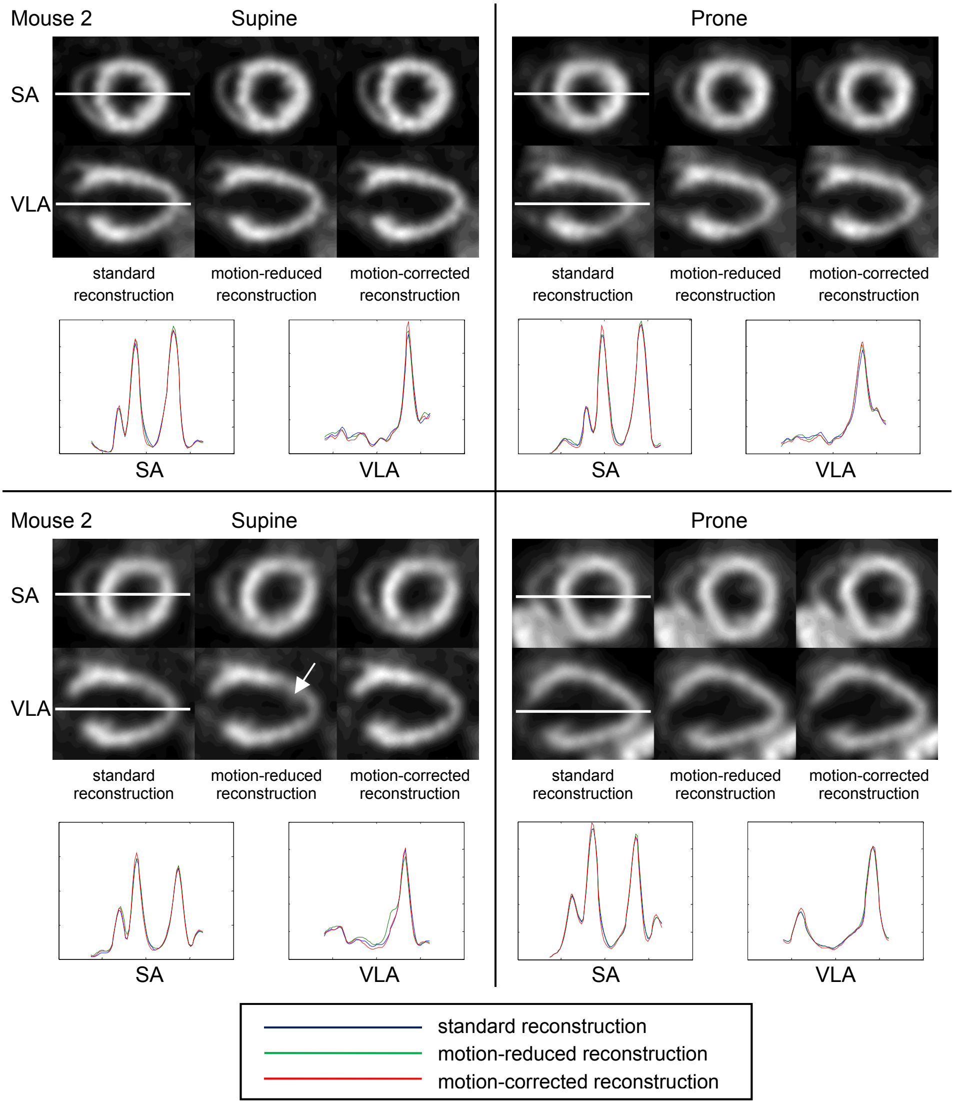

Figure 3.3 SA and VLA slices and line profiles of Mouse 2 and Mouse 5 in supine and prone positions at ED. Images are filtered with a Gaussian kernel (0.7 mm FWHM). For Mouse 5 relatively large differences are indicated by arrows.

3.3.2 Cardiac parameters

We analysed 180 ECG-gated heart images in total resulting from all combinations between the five mice, the two different animal positions, the three reconstruction strategies and the six different Gaussian filter kernels. The average EDV, ESV and LVEF obtained from all

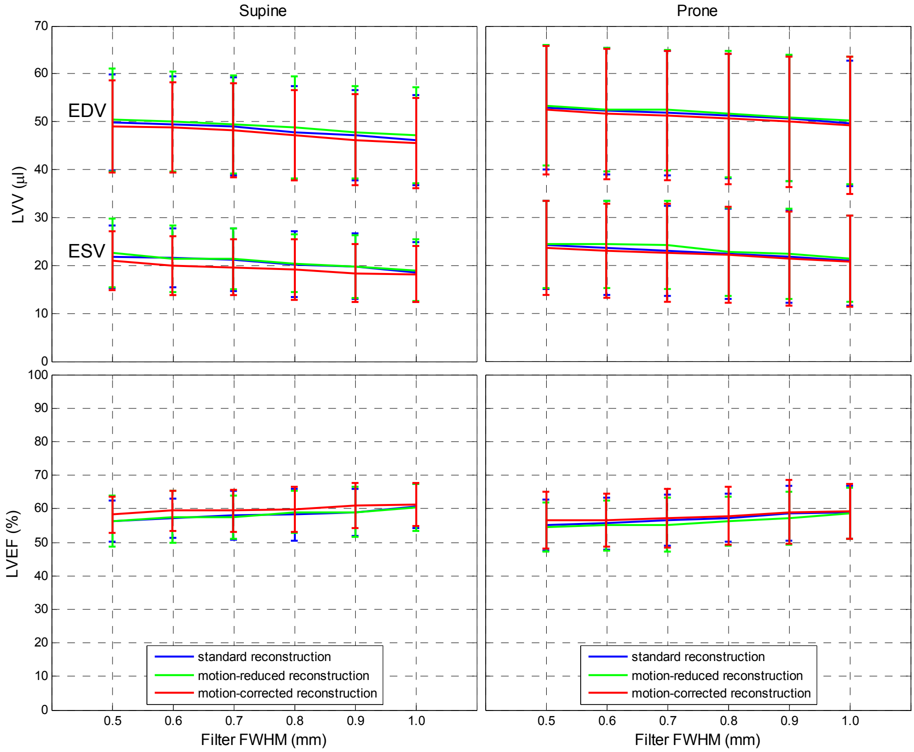

Figure 3.4 Effects of Gaussian filter size on EDVs, ESVs and LVEFs (average of five mice).

standard-reconstruction images filtered with a 0.7 mm FWHM Gaussian kernel were respectively 50±11 µl, 22±8 µl and 57±7%. These values were used as a reference for comparing the relative differences in cardiac parameters caused by the selection of the reconstruction strategies, filter sizes and animal positions.

The 180 ECG-gated heart images were separated into 36 different groups corresponding to different reconstruction strategies, different animal positions and different Gaussian filter kernels. The average EDVs, ESVs and LVEFs over all mice were calculated for each group. The results are plotted in Figure 3.4. It clearly shows that there were barely changes in cardiac parameters induced by the different reconstruction strategies: the largest differences were 1.8 µl for the LVV (3.6% of the reference EDV or 8.6% of the reference ESV) and 2.0% for the LVEF (3.4% of the reference LVEF). The influence of different Gaussian filter kernels was larger: by changing the FWHM from 0.5 mm to 1.0 mm, the LVV decreased by approximately 3.6 µl (7.2% of the reference EDV or 17% of the reference ESV) and the LVEF increased maximally about 4.6% (7.9% of the reference LVEF). The influence of animal positioning was similar: the LVV changed by about 3.8 µl (7.6% of the reference EDV or 18% of the reference ESV) and the LVEF maximally changed 2.8% (4.8% of the reference LVEF).

However, when looking at cardiac parameters of individual mice, we found that the influence of animal positioning on the LVV was variable: e.g. the changes in the LVV of Mouse 2 and 5 were for both within 3 µl due to different reconstruction strategies and within 7 µl, due to different Gaussian filter kernels (Figure 3.5). In contrast, the influence of animal positioning on the LVV was only about 2 µl for Mouse 2 and up to 15 µl for Mouse 5: positioning had a much stronger effect on the LVV for Mouse 5 than for Mouse 2. Cardiac parameter changes caused by different positions for all individual mice can be found in Table 3.1.

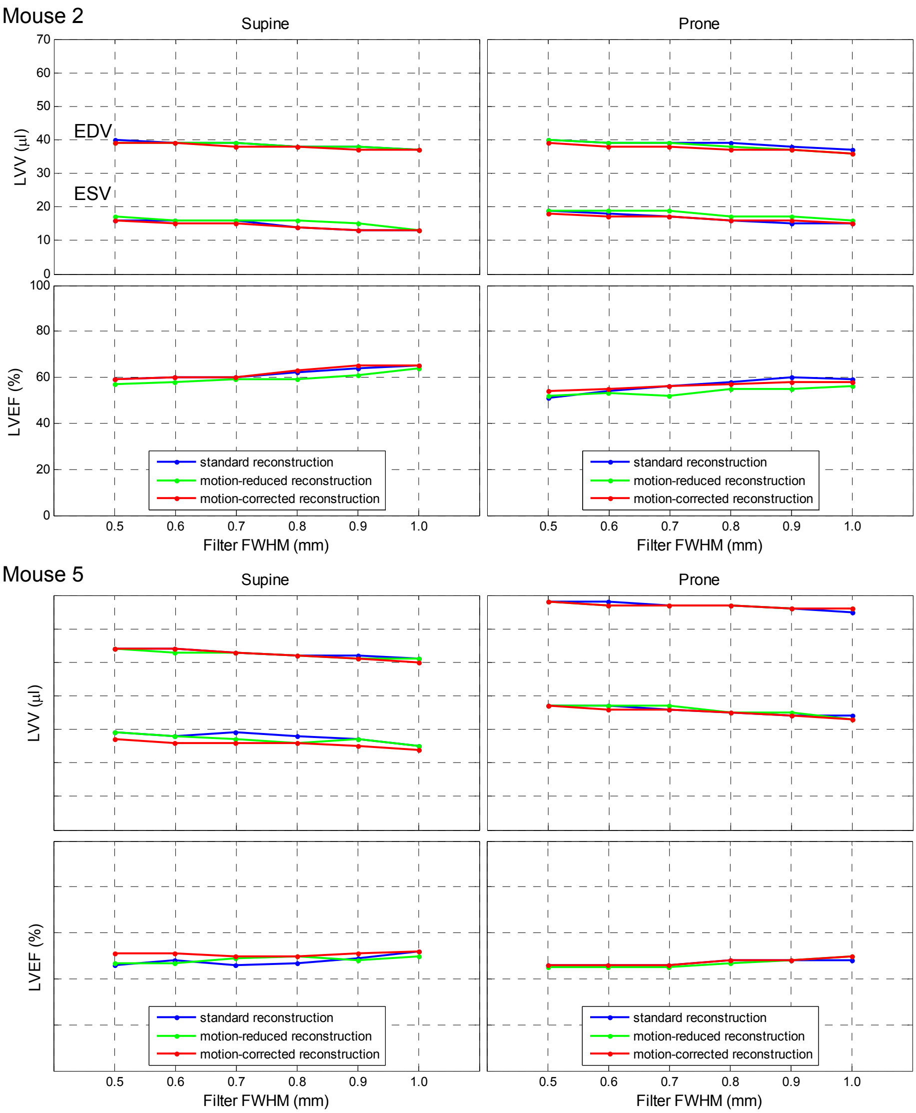

Figure 3.5 Effects of Gaussian filter size on EDVs, ESVs and LVEFs of Mouse 2 and 5.

Table 3.1 Cardiac parameters for all individual mice. The values are averages over the images obtained by applying different reconstruction strategies and spatial filter kernels.

Mouse	Position	EDV (μl)	ESV (μl)	LVEF (%)	Scan order
1	Supine	48	17	64	Prone/Supine
	Prone	57	24	58	
2	Supine	38	15	61	Supine/Prone
	Prone	38	17	55	
3	Supine	41	14	66	Prone/Supine
	Prone	37	12	67	
4	Supine	56	24	58	Supine/Prone
	Prone	64	30	53	
5	Supine	67	35	47	Prone/Supine
	Prone	52	27	49	

3.4 Discussion

In the present study, we reconstructed mice myocardial perfusion images with three different reconstruction strategies in order to study the influence and potential benefit of respiratory gating and motion correction. However, when examining the cardiac images, line profiles and derived cardiac parameters, we found no large changes between the results obtained with the different reconstruction strategies. Moreover, the motion-reduced reconstructions should logically be more similar to the images with respiratory motion correction than the ones without, but this assumption could be rejected by the fact that no such a trend was found for either the average cardiac parameters over all mice or the cardiac parameters of individual mice. None of the strategies showed outstanding results compared to the other strategies. However, the standard reconstruction method is the simplest one to implement.

Image filtering influences the cardiac parameters in a predictable way: the LV wall is increasingly blurred and becomes thicker when larger filter kernels are applied, resulting in a smaller calculated LVV. This effect is similar for the EDV and the ESV. Therefore the stroke volume (SV, equal to EDV−ESV) stays almost unchanged and the LVEF increases (because the LVEF is the quotient of SV and EDV). This is consistent with our data. The rates of change of the EDV and the ESV as a function of the FWHM of the Gaussian filter kernel were respectively −6.7 μl/mm and −6.1 μl/mm (obtained by linear regression). As a result, when taking the average EDV of 50 μl into account, a change in the FWHM of the filter kernel within 0.4 mm would not influence the LVEF by more than 5%.

The influence of animal positioning is somehow puzzling. In clinical studies, the EDV was found lower in prone acquisitions than in supine ones, while other cardiac parameters were barely affected [171]. However in our study, the changes of the measured LVV varied a lot between different animals, ranging from small changes (e.g. Mouse 2: about 2 μl) to large changes (e.g. Mouse 5: about 15 μl). Moreover, we found no clear trend in LVV-change as a function of animal positioning. On the one hand, since the changes induced by respiratory motion correction were small and similar in both supine and prone positioning (about 2 µl), we can hardly say that this variation was caused by different amounts of respiratory motion due to the different positions of the animals. On the other hand, if one considers the positioning order of each mouse between the two scans, it can be noticed that the LVV of four mice increased in their second scan irrespective of their positioning order. Therefore the change of the LVV seems to be caused by inter-scan variations such as tracer accumulation and washout, and/or biological effects resulting from long-time anaesthetization, etc. More experiments are necessary to accept or reject this hypothesis and to investigate which factor(s) cause(s) such inter-scan variations.

The mouse model used in this study may play an important role in future studies as a pre-clinical model for evaluating effects of therapeutics on cardiac function. In the current study ^{99m}Tc-tetrofosmin was used. This tracer enables the quantification of myocardial perfusion and function in a single camera session. In our study we determined the influence of respiratory motion, image filtering and animal positioning on cardiac parameters. This can help researchers to better assess therapeutic effects, while avoiding interference from these factors. There are still other effects such as scatter and attenuation which may influence the measurements, although these effects are very small in mice when clinical tracers are used.

To conclude, even for sub-half-millimetre SPECT, our results indicate that respiratory gating is probably not necessary, and the selection of a specific image filter is not very critical for obtaining reliable cardiac parameters either. However, it could be that when animals that are scanned under different anaesthetic regimes or have compromised pulmonary function, quite different ranges of respiratory motion may occur. In such cases, simultaneous ECG and respiratory gating combined with respiratory motion correction may still be important and useful. Effects of such conditions need further investigations.

3.5 Conclusion

In this paper we found that ECG-gated heart images and derived cardiac parameters such as EDV, ESV and LVEF are barely influenced by applying respiratory motion correction. This can be attributed to the small extent of respiratory motion and the small fraction of the respiratory cycle in which motion occurs when an animal is under anaesthesia. With wider spatial filter kernels cardiac images become smoother, while the LVEF barely changes.

Acknowledgments

This research was partly performed within the framework of CTMM, the Center for Translational Molecular Medicine (www.ctmm.nl), project EMINENCE (grant 01C-204).

We are grateful to Inge Wolterink, Ruud Ramakers (MILabs B.V., Utrecht, the Netherlands), John Buijs and Bart J. Vermolen (University Medical Center Utrecht, the Netherlands) for technical assistance.

Chapter IV

Absolute quantitative total-body small-animal SPECT with focusing pinholes

Chao Wu[1,2,3], Frans van der Have[3,4,5], Brendan Vastenhouw[3,4,5], Rudi A. J. O. Dierckx[1], Anne M. J. Paans[1], Freek J. Beekman[3,4,5]

1 Department of Nuclear Medicine and Molecular Imaging, University Medical Center Groningen, University of Groningen, Groningen, the Netherlands

2 Graduate School for Drug Exploration, University Medical Center Groningen, University of Groningen, Groningen, the Netherlands

3 Image Sciences Institute and Rudolf Magnus Institute, University Medical Center Utrecht, Utrecht, the Netherlands

4 MILabs B.V., Utrecht, the Netherlands

5 Department R3, Section Radiation Detection & Medical Imaging, Delft University of Technology, Delft, the Netherlands

Eur J Nucl Med Mol Imaging (2010) 37:2127–2135
DOI 10.1007/s00259-010-1519-9

Abstract

Purpose: In pinhole SPECT, attenuation of the photon flux on trajectories between source and pinholes affects quantitative accuracy of reconstructed images. Previously we introduced iterative methods that compensate for image degrading effects of detector and pinhole blurring, pinhole sensitivity and scatter for multi-pinhole SPECT. The aim of this paper is (i) to investigate the accuracy of the Chang algorithm in rodents and (ii) to present a practical Chang-based method using body outline contours obtained with optical cameras.

Methods: Here we develop and experimentally validate a practical method for attenuation correction based on a Chang first-order method. This approach has the advantage that it is employed after, and therefore independently from, iterative reconstruction. Therefore, no new system matrix has to be calculated for each specific animal. Experiments with phantoms and animals were performed with a high-resolution focusing multi-pinhole SPECT system (USPECT-II, MILabs, the Netherlands). This SPECT system provides three additional optical camera images of the animal for each SPECT scan from which the animal contour can be estimated.

Results: Phantom experiments demonstrated that an average quantification error of −18.7% was reduced to −1.7% when both window-based scatter correction and Chang correction based on the body outline from optical images were applied. Without scatter and attenuation correction, quantification errors in a sacrificed rat containing sources with known activity ranged from −23.6 to −9.3%. These errors were reduced to values between −6.3 and +4.3% (with an average magnitude of 2.1%) after applying scatter and Chang attenuation correction.

Conclusion: We conclude that the modified Chang correction based on body contour combined with window-based scatter correction is a practical method for obtaining small-animal SPECT images with high quantitative accuracy.

Keywords: quantification, quantitative imaging, small-animal imaging, SPECT

4.1 Introduction

Pinhole SPECT provides high-resolution images of small animals that can be used to quantitatively study the in vivo distribution of a new tracer or drug, for example to determine whether and how molecules reach the target area or what receptors are available in the animal. SPECT can also be employed for function or lesion detection with the help of a wide range of available radiolabelled molecules. In many cases far fewer animals need to be sacrificed in SPECT studies than in post-mortem tissue distribution studies, because SPECT allows for dynamic imaging and longitudinal studies and provides 3D images with slices that are perfectly aligned to each other.

Several dedicated small-animal SPECT systems have been proposed. Most of them (e.g. [10, 21–26, 40, 174]) employ (multi-) pinhole collimation instead of parallel-hole collimation that is used clinically, taking advantage of the magnification of pinholes to improve resolution [13, 40]. Small-animal SPECT images are typically much less degraded by photon scattering and absorption than clinical SPECT images because of smaller body dimensions. Nevertheless, the degradation in small-animal SPECT images is not negligible. For example in the centre of a rat-sized cylinder of water, photon attenuation can reduce the measured concentration of activity up to 25% when imaging with ^{99m}Tc [62]. For clinical SPECT devices several attenuation correction [175–178] and scatter correction methods [55, 61, 177–181] have been developed. Several of these systems are now commercially available and their accuracy has been improved by the availability of integrated SPECT/CT devices [59, 182]. There are few publications about quantitative small-animal SPECT however (e.g. [58, 62, 183]). Recently, Vanhove et al. [65] presented their studies with an average error of −7.9±10.4% between the activity concentrations measured on their scatter- and attenuation-corrected pinhole SPECT mouse images and in a dose calibrator. They used micro-CT imaging for producing attenuation maps, which has the advantage that non-uniformities can be taken into account but at the cost of increased dose to animals and need for additional hardware. Furthermore, the attenuation correction was incorporated in the iterative reconstruction process, which in some reconstruction algorithms may cause problems since they require a new system matrix for each subject to be imaged.

Post-reconstruction attenuation correction algorithms, such as the Chang method, had been proposed decades ago [184]. Their big advantage is that they do not need new system matrices. The first-order correction provided by the Chang algorithm is often not accurate enough for clinical use because effects of attenuation in patients are very strong. The aim of this paper is (i) to investigate the accuracy of the Chang algorithm in rodents and (ii) to present a practical Chang-based method using body outline contours obtained with optical cameras. The method was tested for the case of focusing pinhole SPECT [23, 185] and in combination with correction of other effects such as scatter and distance-dependent collimator blurring and sensitivity.

4.2 Materials and methods

4.2.1 U-SPECT-II: a focusing pinhole small-animal SPECT system

U-SPECT-II [26] is a stationary focusing multi-pinhole SPECT system for small-animal organ and total-body imaging studies. Exchangeable cylindrical collimators containing 75 focusing pinholes can be mounted in the centre and are surrounded by three NaI gamma cameras. Optical photos are acquired by three integrated optical cameras for volume of interest (VOI) selection before SPECT acquisition (Figure 4.1). With an XYZ stage, an animal can be moved inside the collimator during imaging in order to also enable obtaining total-body images.

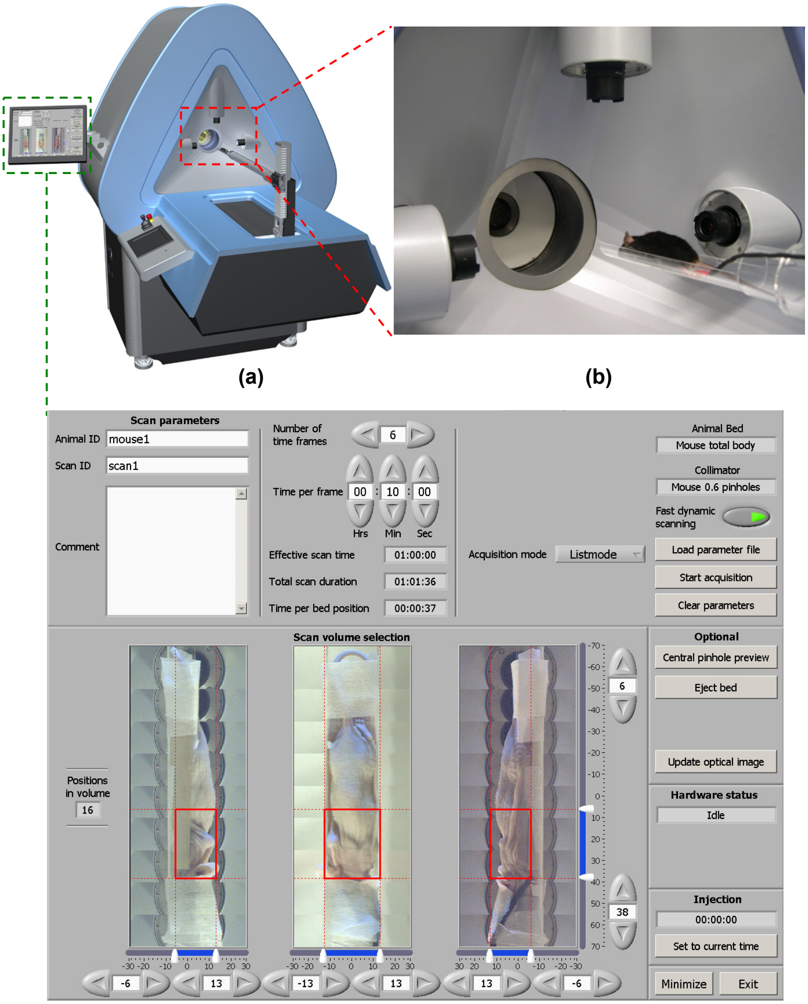

(a)

(b)

(c)

Scan parameters

Animal ID mouse1

Scan ID scan1

Comment

Number of time frames 6

Time per frame 00 : 10 : 00 (Hrs Min Sec)

Effective scan time 01:00:00

Total scan duration 01:01:36

Time per bed position 00:00:37

Acquisition mode Listmode

Animal Bed: Mouse total body

Collimator: Mouse 0.6 pinholes

Fast dynamic scanning

Scan volume selection

Positions in volume 16

Hardware status: Idle

Injection: 00:00:00

Figure 4.1 U-SPECT-II. **(a)** Overview of system. **(b)** Three integrated optical cameras. **(c)** User interface, showing optical photos for VOI selection.

The U-SPECT-II system can reach sub-half-millimetre resolution. With ^{99m}Tc, the image resolution is better than 0.35 mm in any part of a mouse-sized object or better than 0.8 mm in any part of a rat-sized object [26]. With the scanner hardware and acquisition software, the information, including scintillation time, position and photon energy, etc., of every scintillation event is recorded in list mode [26]. This offers great flexibility for image reconstruction, such as implementing decay and spectrum- (e.g. window-) based scatter correction. More detailed descriptions, evaluations and examples of applications of the U-SPECT systems were given in [23, 26, 36, 186].

4.2.2 Image reconstruction

The scanning focus method (SFM) described in [33] was used for acquisition. With the SFM, a total-body scan can be carried out with a sequence of bed positions, and its image can be reconstructed with a single series of iterations. The system matrix used for computing re-projections and back-projections during iterative reconstruction with pixel-based ordered subset expectation maximization (POSEM [32]) is derived from point spread function (PSF) measurements [187]. Within these PSF-based matrices, the effects of the detector blurring, pinhole blurring and pinhole sensitivity are compensated.

4.2.3 Calibration factor

We define the calibration factor to be the ratio of the activity concentration to the voxel value in reconstructed SPECT images. Since the various distance-dependent pinhole sensitivities are already modelled in the system matrix and subsequently compensated in the reconstruction process [187], the calibration factor should be theoretically homogeneous throughout all voxels of reconstructions if attenuation and scatter can be neglected. It means that the calibration factor is a global scaling factor; thus we can obtain the factor by measuring and reconstructing a point source that is almost attenuation free.

We prepared a ^{99m}Tc point source. The activity of the source was 69.0 MBq measured in a VIK-202 dose calibrator. The calibration scan lasted for 200 min, and then a volume of $10\times10\times10$ mm^3 containing the point source in the centre was reconstructed by running 6 POSEM iterations with 16 subsets. Decay effect was compensated during the reconstruction.

The calibration factor, CF, was given by

$$\mathrm{CF} = \frac{A}{V \cdot \sum R} \qquad (4.1),$$

where A is the activity of the point source measured in the dose calibrator, $\sum R$ is the summation of voxel values all over the image and V is the volume of a voxel. If A has a unit of MBq, V is expressed in millilitres, and voxel value R is considered to be dimensionless, then the CF has a unit of MBq/ml.

For scatter- and attenuation-free acquisitions and reconstructions, after scaling by the CF, the voxel values directly represent the activity concentration in those voxels' local regions. However, in practice, scatter correction and attenuation correction should be carried out apart from the global scaling of voxel values.

4.2.4 Scatter correction

In the U-SPECT-II system, scatter correction is integrated into the reconstruction step. Since data are acquired in list mode, scatter and photopeak windows can be set after acquisition. We employed the triple energy window (TEW) technique [188] in both phantom and animal experiments for this paper. A photopeak window (140 keV, 20% width) was used. Two background windows (centred at 117 keV, 10% width and centred at 163 keV, 7% width, respectively) were set adjacent to the photopeak for estimating the number of scattered photons of which the energies ranged inside the photopeak window. The scatter images were scaled by the ratio of the window widths, and added to the estimated scatter-free projections in the denominator of the POSEM formula along the lines proposed in Bowsher et al. [189]. In this way the contributions of scattered photons in projections were taken into account in order to eliminate their detriment to the images as much as possible.

This scatter correction scheme was also performed during the reconstruction of the point source used for obtaining the calibration factor. That scatter needs to be taken into account here is because although probability of scattering inside the point source is quite small, the amount of scattering by the imaging system, especially by the collimator, is not negligible [190, 191]. In a reconstruction of the point source without scatter correction, we found that the calibration factor is 4.35% smaller than the one with scatter correction.

4.2.5 Attenuation correction

The Chang method [184] is a very practical first-order attenuation correction algorithm. It can be implemented as a post-reconstruction processing method, so that no new system matrix is needed. In recent clinical SPECT software, it has often been replaced by more accurate iterative attenuation correction. However, due to the small amount of attenuation in rodents, the Chang algorithm could be sufficient. If the over- and/or under-correction problems of the Chang algorithm can be ignored, the attenuation correction process may benefit from the method's simplicity and high computation speed.

The consequence of attenuation is a reduction in the number of gamma photons which can arrive directly at the detectors, caused by photon scattering and absorption. The amount of attenuation depends on the photon energy, medium properties and the travelling distance of gamma photons in the medium. The transmitted fraction (TF) is therefore represented as

$$\mathrm{TF}_L = \exp\left(-\int_L \mu(l)\mathrm{d}l \right) \qquad (4.2),$$

where L denotes the travelling path of a gamma photon inside the attenuation medium, and μ is the attenuation coefficient. The number of counts detected in that path is then reduced to

$$N = N_0\,\mathrm{TF}_L \qquad (4.3),$$

where N_0 represents the number of counts detected without attenuation.

Chang [184] provided an approximation here: the TF of a voxel over all possible projection paths is the average of all TF_Ls, or

$$\mathrm{TF} = \frac{1}{M}\sum_{m=1}^{M}\exp\left(-\int_{L_m}\mu(l)\mathrm{d}l\right) \quad (4.4),$$

where M is the total number of projections taken in acquisition. In small-animal SPECT, a small M could be sufficient due to the small amount of attenuation. To estimate a sufficiently large M for a rat-sized object, we calculated the TFs with different M on a single slice with an attenuation coefficient of 0.151 cm^{-1} (= μ of 140 keV photon travelling in water) inside an area of an ellipse with its major and minor axes equal to 4 and 2 cm, respectively. Then we took the TFs of the voxels calculated with M = 1024 as reference data and inspected the normalized root mean square deviation (NRMSD) when M is smaller. The results are listed in Table 4.1. We found that by increasing M above 32 gamma ray directions, the NRMSDs are below 0.2%. Therefore, we considered M = 32 as sufficiently large for a rat-sized object and applied it in our studies.

Table 4.1 NRMSD of TFs on an elliptic cross section between different *M* and *M* = 1024.

M	4	8	16	32	64	128	256	512	1024
NRMSD (%)	10.63	1.31	0.29	0.14	0.08	0.04	0.02	0.00	0

An attenuation map was needed to determine the attenuation coefficient μ in different locations of the image volume. In order to simplify the process, we considered the μ to be homogeneous and equal to 0.151 cm^{-1} (= μ of 140 keV photon travelling in water) inside the regions of the objects scanned. In this scheme, only the contour information of the objects was required.

An application program was developed for defining top view and side view 2D contours of animals on the optical photos that standardly are taken before U-SPECT acquisition, e.g. for the purpose of VOI selection and activity localization. As shown in Figure 4.2a, the three optical photos are displayed on the graphical user interface of the software, with a closed Bézier spline curve lying on top of each. The curves are initialized with standard shapes and can be deformed to fit animal outlines by dragging several anchor points. After proper 2D contours were made, the software measured the width p and height q of the animal on the top view and side view contours, respectively, in each position of those transverse slices (Figure 4.2b). Then it created an ellipse of which the horizontal and vertical axes were equal to p and q, respectively, determined by the following equation:

$$\frac{x^2}{p^2} + \frac{y^2}{q^2} = \frac{1}{4} \quad (4.5).$$

All those ordered ellipses were stacked together to form a 3D contour of the object (Figure 4.2c).

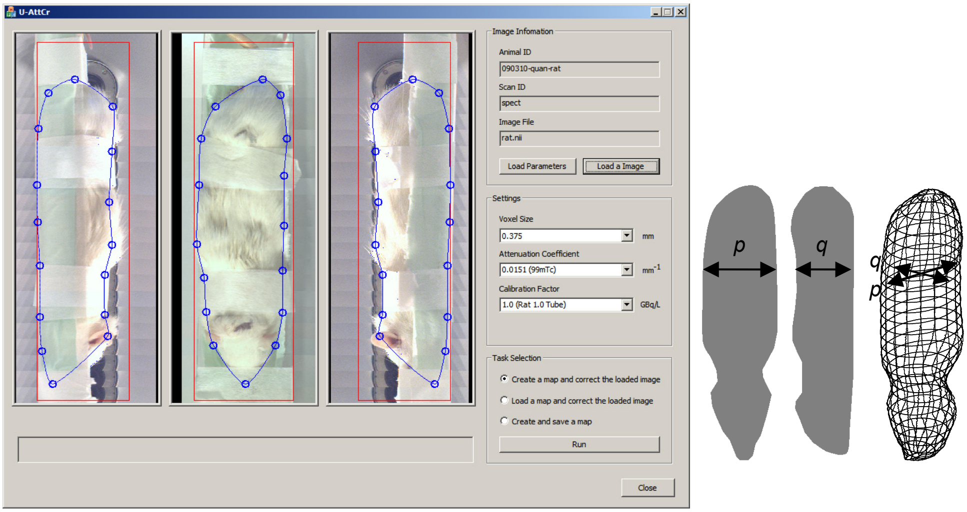

Image Infomation

Animal ID: 090310-quan-rat

Scan ID: spect

Image File: rat.nii

Settings

Voxel Size: 0.375 mm

Attenuation Coefficient: 0.0151 (99mTc) mm^{-1}

Calibration Factor: 1.0 (Rat 1.0 Tube) GBq/L

Task Selection

● Create a map and correct the loaded image
○ Load a map and correct the loaded image
○ Create and save a map

(a) **(b)**

Figure 4.2 Generating a 3D contour. **(a)** Graphical user interface. **(b)** 2D contours. **(c)** A mesh plot of 3D contours based on a stack of ellipses.

4.2.6 Quantification

With this 3D contour and some extra information, such as voxel size and attenuation coefficient μ, the software was able to compute the TF of every voxel:

$$\mathrm{TF} = \frac{1}{32}\sum_{m=1}^{32}\exp\left(-\mu L_m\right) \qquad (4.6).$$

It is important to compute TFs for not only the voxels inside a 3D contour, but also the ones outside. A source can exist outside an attenuation medium, e.g. due to an overly tight body contour, and gamma rays emitted by that source and penetrating the medium will still be attenuated, so that the TFs for that source outside the 3D contour should not be simply set to 1. Another advantage is that it makes the TF change continuously across the border of the contour, which reduces the error brought in by an inaccurate contour.

Finally we computed the activity concentration AC at the location of every voxel of the reconstructed image, with the equation

$$\mathrm{AC} = \frac{R \cdot \mathrm{CF}}{\mathrm{TF}} \qquad (4.7),$$

in which R was the scatter-corrected voxel value.

4.2.7 Experiments

We first used a simple cylindrical phantom to validate the accuracy of absolute quantification with U-SPECT-II. The phantom (45 mm diameter and 40 mm height) was filled with ^{99m}Tc solution with activity concentration equal to 2.88 MBq/ml. The activity was measured by using the VIK-202 dose calibrator. A scan was then performed with USPECT-II, and the image was subsequently reconstructed by using 6 POSEM iterations with 16 subsets, a 0.375-mm voxel size, and with decay and scatter corrections integrated.

A cadaver of a 250 g female Wistar rat was used to test our method in a realistic complex attenuation distribution. Twelve ^{99m}Tc sphere-like sources were made from tips of microcentrifuge tubes (container), cotton balls (solution absorber), ^{99m}Tc solution (radioactive source) and Parafilm (seal). Their diameters were around 5 mm and activities ranged from 7.29 to 9.87 MBq, measured in the same dose calibrator employed in the phantom experiment. These sources were inserted into the rat (mouth, neck, shoulder×2, lung×2, liver, right kidney, intestine, bladder and back×2) by surgery. Then a total-body SPECT scan was carried out. The image was reconstructed by using 6 POSEM iterations combining with 16 subsets and a 0.375-mm voxel size. Decay and scatter corrections were integrated into the reconstruction.

4.3 Results

4.3.1 Phantom experiments

Figure 4.3 shows reconstructed slices of the cylindrical phantom to illustrate the effect of the attenuation correction. The summation of ten transverse slices (decay corrected) without attenuation correction (Figure 4.3a, b) is much darker than with attenuation correction (Figure 4.3c, d), especially in the centre. This can be observed more clearly on the line profiles through the diameters of the phantom along the X direction (Figure 4.3e). The activity concentration measured in the dose calibrator as a gold standard is indicated by a horizontal line at 2.88 MBq/ml.

Without corrections, the difference between the activity concentrations calculated on the reconstructed SPECT image and measured in the dose calibrator was significantly underestimated by −0.54 MBq/ml, or −18.7%. With scatter correction only, the difference worsened to −0.77 MBq/ml (−26.8%). Applying only attenuation correction led to an overestimation by 0.26MBq/ml (9.2%). Applying attenuation correction in combination with scatter correction resulted in a small underestimation of −0.05 MBq/ml (−1.7%). These numbers were calculated on the voxels in a cylindrical volume with a diameter of 42 mm, which was slightly smaller than the phantom size.

4.3.2 Animal experiments

Since the sources inserted into the rat were isolated well, it is possible to segment sub-volumes for individual sources on the reconstructed SPECT image. The activity of each source was calculated by adding all the voxel values in the sub-volume containing that source and then multiplying the resulting sum, the CF, and the voxel size together. Eleven

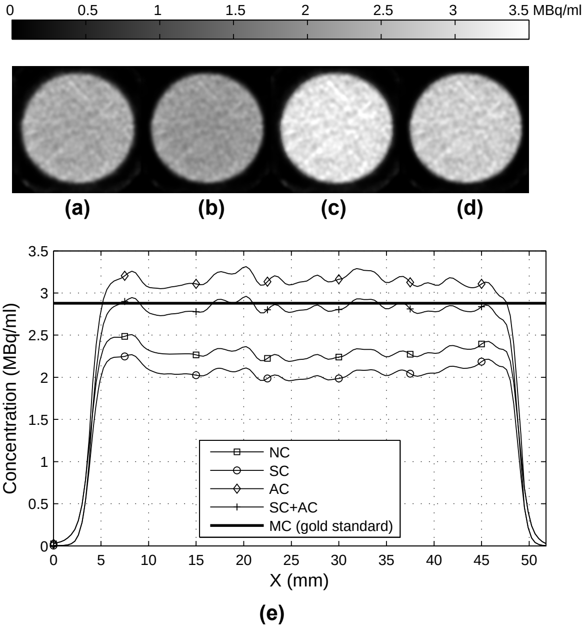

Figure 4.3 Averages of ten transverse SPECT slices of the cylindrical phantom. The grey scales of a–d are the same, from black (0 Mbq/ml) to white (3.5 MBq/ml). **(a)** Without corrections (NC). **(b)** With scatter correction (SC). **(c)** With attenuation correction (AC). **(d)** With scatter and attenuation correction (SC+AC). **(e)** Line profiles through centre of phantom. The line MC indicates the concentration measured with a dose calibrator, as a gold standard.

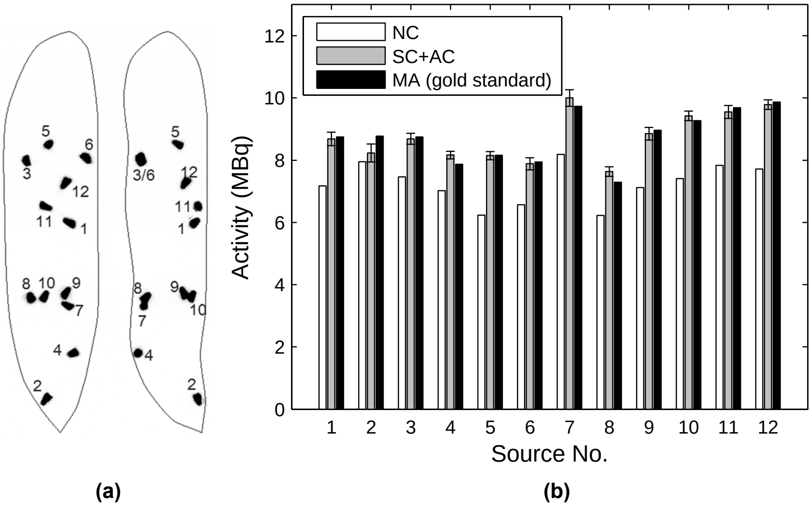

Figure 4.4 **(a)** Planar images showing positions of sources. **(b)** Activities of sources. NC: no correction was performed, SC+AC: scatter and attenuation correction was performed, MA: activities measured by dose calibrator.

volunteers were invited to carry out the attenuation corrections on the reconstructed image individually, using the application program that is shown in Figure 4.2a. After a 15 min training session, all volunteers were able to finish their testing within 5 min. Table 4.2 lists the activities of the sources measured in the dose calibrator and their quantitative results calculated on the decay, scatter and attenuation-corrected image. The averages, standard deviations and percent errors of those results over the 11 testers are also listed.

Table 4.2 Activities of sources measured in dose calibrator and corrected results by 11 individual testers.

Src. No.	Act. (MBq)	Quantified results by eleven individual testers (MBq)											Aver. (MBq)	SD (MBq)	Error (%)
1	8.75	8.91	8.78	9.00	8.43	8.86	8.54	8.69	8.69	8.50	8.31	8.80	8.68	0.21	−0.8
2	8.77	7.92	8.25	8.23	7.82	8.09	8.23	8.38	8.02	8.51	8.18	8.87	8.23	0.29	−6.2
3	8.75	8.82	8.77	8.65	8.80	8.69	8.65	8.22	8.74	8.58	8.73	8.88	8.68	0.18	−0.8
4	7.87	8.07	8.19	8.13	8.25	8.27	7.96	8.34	8.09	8.04	8.33	8.15	8.16	0.12	3.7
5	8.16	8.30	8.15	8.31	8.04	8.25	8.01	8.00	8.23	7.98	8.08	8.26	8.15	0.13	−0.2
6	7.94	8.21	7.94	7.78	7.94	8.03	7.63	7.52	8.02	7.76	7.92	7.97	7.88	0.19	−0.7
7	9.73	10.47	9.87	10.26	10.29	10.00	9.93	9.59	9.62	9.97	10.02	9.99	10.00	0.26	2.8
8	7.29	7.82	7.59	7.82	7.78	7.68	7.60	7.45	7.31	7.63	7.68	7.65	7.64	0.15	4.8
9	8.96	9.19	8.89	9.17	8.81	8.95	8.74	8.61	8.77	8.73	8.56	8.94	8.85	0.20	−1.2
10	9.27	9.63	9.47	9.68	9.39	9.49	9.32	9.29	9.40	9.29	9.17	9.53	9.42	0.15	1.7
11	9.69	9.73	9.66	9.78	9.44	9.60	9.53	9.64	9.54	9.33	9.07	9.71	9.55	0.21	−1.5
12	9.87	9.91	9.88	10.02	9.64	9.97	9.62	9.72	9.84	9.62	9.60	9.85	9.79	0.15	−0.8
Max. error															6.2

Figure 4.4 shows the decay-corrected activities of the sources calculated on the reconstructed SPECT image without and with scatter and attenuation correction, as well as the activities measured in the dose calibrator. The quantification errors on the uncorrected images ranged from −23.6 to −9.3%. With attenuation correction only, these errors of the 11 testers' average results ranged from −1.4 to 10.3%, with an average magnitude of 5.6% over all 12 sources. With scatter and attenuation correction, these errors ranged from −6.3 to +4.3%, and the average magnitude decreased to 2.1%.

4.4 Discussion

Quantification of SPECT imaging in absolute terms becomes possible when physical effects like collimator blurring, sensitivity, scatter and photon absorption are all modelled during iterative reconstruction or compensated afterwards. In clinical SPECT imaging, non-uniform attenuation maps (e.g. from X-ray CT) need to be acquired for accurate quantitative results [178]. Our work shows that attenuation compensation can be performed well in small-animal SPECT applications, despite the fact that no CT scanner was used. Uniform attenuation maps were created with the help of body contour information from optical cameras. At the current stage of this research, the 2D contours were defined manually with deformable closed spline curves on the optical photos. This could possibly be further automated by using certain image processing techniques, such as image segmentation, pattern recognition and an anatomical body contour model.

Experiments were performed to validate our method, first with a simple uniform phantom, and then with a rat cadaver. Although the animal model of a rat with artificial sources is still different from a realistic set-up of preclinical studies (with injections and region of interest measurements, etc.), it is very well suited for evaluating the accuracy of correction methods, since the exact amounts of activity in specific regions of interest are known (which is in contrast to using living animals with a tracer injected). The results from the phantom and animal experiments demonstrated that without compensation an approximately 10–30% underestimation of the activity concentration could be achieved, varying with the diameters of the objects and the depth of the sources. Note that even if the sources were just under the skin of the rat, i.e. the common positions of transplanted tumours for pre-clinical cancer research, there was still more than 10% underestimation. Applying a first-order uniform attenuation correction with the Chang algorithm resulted in accurate quantifications in our experiments, especially when combining together with scatter correction (−1.7% in the phantom study and from −6.3 to +4.3% in the animal study).

In Table 4.2 we notice that the magnitudes of most errors are below 5% except for source No. 2 which has an underestimation of −6.3%. This source was in the rat's mouth and we found that the mouth can be hardly seen on the optical photos, due to the obstruction of the tissue and tape around the rat, which makes the 2D contours at that region uncertain. In fact, the source is not even enclosed with the contours made by 7 of the 11 testers. This apparently leads to an underestimation of the attenuation and thus to a negative bias of the quantitative result. Therefore, we suggest trying to keep a clear sight of the animal contour in a study that requires absolute quantification. On the other hand, the standard deviations of the 11 testers' results are small (≤3%), which supports the observation that the proposed attenuation correction method is not very sensitive to the contour differences introduced by some subjective judgments of individuals.

When imaging with ^{99m}Tc, scatter correction is usually not performed in normal studies due to the small amount of Compton photons within the photopeak window. However, for absolute quantitative studies, it is better to apply scatter correction in order to avoid the overestimation caused by scattered photons. By using attenuation correction in combination with scatter correction, about 7.5 and 3.5% improvement of quantitative accuracy over the accuracy with only attenuation correction was gained in our phantom and rat cadaver experiments, respectively.

There are two things in our experiments which may cause a bias to the results. The first one is the energy window settings of reconstruction. Different photopeak window settings will affect the proportion of gamma counts which contribute to the reconstructed images and thus change the calibration factor. To avoid this we employed the same window settings for all of the reconstructions. The other one is the inaccuracy of the dose calibrator. By using the same dose calibrator to measure the sources for computing the calibration factor and for the validation experiments, the system error, or bias, of the dose calibrator cancels out in the final results of relative errors. However, accurate calibration of the dose calibrator is essential to obtain the exact calibration factor and absolute quantitative results in applications.

In order to simplify our method and to facilitate rapid correction, the pinhole geometry of the U-SPECT-II system and associated attenuation paths were roughly (2D) approximated during the Chang-like attenuation correction. The actual projection paths of a voxel are very complicated considering both the multi-pinhole geometry and the use of multiple bed positions during acquisition. It was shown that this approximation provides good quantitative accuracy in small-animal images. That still good results were obtained can partly be explained by the fact that changes of transmitted fraction due to the length differences between oblique paths and perpendicular paths are small (around 5% at the most).

In clinical studies, the Chang algorithm is known to cause over- and under-correction, and therefore an additional iterative step for compensation is implemented, however at the cost of noise increase. Since in small-animal SPECT the results are accurate without additional iterations, we restricted our method to pure post-reconstruction processing which (i) is much easier to implement and (ii) does not increase noise.

4.5 Conclusion

The effects of attenuation in rat-sized objects are significant. We introduced a contour-based attenuation correction method for small-animal SPECT. To validate this method, phantom and animal experiments were performed and subsequently quantified with a practical software tool by 11 testers. From the results (average error of 1.7 and 2.1% for phantom and animal studies, respectively), we conclude that this body contour-based uniform attenuation correction method derived from the Chang algorithm, in combination with scatter correction, is sufficient for accurate absolute quantification in small-animal SPECT imaging. The information of 3D contours for generating the attenuation maps can be obtained from optical photos instead of from X-ray CT images. This gives opportunities to do absolute quantitative SPECT with stand-alone SPECT systems and to reduce the dose to the animals caused by X-rays which can be limiting in longitudinal studies.

Acknowledgment

We thank Roel Wierts, Sergiy Lazarenko, Marcel Segbers, Jurgen Sijbesma, Norbert Gehéniau, and Paul Hermans for technical support, and Johan de Jong for suggestions and comments.

Chapter V

Quantitative multi-pinhole small-animal SPECT: uniform versus non-uniform Chang attenuation correction

Chao Wu[1,2], Johan R. de Jong[1], Hugo A. Gratama van Andel[2,3], Frans van der Have[2,3,4], Brendan Vastenhouw[2,3,4], Peter Laverman[5], Otto C. Boerman[5], Rudi A. J. O. Dierckx[1], Freek J. Beekman[2,3,4]

1 Department of Nuclear Medicine and Molecular Imaging, University Medical Center Groningen, University of Groningen, Groningen, the Netherlands

2 Rudolf Magnus Institute of Neuroscience, University Medical Center Utrecht, Utrecht, the Netherlands

3 MILabs B.V., Utrecht, the Netherlands

4 Section Radiation, Detection and Medical Imaging, Delft University of Technology, Delft, the Netherlands

5 Department of Nuclear Medicine, Radboud University Nijmegen Medical Centre, Nijmegen, the Netherlands

Phys Med Biol (2011) 56:N183–N193
DOI 10.1088/0031-9155/56/18/N01

Abstract

Attenuation of photon flux on trajectories between the source and pinhole apertures affects the quantitative accuracy of reconstructed single-photon emission computed tomography (SPECT) images. We propose a Chang-based non-uniform attenuation correction (NUA-CT) for small-animal SPECT/CT with focusing pinhole collimation, and compare the quantitative accuracy with uniform Chang correction based on (i) body outlines extracted from X-ray CT (UA-CT) and (ii) on hand drawn body contours on the images obtained with three integrated optical cameras (UA-BC). Measurements in phantoms and rats containing known activities of isotopes were conducted for evaluation. In ^{125}I, ^{201}Tl, ^{99m}Tc and ^{111}In phantom experiments, average relative errors comparing to the gold standards measured in a dose calibrator were reduced to 5.5%, 6.8%, 4.9% and 2.8%, respectively, with NUA-CT. In animal studies, these errors were 2.1%, 3.3%, 2.0% and 2.0%, respectively. Differences in accuracy on average between results of NUA-CT, UA-CT and UA-BC were less than 2.3% in phantom studies and 3.1% in animal studies except for ^{125}I (3.6% and 5.1%, respectively). All methods tested provide reasonable attenuation correction and result in high quantitative accuracy. NUA-CT shows superior accuracy except for ^{125}I, where other factors may have more impact on the quantitative accuracy than the selected attenuation correction.

5.1 Introduction

Small-animal single-photon emission computed tomography (SPECT) and SPECT/CT play an increasingly important role in biomedical research [5–7, 162, 192]. Accurate and highly reproducible results can be obtained, often even without attenuation correction. However, with improved quantitative accuracy, new research applications may come in reach, e.g. since more subtle differences in tissue function can be detected, and efficacy of drugs or radiation therapy can be monitored and compared longitudinally.

Previous phantom studies show that photon attenuation reduces the measured activity concentration in the centre of a rat-sized cylinder containing water by up to 50% when imaging with ^{125}I, and up to 25% with ^{99m}Tc [62]. Simulation studies show that the attenuation can reduce reconstructed tracer concentration by up to approximately 40% for ^{125}I and up to about 20% for ^{99m}Tc and ^{111}In even in mouse-sized phantoms [193]. Therefore, attenuation correction, together with correction for effects such as scatter and camera blurring, is important for obtaining highly quantitative SPECT images.

Effects of attenuation and scatter are much smaller in rodents than in humans. Therefore, practical first-order corrections may be sufficient to achieve accurate quantification. With window-based scatter correction [188] and iterative attenuation correction [194] based on micro-CT images, Vanhove et al. showed that quantitative errors in mouse studies could be reduced to −7.9 ± 10.4% [65]. We recently introduced an optical-contour-based modified Chang method [184] and obtained accurate results as well

(1.7% underestimation on average in a phantom study, and 2.1% error on average in a rat study) [195]. This Chang attenuation correction does not require an object-dependent system matrix for reconstruction. However, a method based on images obtained with optical cameras has some methodological drawbacks compared to inherently automated CT-based attenuation: (i) the attenuation maps assume homogeneous attenuation, and (ii) the default 3D body contour model needs to be adjusted to individual animals by the operator. While uniform attenuation correction leads to reasonably accurate results, CT-based non-uniform attenuation correction should at least in theory further improve the accuracy and reproducibility of quantification.

Recently, commercial pre-clinical micro-SPECT/CT systems have been developed facilitating CT-based non-uniform attenuation correction. This study presents a modified non-uniform Chang method for quantitative small-animal SPECT. This method was tested with data acquired on a U-SPECT-II/CT system (MILabs, Utrecht, the Netherlands) for ^{125}I, ^{201}Tl, ^{99m}Tc and ^{111}In.

5.2 Materials and methods

5.2.1 U-SPECT-II/CT system

The system comprises three stationary detector arrays with multi-pinhole collimators optimized for differently sized rodents with 75 focused pinholes in each cylindrical collimator. For scanning large volumes—up to the entire animal—an XYZ stage shifts the animal during acquisition. Volume images are then obtained during iterative image reconstruction using all acquired data from all bed positions. Evaluations show that with ^{99m}Tc and ^{123}I, the spatial resolution can reach 0.35 mm for mice and 0.8 mm for rats. These values are only slightly degraded with other commonly used SPECT isotopes like ^{111}In [26].

The high throughput CT (SkyScan1178, SkyScan, Kontich, Belgium) comprises a fast circular cone-beam setup dedicated for low-dose scanning with an air-cooled metallo-ceramic tube (voltage range 20–65 kV) and a 1280 × 1024 pixel 12 bit CCD-based detector. The scanning volume is 82 mm in diameter, with 82 mm length for a single scan and up to 212 mm length with multiple scans. The voxel size is 83 or 166 µm.

5.2.2 Data acquisition, image reconstruction and registration

SPECT data were acquired in list mode. Images were reconstructed with the scanning focus method (SFM) [33] and compensation for blurring effects and distance-dependent pinhole sensitivity through accurate system modelling [187]. Reconstruction was accelerated by using pixel-based ordered subset expectation maximization (POSEM) [32] with 16 subsets and 6 iterations.

CT images were reconstructed using a modified Feldkamp algorithm with automatic

Table 5.1 Window settings for ^{125}I, ^{201}Tl, ^{99m}Tc and ^{111}In (low- and high-energy photopeak).

Window (keV ± %)	^{125}I	^{201}Tl	^{99m}Tc	^{111}In (low)	^{111}In (high)
Photopeak	28 ± 40%	72 ± 15%	140 ± 10%	171 ± 10%	245 ± 10%
Background1	14 ± 14.3%	55 ± 9.3%	112 ± 5%	148 ± 3.4%	215 ± 2.3%
Background2	42 ± 4.8%	88 ± 5.7%	168 ± 3.5%	194 ± 2.6%	275 ± 1.8%

adaptation to the scan geometry. Beam hardening and ring artefacts were corrected, and the voxel numbers were converted into Hounsfield units by using a pre-measured calibration factor (CF).

Registration of CT to SPECT images was fully automated using a pre-calculated transformation matrix.

5.2.3 SPECT CF for quantification

CFs were obtained by acquiring SPECT images of small sources with known activity and were used for converting the reconstructed voxel values to activity concentrations. Since the various distance-dependent pinhole sensitivities were already modelled in the system matrix and subsequently compensated in the reconstruction process [187], the CF for each isotope should theoretically be homogeneous throughout all voxels of reconstructions if attenuation and scatter can be neglected. This means that the CF for each isotope is a global scaling factor given by

$$\mathrm{CF} = \frac{A}{V \cdot \sum R} \tag{5.1},$$

where A is the activity of the source measured in a dose calibrator, $\sum R$ is the summation of all voxel values in the reconstructed SPECT image and V is the volume of a voxel. If A has a unit of MBq, V is expressed in ml and the voxel value R is considered to be dimensionless, then the CF has a unit of MBq/ml.

5.2.4 Window-based scatter correction

Scatter is a significant source of error [62, 193]. Therefore, attenuation correction without scatter correction can lead to overestimation of activity [195]. Since effects of scatter in small animals and pinholes are relatively small [190, 191, 196], window-based scatter correction methods [188] are assumed to be sufficient for isotopes such as ^{99m}Tc and ^{111}In [62, 65, 195]. When imaging with ^{201}Tl, high-energy photons emitted by contaminants can scatter in the collimators and detectors, leading to a rather flat background under the photopeak in the spectrum [197]. This can also be corrected with window-based methods.

Since U-SPECT-II acquires data in list mode, photopeak and background windows can be set after acquisition. The window settings configured in our experiments are listed in Table 5.1. The resulting scatter estimate projections were scaled according to the ratio of the window widths, and incorporated in the POSEM reconstruction according to the Bowsher method [189].

5.2.5 Attenuation map

Intensities of registered CT images were rescaled in order to provide non-uniform attenuation maps for ^{125}I, ^{201}Tl, ^{99m}Tc and ^{111}In. Attenuation coefficients (μ) were calculated for each voxel using the following scaling [198]:

$$\mu = \mu_0 \left(\frac{\mathrm{HU}}{1000} + 1 \right) \quad (5.2),$$

where HU is the image intensity in Hounsfield units of a given voxel and μ_0 is the linear attenuation coefficient associated with water and the energy of the photons used in SPECT. μ_0 was obtained by using the NIST data tables [199].

5.2.6 Post-reconstruction attenuation correction

The Chang algorithm [184] is a practical first-order attenuation correction method, which provides an approximation for obtaining the transmitted fraction (TF) for each voxel in reconstructed images. In this method, the TF along every projection line from a certain voxel is calculated, and the average of all these TFs is treated as the overall TF for that voxel:

$$\mathrm{TF} = \frac{1}{M} \sum_{m=1}^{M} \exp\left(- \int_{L_m} \mu(l) \mathrm{d}l \right) \quad (5.3),$$

where M is the number of projections involved in acquisition for data of a certain voxel, L_m denotes the m-th projection path of gamma photons and μ is the attenuation coefficient on that projection line L_m. M was set to 64. For non-uniform attenuation correction, attenuation coefficients were derived from CT images according to Equation (5.2). After the TF of gamma rays for each voxel was estimated, non-uniform attenuation correction was applied:

$$\mathrm{AC} = \frac{U \cdot \mathrm{CF}}{\mathrm{TF}} \quad (5.4),$$

with AC the corrected activity concentration and U the voxel value.

For comparison, two uniform attenuation corrections were performed: (i) based on optical body contours (“UA-BC”) [195] and (ii) based on contours extracted from CT using a threshold (“UA-CT”). Non-uniform attenuation correction with the attenuation coefficients derived from the CT data will be hereinafter referred to as “NUA-CT”.

5.2.7 Phantom experiments

We used the NEMA image quality phantom for small-animal imaging (NEMA NU 4-2008, Figure 5.1a) to validate accuracy of attenuation correction. The phantom consists of a cylindrical fillable chamber (30 mm inside diameter and 30 mm length), and a lid with two empty chambers (10 mm outside diameter and 15 mm length).

The phantom was first filled with $^{99m}TcO_4^-$ solution (8.65 MBq/ml). The activity was measured in the same dose calibrator that was used for the SPECT calibration. Next, SPECT and fully circular CT (60 kV and 615 μA) were performed. SPECT images were reconstructed with decay and scatter correction. The same procedure was repeated for $^{201}TlCl_3$, $^{111}InCl_3$ and $Na^{125}I$ solution, with activity concentrations of 5.90 MBq/ml, 5.91 MBq/ml and 4.54 MBq/ml, respectively.

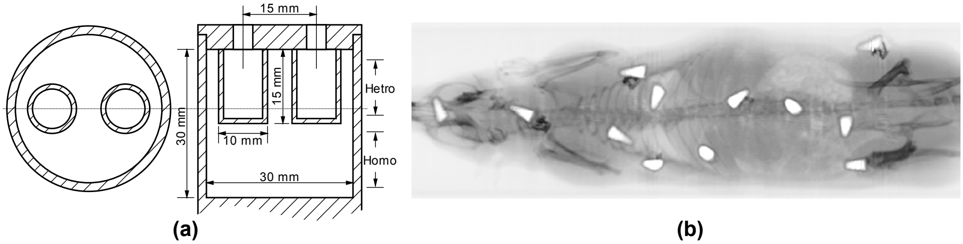

Figure 5.1 (a) Drawing of the NEMA image quality phantom. **(b)** Rat with artificial sources.

5.2.8 Animal experiments

We used four cadavers of female Wistar rats (300–350 g body weight) to test the method with realistic attenuation distributions. For each isotope, 12 small sources with volumes of around 0.2 ml were made from tips of 0.5 ml microcentrifuge tubes (Eppendorf, Hamburg, Germany), radioactive solution and Parafilm (Pechiney Plastic Packaging Company, Chicago, IL, USA). Activities of ^{125}I, ^{201}Tl, ^{99m}Tc and ^{111}In sources ranged from 8.30 to 11.8 MBq, 3.82 to 7.23 MBq, 13.9 to 18.8 MBq and 6.02 to 11.7 MBq, respectively. The activity in the sources was measured in the same dose calibrator. These sources were inserted into the four rats surgically (inside or nearby mouth, neck, left and right lungs, liver, stomach, left kidney, intestine, left and right shoulders, and left and right sides of waist, as shown in Figure 5.1b). Total-body SPECT/CT was performed for each rat.

5.3 Results

5.3.1 Phantom experiments

Figure 5.2 to 5.7 shows 10 mm slices and line profiles of the reconstructed phantom images. Significant differences were found between uncorrected and corrected results, while the contrasts among corrected results with the three different methods were small. The gold standards were activity concentrations measured in a dose calibrator. When UA-BC was

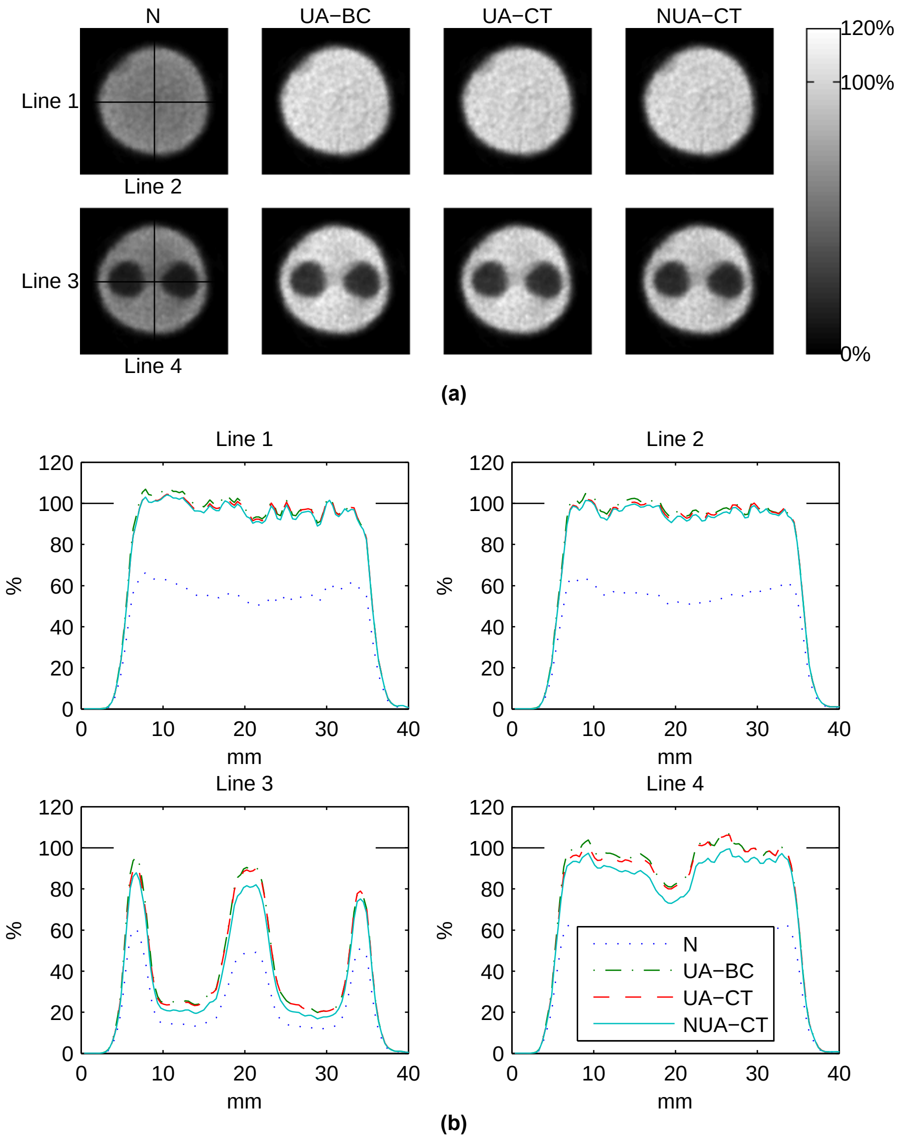

Figure 5.2 Results of ^{125}I phantom. **(a)** Slices without attenuation correction (N), with optical-contour-based correction (UA-BC), with CT-contour-based correction (UA-CT) and with CT-image-based correction (NUA-CT). **(b)** Line profiles through the centre of slices. Note that the gold standard is 100%.

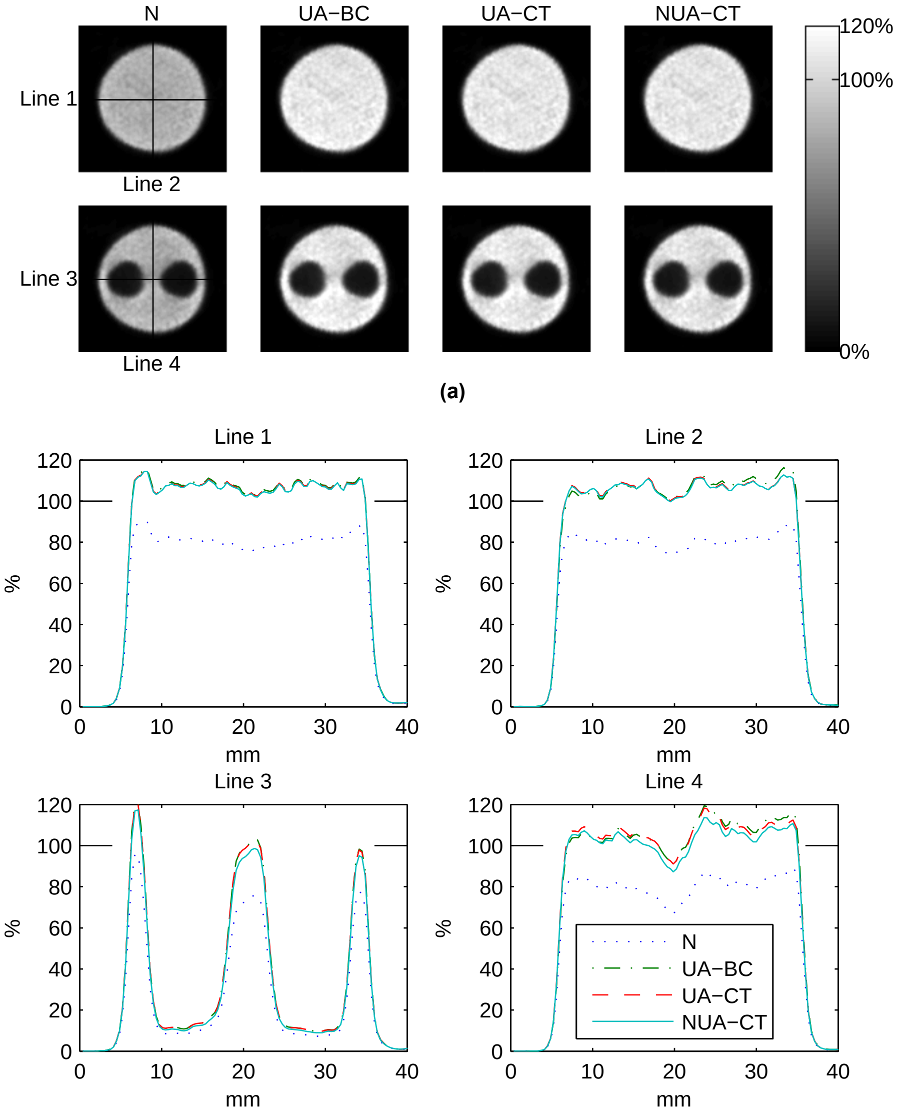

(a)

(b)

Figure 5.3 Results of ^{201}Tl phantom. **(a)** Slices without attenuation correction (N), with optical-contour-based correction (UA-BC), with CT-contour-based correction (UA-CT) and with CT-image-based correction (NUA-CT). **(b)** Line profiles through the centre of slices. Note that the gold standard is 100%.

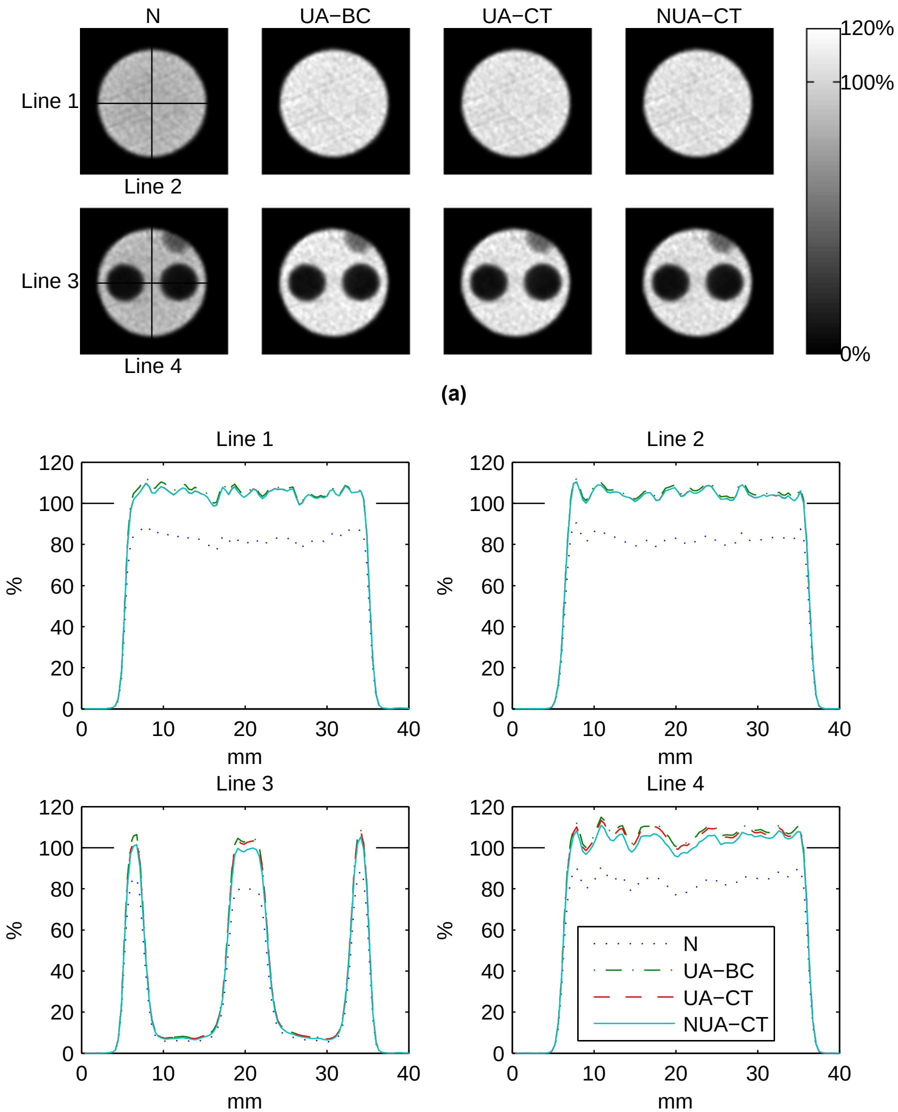

(a)

(b)

Figure 5.4 Results of ^{99m}Tc phantom. **(a)** Slices without attenuation correction (N), with optical-contour-based correction (UA-BC), with CT-contour-based correction (UA-CT) and with CT-image-based correction (NUA-CT). **(b)** Line profiles through the centre of slices. Note that the gold standard is 100%.

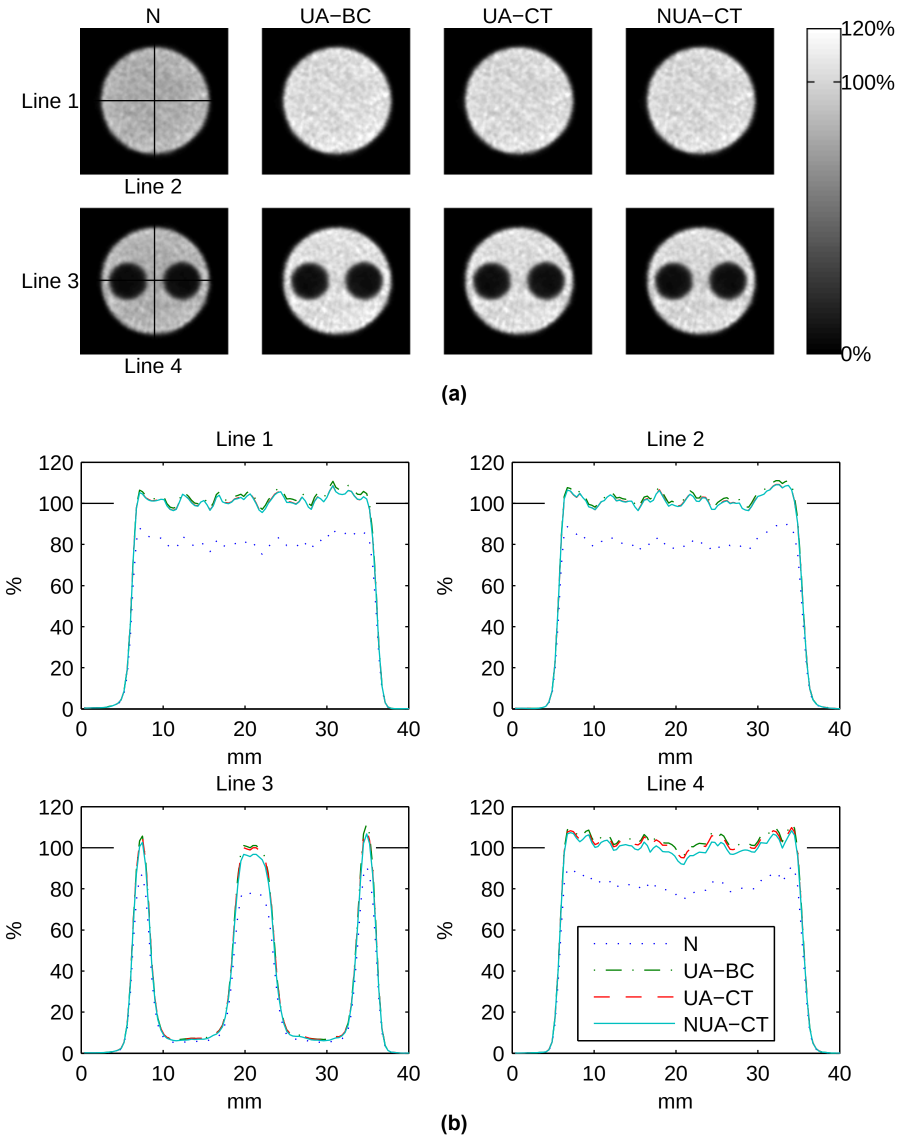

Figure 5.5 Results of ^{111}In phantom (reconstructed by using low-energy photopeak). **(a)** Slices without attenuation correction (N), with optical-contour-based correction (UA-BC), with CT-contour-based correction (UA-CT) and with CT-image-based correction (NUA-CT). **(b)** Line profiles through the centre of slices. Note that the gold standard is 100%.

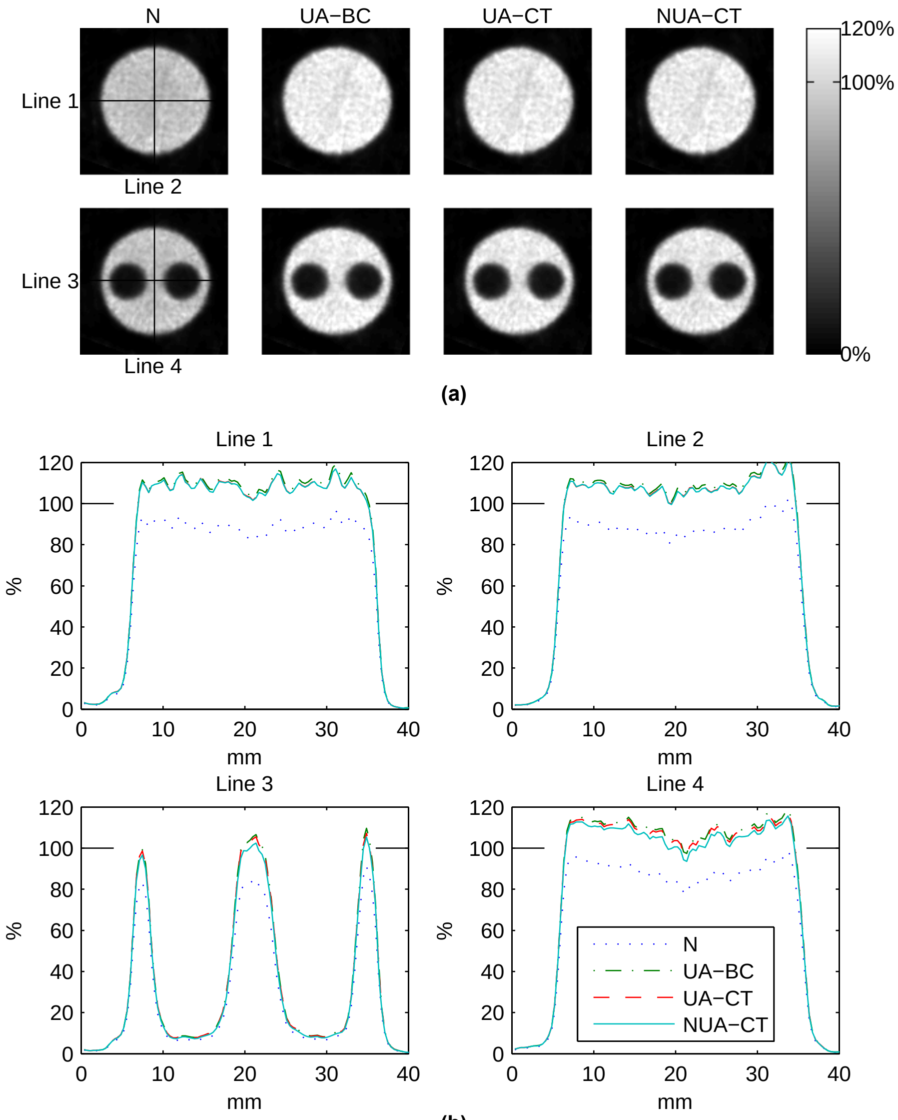

Figure 5.6 Results of ^{111}In phantom (reconstructed by using high-energy photopeak). **(a)** Slices without attenuation correction (N), with optical-contour-based correction (UA-BC), with CT-contour-based correction (UA-CT) and with CT-image-based correction (NUA-CT). **(b)** Line profiles through the centre of slices. Note that the gold standard is 100%.

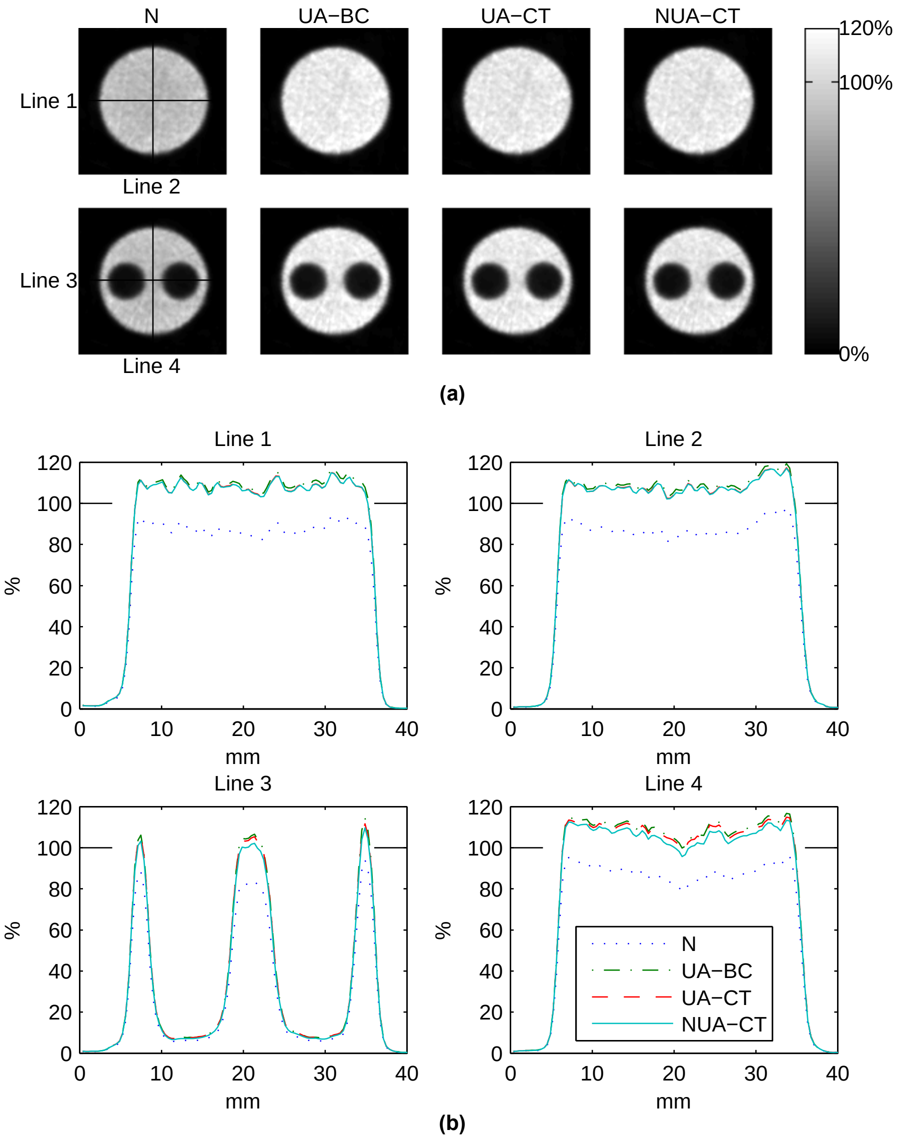

Figure 5.7 Results of ^{111}In phantom (reconstructed by using both photopeaks). **(a)** Slices without attenuation correction (N), with optical-contour-based correction (UA-BC), with CT-contour-based correction (UA-CT) and with CT-image-based correction (NUA-CT). **(b)** Line profiles through the centre of slices. Note that the gold standard is 100%.

used, the deviations from the gold standards were −1.9%, 8.4%, 7.0%, 5.1%, 11.4% and 11.5% for ^{125}I, ^{201}Tl, ^{99m}Tc, ^{111}In (low-energy photopeak), ^{111}In (high-energy photopeak) and ^{111}In (both photopeaks), respectively. These errors were altered to −3.3%, 8.0%, 5.7%, 3.6%, 9.9% and 10.0% with UA-CT, respectively, and to −5.5%, 6.8%, 4.9%, 2.8%, 9.2% and 9.2%, respectively, by using NUA-CT. In contrast, errors of −41.9%, −17.2%, −15.5%, −16.1%, −9.0% and −10.0% were found when no attenuation correction was performed. Besides the overall activity concentrations, we also divided the entire volume into homogeneous and heterogeneous regions (indicated in Figure 5.1a as "Homo" and "Hetro", respectively) and calculated their activity concentrations separately. These results are listed in Table 5.2.

Table 5.2 Quantitative errors of phantom images by using different attenuation correction methods.

Error (in %)	No correction	UA-BC	UA-CT	NUA-CT
^{125}I				
Homogeneous	−42.2	−1.8	−3.2	−4.0
Heterogeneous	−41.5	−2.1	−3.5	−7.9
^{201}Tl				
Homogeneous	−17.7	8.1	7.7	7.3
Heterogeneous	−16.4	8.9	8.6	6.0
^{99m}Tc				
Homogeneous	−16.3	6.0	4.8	4.8
Heterogeneous	−14.0	8.7	7.3	5.1
^{111}In (low)				
Homogeneous	−17.1	4.1	2.5	2.4
Heterogeneous	−14.5	6.7	5.3	3.4
^{111}In (high)				
Homogeneous	−9.6	10.9	9.4	9.3
Heterogeneous	−8.1	12.1	10.7	8.9
^{111}In (both)				
Homogeneous	−10.8	10.8	9.2	9.1
Heterogeneous	−8.6	12.7	11.3	9.4

5.3.2 Animal experiments

Activities in the regions of interest containing the sources in both uncorrected and corrected images were calculated, and compared with the gold standards measured in the dose calibrator. Results are plotted in Figure 5.8 for each source. For ^{125}I, the relative errors of the activities measured on the image without attenuation correction, with UA-BC, with UA-CT and with NUA-CT, were on average −47.0%, 7.2%, 2.3% and 2.1%, respectively. For ^{201}Tl, these errors were −26.8%, 5.5%, 2.7% and 3.3%. For ^{99m}Tc, the same errors were

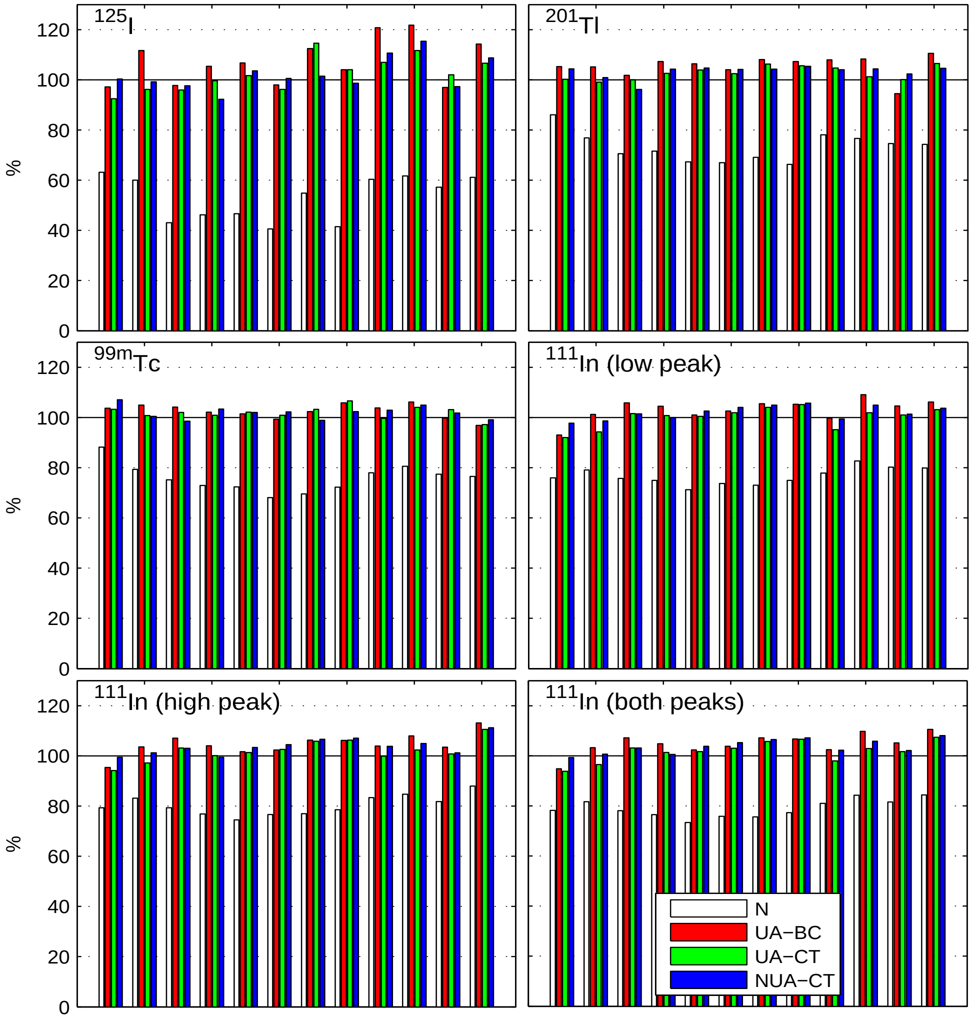

Figure 5.8 Results of animal studies with different isotopes. N: without attenuation correction, UA-BC: with optical-contour-based correction, UA-CT: with CT-contour-based correction and NUA-CT: with CT-image-based correction. Note that the gold standard is 100%.

−24.1%, 2.5%, 2.0% and 2.0%. For ^{111}In (low-energy photopeak), they were −23.4%, 3.2%, 0.1% and 2.0%; for ^{111}In (high-energy photopeak), they were −19.8%, 4.6%, 2.0% and 3.8%; and for ^{111}In (both photopeaks), they were −21.0%, 4.8%, 1.8% and 3.7%, respectively. These values are listed in Table 5.3 together with standard deviations of the relative errors.

Table 5.3 Quantitative errors of rat images by using different attenuation correction methods.

Error (in %)	No correction	UA-BC	UA-CT	NUA-CT
^{125}I				
Average	−47.0	7.2	2.3	2.1
Standard deviation	8.8	9.0	6.7	6.5
^{201}Tl				
Average	−26.8	5.5	2.7	3.3
Standard deviation	5.7	4.2	2.6	2.5
^{99m}Tc				
Average	−24.1	2.5	2.0	2.0
Standard deviation	5.5	2.8	2.4	2.5
^{111}In (low)				
Average	−23.4	3.2	0.1	2.0
Standard deviation	3.4	4.1	4.1	2.7
^{111}In (high)				
Average	−19.8	4.6	2.0	3.8
Standard deviation	4.0	4.2	4.3	3.4
^{111}In (both)				
Average	−21.0	4.8	1.8	3.7
Standard deviation	3.6	4.1	4.1	2.9

5.4 Discussion

In the present study, a Chang-based non-uniform attenuation correction method was developed and its impact on the accuracy of quantitative analysis of SPECT images was determined. For the standard small-animal NEMA image quality phantom, the underestimation of activity concentration due to photon attenuation ranged from 9.0% to 41.9% for different isotopes when no correction was applied, which was in line with [193]. With each of the three attenuation correction methods, the relative error reduced to less than 10% except for the ^{111}In high-energy-photopeak and ^{111}In both-photopeak images. There was a trend towards a slight overestimation in images involving the ^{111}In high-energy photopeak. This is because the system matrices were made from scans with ^{99m}Tc. The 245 keV photons emitted by ^{111}In have a higher possibility of penetrating the collimator directly, which is not yet accurately modelled in the system matrices. In this sense, although ^{111}In images are usually reconstructed using both photopeaks to increase the signal-to-noise ratio, especially when the number of counts collected is not high enough, it may be better to use only the low-energy photopeak for quantitative purposes in studies with sufficiently high activity. Future investigations about optimal window-settings and correction of ^{111}In images at different count levels may lead to further improvement of quantification for ^{111}In imaging.

For ^{125}I, ^{201}Tl, ^{99m}Tc and for the ^{111}In low-energy-photopeak data, differences of the average accuracy after attenuation correction by using UA-BC and UA-CT were between 0.4% and 1.5%. Since these two methods use exactly the same algorithm, the differences in the results can only be explained by the differences of contour extraction. Use of the CT contours led to slightly more accurate results except for ^{125}I.

When comparing UA-CT and NUA-CT, we can see that in the homogeneous region of the phantom, the two methods lead to similar results (difference <0.8%). However, in the heterogeneous region, NUA-CT is superior to UA-CT for ^{201}Tl, ^{99m}Tc and ^{111}In low-energy-photopeak images, though differences are small (<2.6%). This could be explained by the uniform and non-uniform TF maps calculated from the different methods. Taking the TF maps for ^{99m}Tc as an example (Figure 5.9), the TFs of about three quarters of the voxels have differences less than 2% between the uniform and non-uniform maps. The largest difference was less than 6.9% and was located in the air-filled chambers. For ^{125}I, because the amount of attenuation is higher than for the other isotopes, the difference in results between using NUA-CT and UA-CT is also higher, about 4.4% on average.

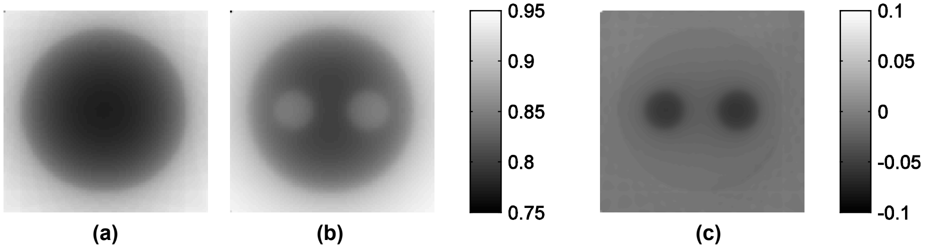

Figure 5.9 TF maps of heterogeneous phantom slice for ^{99m}Tc calculated by using **(a)** UA-CT and **(b)** NUA-CT. **(c)** is (a) − (b).

Only the attenuation-corrected ^{125}I images suffered from underestimation. Quantitative accuracy was the best for UA-BC and worst for NUA-CT. This may be caused by errors in scatter correction and reconstruction. The coherent scattering of low-energy photons cannot be simply corrected by using the energy-window-based method. Therefore, part of the activity was wrongly attributed to the air-filled chambers (Figure 5.2b), and consequently reconstructed activity in the solution-filled area decreased. In addition, some distortions in the shape of the phantom were observed in the ^{125}I and ^{201}Tl images (Figure 5.2a and 5.3a). This can be explained by the fact that the system point spread functions (PSFs) were calibrated with ^{99m}Tc. We expect that more extensive calibration with different isotopes or correction of PSFs for the photon energy (e.g. along the lines in [34]) will further improve the results. However, note that neither of these approaches is trivial to implement.

In rat cadavers, we obtained quantitative errors in un-corrected images which again were in line with experiments in [62]. As expected, UA-BC gave the worst (but still quite accurate) estimation of the activities. Comparing with UA-CT that uses more accurate contours, we found that the estimations of attenuation by using UA-BC were higher. This means that the hand-draw contours may have been drawn too loose, which may be caused by the fur of the rats. Surprisingly, UA-CT performed as well as NUA-CT.

The Chang algorithm, either uniform or non-uniform, is a first-order approximation. We expect that the quantitative accuracy would progressively increase by using UA-BC, UA-CT and NUA-CT. This coincides with the phantom-experiment results quite well. However, in the rat studies, the advantage of NUA-CT is not obvious comparing to UA-CT. One reason could be that there are no large structures with higher or lower density than soft tissue in the rat bodies, unlike in the heterogeneous region of the phantom. The volume containing bones is small, and the air content of the lungs was low, since the rats were euthanized before the scans. In studies with living animals, the effect of non-uniform attenuation correction will be somewhat larger. Otherwise, noise and artefacts in CT images may cancel out part of the benefit from non-uniform attenuation correction.

The linear scaling that we have used for translating CT numbers to attenuation coefficients is an approximate approach. However, it has the advantage that no extra CT measurements with dense materials are required. This linear approach seems to be sufficient for accurate attenuation correction in small animals, likely because of the small dimension of bone structure. If any significant improvements can still be made needs to be tested in future experiments.

5.5 Conclusion

We introduced a CT-image-based first-order Chang method for non-uniform attenuation correction in SPECT with focusing pinholes. Phantom and animal experiments were conducted with different isotopes (i.e. ^{125}I, ^{201}Tl, ^{99m}Tc and ^{111}In). Results were compared with two uniform attenuation correction methods based on contours extracted from optical images or CT images. We conclude that all the three methods allow accurate absolute quantification in small-animal SPECT, while the CT-based methods improve the accuracy as compared to the optical-contour-based one. It is a good choice just to use the optical-contour-based method for small-animal studies in which quantification is needed but no CT scans are available. When CT images are used, the creation of the attenuation maps is slightly more accurate and is automated, which can save time and operator training for drawing the contours.

Acknowledgment

We are grateful to Bianca Lemmers-de Weem (Central Animal Facility, Radboud University Nijmegen, Nijmegen, the Netherlands) for technical assistance.

Chapter VI

Effects of attenuation map accuracy on attenuation-corrected micro-SPECT images

Chao Wu[1,2], Hugo A. Gratama van Andel[2,3], Peter Laverman[4], Otto C. Boerman[4],
Freek J. Beekman[1,3]

1 Section Radiation, Detection & Medical Imaging, Delft University of Technology, Delft, the Netherlands

2 Rudolf Magnus Institute of Neuroscience, University Medical Center Utrecht, Utrecht, the Netherlands

3 MILabs B.V., Utrecht, the Netherlands

4 Department of Nuclear Medicine, Radboud University Nijmegen Medical Centre, Nijmegen, the Netherlands

EJNMMI Research (2013) 3:7
DOI 10.1186/2191-219X-3-7

Abstract

Background: In single-photon emission computed tomography (SPECT), attenuation of photon flux in tissue affects quantitative accuracy of reconstructed images. Attenuation maps derived from X-ray computed tomography (CT) can be employed for attenuation correction. The attenuation coefficients as well as registration accuracy between SPECT and CT can be influenced by several factors. Here we investigate how such inaccuracies influence micro-SPECT quantification.

Methods: Effects of (i) misalignments between micro-SPECT and micro-CT through shifts and rotation, (ii) globally altered attenuation coefficients and (iii) combinations of these were evaluated. Tests were performed with a NEMA NU 4-2008 phantom and with rat cadavers containing sources with known activity.

Results: Changes in measured activities within volumes of interest in phantom images ranged from <1.5% (^{125}I) and <0.6% (^{201}Tl, ^{99m}Tc and ^{111}In) for 1 mm shifts to <4.5% (^{125}I) and <1.7% (^{201}Tl, ^{99m}Tc and ^{111}In) with large misregistration (3 mm). Changes induced by 15° rotation were smaller than those by 3 mm shifts. By significantly altering attenuation coefficients (±10%), activity changes of <5.2% for ^{125}I and <2.7% for ^{201}Tl, ^{99m}Tc and ^{111}In were induced. Similar trends were seen in rat studies.

Conclusions: While getting sufficient accuracy of attenuation maps in clinical imaging is highly challenging, our results indicate that micro-SPECT quantification is quite robust to various imperfections of attenuation maps.

Keywords: molecular imaging, SPECT, CT, small animal, misregistration, attenuation correction, quantification

6.1 Background

Small-animal single-photon emission computed tomography (micro-SPECT) plays an increasingly important role in biomedical research [5–7, 162, 192, 200–203]. Attenuation correction, together with correction for effects such as scatter and camera blurring, is essential for obtaining highly quantitative SPECT images. Efforts have been made to improve quantitative accuracy in micro-SPECT. For instance, Hwang et al. [58] and Vanhove et al. [65] showed that by using attenuation maps derived from micro-CT data, cupping artefacts in micro-SPECT images could be eliminated and quantitative errors could be reduced with iterative attenuation correction [194] and window-based scatter correction [188] methods. We recently introduced an optical-contour-based modified Chang method [184] for attenuation correction in multi-pinhole SPECT, which is applied post-reconstruction and leads to small quantitative errors (1.7% and 2.1% on average in phantom and rat studies with ^{99m}Tc, respectively) [195]. This method was later extended to a CT-based non-uniform attenuation correction and tested with four different isotopes on a micro-SPECT/CT system [204]. Average quantitative errors of 2.1%, 3.3%, 2.0% and 2.0% in activities of sources implanted in rat cadavers were achieved for ^{125}I, ^{201}Tl, ^{99m}Tc and ^{111}In, respectively.

In clinical SPECT, problems caused by inaccurate attenuation maps have been thoroughly investigated. For example, Tonge et al. [205, 206] indicated that even minor degrees of misregistration (a couple of millimetres) between SPECT and CT can create significant artefacts. Goetze et al. [207] found that misregistration of less than 1 cm contributed significantly to changes in myocardial perfusion images. Studies of e.g. Kennedy et al. [208] found misregistration of more than 3.4 mm in 73% of clinical SPECT/CT studies. Such studies even raised the question whether attenuation correction should be applied to clinical myocardial perfusion SPECT. Results about attenuation map inaccuracies and their effects on quantitative accuracy for clinical SPECT cannot be directly translated to micro-SPECT studies because of e.g. higher resolution, different anatomies and less attenuation in micro-SPECT studies. Since anatomical images from external scanners are often combined with micro-SPECT, registration and scaling issues occur quite often. Therefore, knowledge about required attenuation map accuracy is highly important.

The aim of the present study is to investigate the effects of attenuation map imperfections on the accuracy of micro-SPECT quantification. Two main sources of attenuation map inaccuracies were emulated: (i) misalignments between micro-SPECT and micro-CT images, e.g. as could result from misregistration or animal movement; and (ii) global errors in the attenuation coefficients derived from micro-CT data, e.g. as could result from sub-optimal CT calibration.

6.2 Method

Animal studies involved in this study were conducted following the regulations approved by the Animal Experiment Committee of the Radboud University Nijmegen.

6.2.1 Phantom and animal imaging in U-SPECT-II/CT

The U-SPECT-II/CT system used in the present study (MILabs, Utrecht, the Netherlands; Figure 6.1) comprises three stationary gamma cameras equipped with different cylindrical multi-pinhole collimators optimized for differently sized rodents, each containing 75 focused pinholes. An XYZ stage shifts the animal during acquisition for scanning large volumes up to the entire animal. The integrated high-throughput micro-CT comprises a fast circular cone-beam setup dedicated for low-dose scanning with an air-cooled metallo-ceramic tube (voltage range 20 to 65 kV) and a 1280 × 1024 pixel 12-bit CCD-based detector. Performance of this system is described in [26, 195, 204, 209–212].

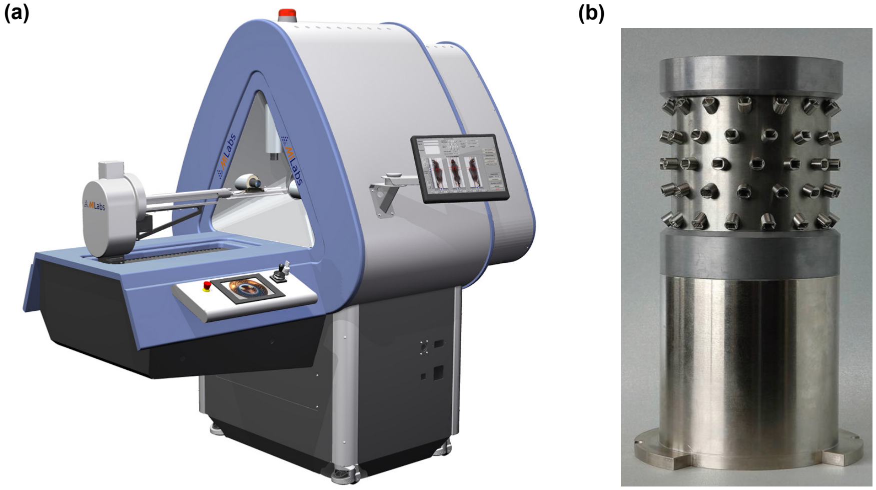

Figure 6.1 Images of the system and rat collimator used in the present study. **(a)** U-SPECT-II/CT multi-pinhole system and **(b)** rat collimator.

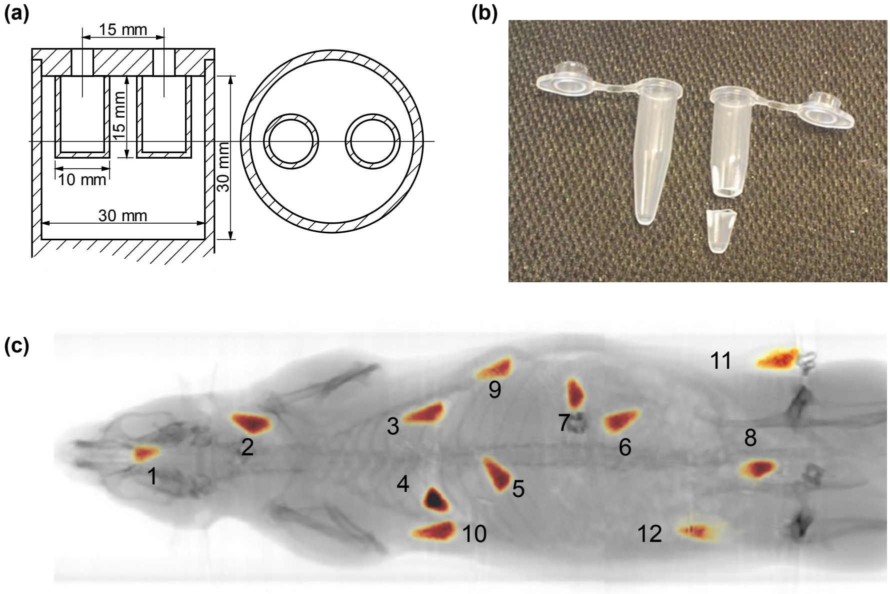

Figure 6.2 NEMA image quality phantom, microcentrifuge tube and rat body showing ^{99m}Tc sources. **(a)** Drawing of NEMA image quality phantom, **(b)** 0.5 ml microcentrifuge tube and its tip for making sources (sealed with Parafilm (Pechiney Plastic Packaging Company, Chicago, IL, USA) afterwards) used in the rat study and **(c)** rat with numbered ^{99m}Tc sources with known activity.

A NEMA image quality phantom for small-animal imaging (NEMA NU 4-2008, NEMA, Rosslyn, VA, USA; Figure 6.2a) with two small air-filled chambers was first filled with $^{99m}TcO_4^-$ solution (8.65 MBq/ml). The activity was measured in a dose calibrator. Next, SPECT and fully circular CT (60 kV and 615 μA) were performed. Then, the same procedure was repeated for $^{201}TlCl_3$, $^{111}InCl_3$ and $Na^{125}I$ solutions, with activity concentrations of 5.90 MBq/ml, 5.91 MBq/ml and 4.54 MBq/ml, respectively. In addition, 12 small ^{99m}Tc sources (approximately conical, about 6 mm in length and 3 mm in average diameter, and made from tips cut from 0.5 ml microcentrifuge tubes; Figure 6.2b) with known activity were inserted into a cadaver of a female Wistar rat surgically (inside or near the mouth, neck, left and right lungs, liver, stomach, left kidney, intestine, left and right shoulders, and left and right sides of the waist, as shown in Figure 6.2c). Total-body SPECT/CT was performed for the rat. This was repeated with three other rat cadavers for ^{125}I, ^{201}Tl and ^{111}In. Activities of the ^{125}I, ^{201}Tl, ^{99m}Tc and ^{111}In sources ranged from 8.30 to 11.8 MBq, 3.82 to 7.23 MBq, 13.9 to 18.8 MBq and 6.02 to 11.7 MBq, respectively.

SPECT images were reconstructed by using the scanning focus method [33] combined with pixel-based ordered subset expectation maximization [32] using 16 subsets, 6 iterations and a 0.375 mm voxel grid, during which blurring and pinhole sensitivity effects were corrected [187] and an energy-window-based scatter correction method was implemented [188]. CT images were reconstructed with a 0.169 mm voxel grid, using NRecon (SkyScan, Kontich, Belgium) with its built-in modified Feldkamp algorithm and methods for beam hardening and ring artefact corrections. Both SPECT and CT images were rescaled with pre-measured calibration factors, and then SPECT images were registered to CT images by means of rigid transformations with pre-determined matrices.

More details on system calibration, phantom and animal preparation, data acquisition, image reconstruction, scatter correction and SPECT–CT registration have been described in [204].

6.2.2 CT-based non-uniform attenuation correction for micro-SPECT

The Chang algorithm [184] is a practical attenuation correction method, which provides an approximation for obtaining the transmitted fraction (TF) for each voxel in reconstructed images. Being a post-reconstruction correction method, the Chang algorithm does not require generation of additional SPECT system matrices that each takes up tremendous amounts of memory and computation. Therefore, the Chang algorithm can be easily applied to images acquired from any micro-SPECT system. This algorithm has been shown to lead to highly accurate results [195, 204] which can be attributed to the fact that (in contrast to clinical SPECT) only small corrections are required in rodents, justifying the use of this first-order method (in clinical SPECT, iterative attenuation correction is highly preferred while memory demands are different). Details about implementation of the modified Chang algorithm for multi-pinhole SPECT are found in [204]. In brief, the TF along every projection line from a certain voxel is calculated, and the average of all these TFs is treated as the overall TF for that voxel:

$$\mathrm{TF} = \frac{1}{M}\sum_{m=1}^{M}\exp\left(-\int_{L_m}\mu(l)\mathrm{d}l\right) \qquad (6.1),$$

where M is the number of projections involved in acquisition for data of a certain voxel, L_m denotes the m-th projection path of gamma photons and μ is the attenuation coefficient on that projection line L_m. Attenuation coefficients were derived from CT images by linear scaling [198]:

$$\mu = \mu_0\left(\frac{\mathrm{HU}}{1000}+1\right) \qquad (6.2),$$

in which HU is the CT image intensity in Hounsfield units, and μ_0 is the linear attenuation coefficient associated with water and the energy of the photons used in SPECT. μ_0 was obtained using the NIST data tables [199]. In case that more than one photon energy was involved, μ_0 was chosen to be the average of $\mu_0(E)$ weighted by the number of photons detected under each energy E. When the TF for each voxel was estimated, the attenuation was compensated by dividing each voxel value by its corresponding TF [204].

6.2.3 Attenuation correction with different attenuation maps

For each scan, an attenuation coefficient map was created from the registered CT image by linear scaling as in Equation (6.2) and then converted to a transmitted fraction map with the non-uniform Chang algorithm as described in Equation (6.1). To only evaluate the impact of inaccuracies in attenuation maps on the SPECT quantification, we considered these original attenuation maps to be accurate, and thus, we used the SPECT images corrected with these maps as reference images. Meanwhile, quantitative errors, i.e. differences between activities measured in images and in a dose calibrator, were also calculated for each reference image for reasons of comparison.

To investigate the effect of misregistration, we shifted the original TF maps for phantom studies in either $+x$ (towards the right side of the system) or $+y$ (downwards) direction and the maps for animal studies in $+x$, $+y$ or $+z$ (towards the back side of the system) direction. The distances of shifting in each direction were set to 1 mm and 3 mm. All original TF maps were also rotated anticlockwise by 15° to emulate the consequences of animal movement during scans. All these shifted and rotated TF maps were used for attenuation correction of their corresponding SPECT images. Later on, we globally changed the attenuation coefficients in the attenuation maps by ±10% of the original values. This was to emulate errors introduced by CT itself and/or from converting CT values to attenuation coefficients. TF maps were again calculated with the non-uniform Chang algorithm from these altered attenuation maps and then used for correcting for attenuation in their corresponding SPECT images. As a final test, the TF maps calculated with the +10% attenuation coefficient maps were also rotated anticlockwise by 15° and shifted by 3 mm in the x direction. This way, we introduced a combination of "worst-case" errors. These TF maps were then employed for attenuation correction. All images that were corrected with the abovementioned inaccurate attenuation maps were compared to the reference images.

All the above operations were performed for ^{125}I, ^{201}Tl, ^{99m}Tc and ^{111}In separately.

6.3 Results

6.3.1 Phantom experiments

Three 3 mm × 3 mm × 11 mm volumes of interest (VOIs) were defined in heterogeneous slices of each phantom image, as shown in Figure 6.3a. Measured activities within the VOIs in the reference images and in the images corrected with inaccurate attenuation maps were calculated and compared. Changes in the measured VOI activities induced by attenuation map inaccuracies are listed in Table 6.1. With 1 mm shifts of the attenuation maps, the VOI activity changed less than 1.5% for ^{125}I and 0.6% for ^{201}Tl, ^{99m}Tc and ^{111}In. When the shifts increased to 3 mm, the changes increased to less than 4.5% for ^{125}I and 1.7% for ^{201}Tl, ^{99m}Tc and ^{111}In. With 15° rotation of the maps, the changes were less than 1.4% for ^{125}I and 0.9% for ^{201}Tl, ^{99m}Tc and ^{111}In. When the attenuation coefficients were altered by 10%, the activity in the VOIs changed less than 5.2% for ^{125}I and 2.7% for ^{201}Tl, ^{99m}Tc and ^{111}In. With the combination of rotation and shifts of the maps and altered attenuation coefficients, the VOI activity changed less than 6.2% for ^{125}I and 3.0% for ^{201}Tl, ^{99m}Tc and ^{111}In. The quantitative errors of the reference images are listed in the first data column of Table 6.1 for reasons of comparison.

Table 6.1 Quantitative errors and relative changes of VOI activities. Quantitative errors (in %) of VOI activities in reference phantom SPECT images were calculated with respect to dose calibrator measurements (1st data column), and relative changes (in %) in VOI activities due to attenuation map inaccuracies were calculated with respect to reference images (2nd to 9th data column).

Isotope	VOI	Quanti. error	Changes induced by map inaccuracies (rotation, shift and/or μ change) with respect to references							
			0° 1 mm *X* 1.0μ	0° 3 mm *X* 1.0μ	0° 1 mm *Y* 1.0μ	0° 3 mm *Y* 1.0μ	15° 0 mm 1.0μ	0° 0 mm 0.9μ	0° 0 mm 1.1μ	15° 3 mm *X* 1.1μ
^{125}I	1	−20.4	0.1	0.4	−0.5	−4.0	0.0	−4.9	5.2	5.3
	2	−11.8	0.7	1.1	−0.2	−1.0	−0.2	−4.8	5.0	6.2
	3	−7.9	−1.1	−4.0	−1.5	−4.5	−1.4	−4.2	4.3	−0.8
^{201}Tl	1	−5.8	0.0	0.1	−0.1	−1.5	0.0	−2.6	2.7	2.7
	2	6.1	−0.4	−1.4	0.0	−0.3	−0.1	−2.5	2.6	3.0
	3	4.4	0.2	−0.3	0.6	1.4	−0.7	−2.3	2.3	0.0
^{99m}Tc	1	−2.0	0.1	0.2	−0.2	−1.7	0.0	−2.2	2.2	2.1
	2	6.1	−0.3	−1.1	−0.1	−0.3	−0.1	−2.1	2.2	2.4
	3	−8.3	0.4	−0.2	0.5	1.3	−0.2	−1.8	1.9	0.2
^{111}In	1	−4.7	0.0	0.1	−0.2	−1.4	0.0	−2.1	2.1	2.2
	2	−3.5	−0.4	−1.2	0.0	−0.3	−0.1	−2.0	2.0	2.5
	3	3.2	0.0	−1.1	0.4	0.9	−0.9	−1.9	1.9	0.6

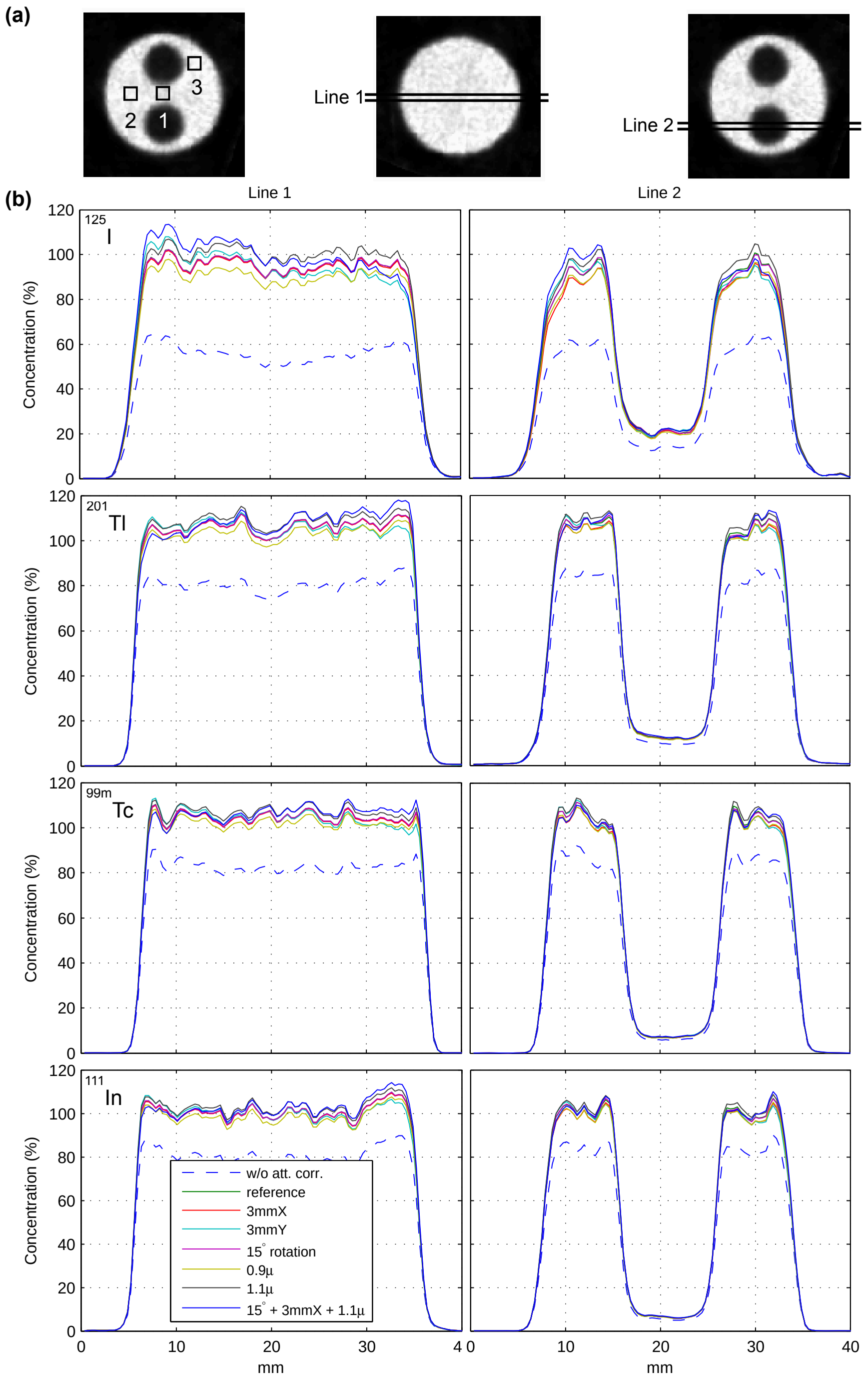

Figure 6.3 VOIs and line profiles. **(a)** VOI and line-profile definitions in phantom images. **(b)** Line profiles in phantom images with different attenuation map inaccuracies for four isotopes.

In addition, the normalized root mean square deviation (NRMSD) was calculated voxel-wise between the reference images and the images corrected with inaccurate attenuation maps:

$$\mathrm{NRMSD} = \sqrt{\frac{1}{n}\sum_{i=1}^{n}\left(\frac{v_i - vr_i}{vr_i}\right)^2} \times 100\% \qquad (6.3),$$

where v_i is i-th voxel inside the phantom chamber in an image corrected with an inaccurate map, and vr_i is the corresponding voxel in a reference image. n is the number of voxels inside the phantom chamber. The results are listed in Table 6.2. The largest NRMSDs caused by combined rotation, shifts and attenuation coefficient errors were 6.3%, 3.0%, 2.5% and 2.3% for ^{125}I, ^{201}Tl, ^{99m}Tc and ^{111}In, respectively.

Table 6.2 NRMSDs (in %) between phantom images corrected with inaccurate maps and with accurate maps.

Isotope	Rotation, shift and × μ							
	0° 1 mm X 1.0μ	0° 3 mm X 1.0μ	0° 1 mm Y 1.0μ	0° 3 mm Y 1.0μ	15° 0 mm 1.0μ	0° 0 mm 0.9μ	0° 0 mm 1.1μ	15° 3 mm X 1.1μ
^{125}I	1.7	4.9	1.7	4.7	0.8	4.4	4.6	6.3
^{201}Tl	0.8	2.2	0.7	2.2	0.4	2.4	2.5	3.0
^{99m}Tc	0.6	1.8	0.6	1.8	0.4	2.1	2.1	2.5
^{111}In	0.6	1.7	0.6	1.6	0.3	1.9	2.0	2.3

Line profiles through homogenous and heterogeneous slices (defined in Figure 6.3a) were created from images corrected with different attenuation maps and are plotted in Figure 6.3b. When the attenuation map was shifted, it is clear that the main changes in quantitation were located at the edges of the phantom along the shifting direction. The changes were small for ^{201}Tl, ^{99m}Tc and ^{111}In imaging (≤5%), while for ^{125}I it was larger (≤10%). Rotation of attenuation maps had almost no effect in homogenous slices for all four isotopes: the line profiles perfectly overlapped the reference profiles. In heterogeneous slices, the profiles slightly deviated (1% to 2%) from the reference profiles only close to the edges of the air chambers. When altering the attenuation coefficients by ±10%, the induced changes were on average about 2% to 3% for ^{201}Tl, ^{99m}Tc and ^{111}In, and about 5% for ^{125}I. Unlike shifting or rotating the maps, the changes in quantitation when the attenuation coefficients were altered resulted in global (but not uniform) over- or underestimations.

6.3.2 Animal experiments

In the rat SPECT images, non-overlapped spherical VOIs (diameter of about 15 mm) were created for each small source. The sources were completely enclosed in the centres of their corresponding VOIs. Activities in the VOIs were measured in the images corrected with different attenuation maps. Comparisons were made between measurements in the

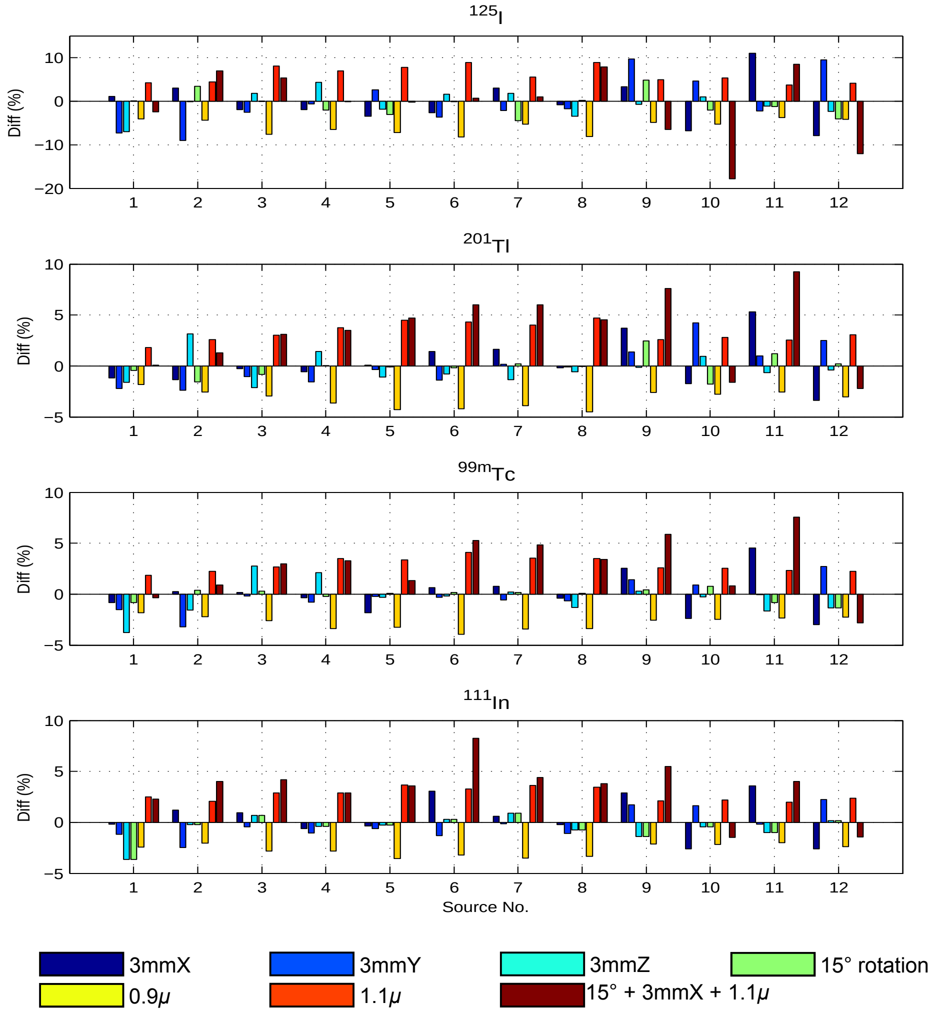

Figure 6.4 Differences between source activities in rat SPECT images corrected with inaccurate attenuation maps and with accurate maps. The differences are in percent (%).

reference images and in the images corrected with inaccurate maps. Changes in the measured VOI activities induced by map inaccuracies are plotted in Figure 6.4, and the average absolute changes in percentage are listed in Table 6.3. With 1 mm shifts of the maps, the measured VOI activities changed 1.4 ± 1.1%, 0.6 ± 0.5%, 0.5 ± 0.4% and 0.5 ± 0.4% on average for ^{125}I, ^{201}Tl, ^{99m}Tc and ^{111}In, respectively, while these average changes increased to 3.6 ± 2.9%, 1.5 ± 1.2%, 1.3 ± 1.2% and 1.2 ± 1.0% with 3 mm shifts. When the maps were rotated by 15°, the changes were 2.1 ± 1.8%, 0.8 ± 0.8%, 0.5 ± 0.4% and 0.5 ± 0.8% on average. When altering the attenuation coefficients by 10%, the VOI activities changed 5.9 ± 1.8%, 3.3 ± 0.9%, 2.8 ± 0.7% and 2.7 ± 0.6% on average for the four isotopes, respectively. With combined rotated and shifted maps and altered attenuation coefficients, the average changes were 5.8 ± 5.4%, 4.4 ± 3.2%, 3.3 ± 2.2% and 3.9 ± 2.2% for ^{125}I, ^{201}Tl, ^{99m}Tc and ^{111}In, respectively. The quantitative errors of the reference images, as described in [204], are listed in the first data column of Table 6.3 for reasons of comparison.

Table 6.3 Average absolute quantitative errors and average absolute changes of source activities. Average absolute quantitative errors (in %) of source activities in reference rat SPECT images were calculated with respect to dose calibrator measurements (1st data column), and average absolute changes (in %) in source activities due to attenuation map inaccuracies were calculated with respect to reference images (2nd to 11th data column).

Isotope	Quanti. error[a]	Changes induced by map inaccuracies (rotation, shift and/or μ change) with respect to references									
		0° 1 mm$X$ 1.0μ	0° 3 mm$X$ 1.0μ	0° 1 mm$Y$ 1.0μ	0° 3 mm$Y$ 1.0μ	0° 1 mm$Z$ 1.0μ	0° 3 mm$Z$ 1.0μ	15° 0 mm 1.0μ	0° 0 mm 0.9μ	0° 0 mm 1.1μ	15° 3 mm$X$ 1.1μ
^{125}I	2.1±6.5	1.5±1.1	3.9±3.1	1.6±1.2	4.6±3.3	0.9±0.9	2.3±1.9	2.1±1.8	5.8±1.7	6.1±1.9	5.8±5.4
^{201}Tl	3.3±2.5	0.6±0.6	1.7±1.6	0.6±0.4	1.5±1.2	0.5±0.5	1.2±0.8	0.8±0.8	3.2±0.8	3.3±0.9	4.4±3.2
^{99m}Tc	2.0±2.5	0.6±0.5	1.5±1.4	0.4±0.4	1.0±1.0	0.5±0.4	1.3±1.2	0.5±0.4	2.8±0.6	2.9±0.7	3.3±2.2
^{111}In	2.0±2.7	0.6±0.4	1.6±1.3	0.4±0.3	1.2±0.8	0.3±0.4	0.8±1.0	0.5±0.8	2.7±0.6	2.8±0.6	3.9±2.2

[a] Obtained from [204].

6.4 Discussion

We previously have shown that quantitative differences between uniform and non-uniform attenuation correction are quite small in micro-SPECT [204]. In this study, the influence of other attenuation map imperfections (i.e. misregistration and global errors in attenuation coefficient) on the quantitative accuracy of attenuation-corrected SPECT was investigated. For this purpose, we mimicked misregistration between micro-SPECT and micro-CT, and global deviation of attenuation coefficients. A mismatch of a few millimetres is already a big error for image registration in small-animal imaging: e.g. Ji et al. [69] showed that when using a proper calibration method for co-registration and a special bed mounting interface, the accuracy of small-animal SPECT–CT registration can reach sub-millimetre accuracy without using extra markers. Deviation of attenuation coefficients can be caused by the errors in CT voxel values (in HU) or from the method that translates HU numbers into linear attenuation coefficients. The system error of CT (in HU) can be eliminated by re-calibration with a water phantom, and other effects such as ring artefacts and beam-hardening effects can be well controlled and suppressed with proper reconstruction algorithms. Many reliable models for translating HU to attenuation coefficients for attenuation correction in SPECT and positron emission tomography have been proposed and evaluated, e.g. in [213, 214]. Therefore, the level of the inaccuracies set in our present investigation is expected to exceed those applied in most real small-animal studies.

For both phantom and animal experiments, the changes in image quantitation due to strong attenuation map inaccuracies were less than about 5%, except for ^{125}I (worst case

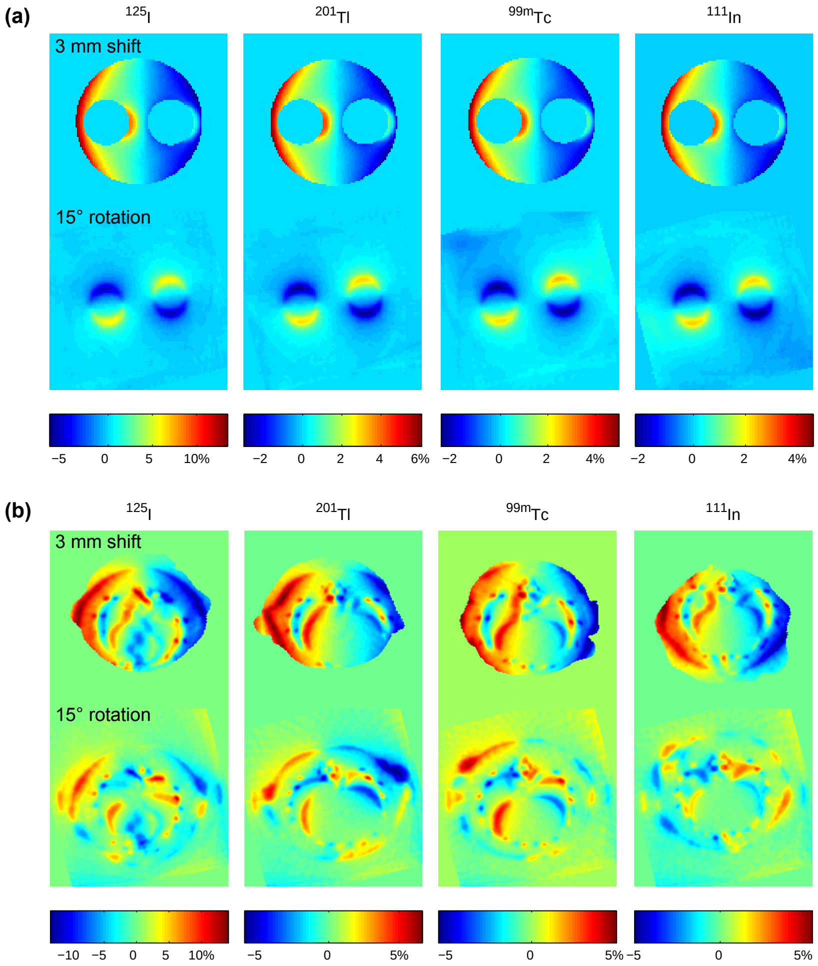

Figure 6.5 Relative differences in attenuation due to 3 mm shifts or 15° rotation. **(a)** Phantom heterogeneous slices and **(b)** rat thoracic slices.

approximately 10%), which can be attributed to ^{125}I attenuation that is more prominent.

In the phantom studies, quantitation changes due to attenuation map shifts were small inside the phantom, but increased close to the outer edge to a maximum of about 5% for ^{125}I and about 2% to 3% for ^{201}Tl, ^{99m}Tc and ^{111}In. Although sharp attenuation and activity changes exist at the edges of the air chambers in the phantom, the changes in TF maps are rather smooth. As a result, quantification errors due to misregistration stayed also small in these regions. Quantitation changes caused by map rotation were smaller than the changes by shifts, and because the axis of rotation was closely aligned with the axis of the phantom, the changes only existed close to the air chambers. This may be relevant for quantification in e.g. tumours that are close to lungs or in cardiac imaging. These changes of measured activity concentration were consistent with the relative differences between the

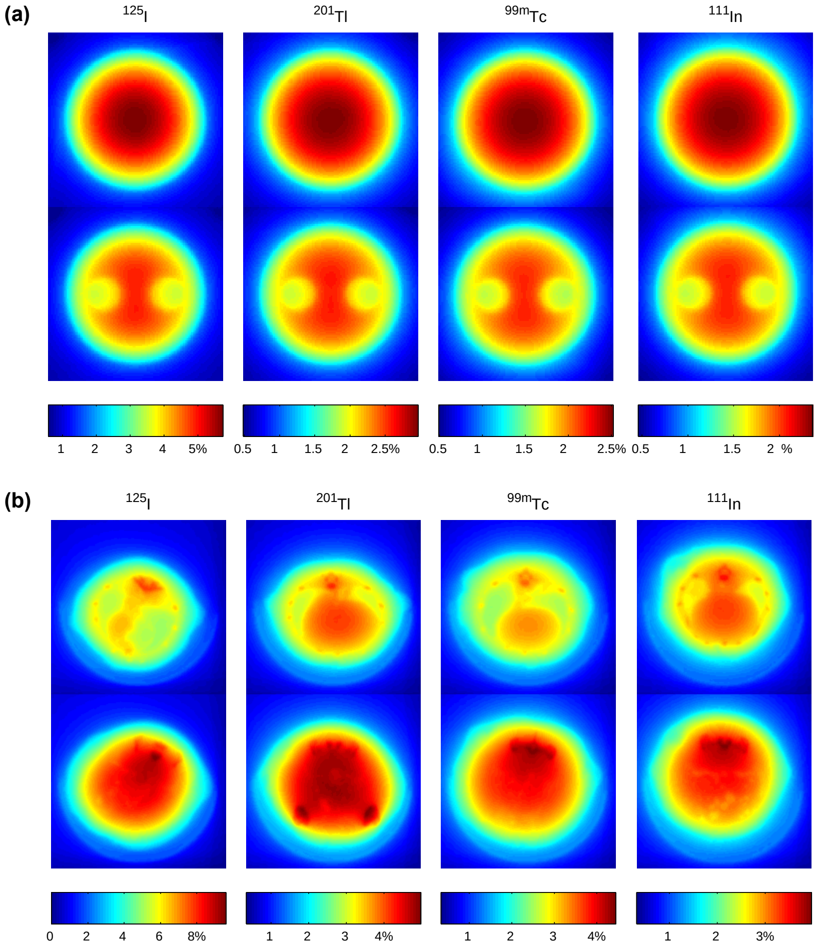

Figure 6.6 Relative differences in attenuation due to multiplying attenuation coefficients by 1.1. **(a)** Two different phantom slices and **(b)** two different slices through each rat.

reference TF maps and the shifted or rotated maps, as shown in Figure 6.5a. When imaging the small sources in the rat cadavers, the activity changes in a subset of sources due to shifts and rotation were a bit larger than changes in the phantom, which can be explained by the effects of non-uniform attenuation close to the sources. Again, the influence of rotation on map accuracy was smaller than that of shifts, as shown in the rat thoracic slices in Figure 6.5b. Since both large shifts and rotation have limited effects on quantitative accuracy in our emulation, we believe that the typical misalignments between micro-SPECT and micro-CT caused by sub-optimal registration and/or animal movement during scans will not often have a prominent impact to SPECT quantitative accuracy.

With attenuation coefficients globally altered by ±10%, similar global over- or underestimation was observed in both phantom and animal studies. We also examined the relative differences between the reference TF maps and the ones derived from 10% increased attenuation coefficients. Figure 6.6a shows the differences in two transaxial slices of phantom TF maps for each isotope. One slice was from the part of the phantom without air chambers, and the other one was from the part that contains the two air chambers. Figure 6.6b shows the differences in two slices through the rat TF maps: one slice across the thorax and the other across the abdomen of each rat. It is clear that with a global change of the attenuation coefficients, the changes in the TF maps are not homogenous. The effects are larger around bone areas as shown in Figure 6.6b and are smaller at areas with low density such as the air chambers in Figure 6.6a and lungs in Figure 6.6b. Ostensibly, this implies that the attenuation coefficient accuracy in and around the bones may play a relatively important role in the accuracy of SPECT attenuation correction. However, the contribution of bone attenuation is limited in the integral in Equation (6.1) for small animals so that effects on quantification would not spread widely, as shown in the “Results” section and in Figure 6.6b.

Without attenuation correction, activities were roughly underestimated by 40% for ^{125}I and 20% for ^{201}Tl, ^{99m}Tc and ^{111}In. Even the largest inaccuracies in attenuation maps investigated here effectively took away only one eighth of the benefit from the attenuation correction. Since accuracy of the attenuation coefficients and alignment between micro-SPECT and micro-CT in practice are usually better than in the worst situations emulated in the present study, effects of attenuation map inaccuracies on micro-SPECT quantification will usually be small.

6.5 Conclusions

For the more commonly used SPECT isotopes like ^{201}Tl, ^{99m}Tc and ^{111}In, misalignments up to a few millimetres or in the order of 10° to 15° between micro-SPECT and micro-CT, and/or global attenuation coefficient inaccuracies in the range of ±10% have quite small effects on micro-SPECT quantification. Therefore, we conclude that micro-SPECT quantification is quite robust to imperfections in attenuation maps for most applications.

Acknowledgments

This research was partly performed within the framework of CTMM, the Center for Translational Molecular Medicine (www.ctmm.nl), project EMINENCE (grant 01C-204). We are grateful to Bianca Lemmers-de Weem (Central Animal Facility, Radboud University Nijmegen, Nijmegen, the Netherlands) for technical assistance and Pieter E. B. Vaissier (Section Radiation, Detection & Medical Imaging, Delft University of Technology, Delft, the Netherlands) for suggestions and comments on the manuscript.

Chapter VII

Summary and future prospects

The main content of this thesis comprises two aspects regarding high-resolution small-animal single-photon emission computed tomography (SPECT) and SPECT/computed tomography (CT): (i) application in cardiac studies and its relevant technical issues, and (ii) SPECT image quantification.

Preclinical cardiovascular research using small-animal models has been extensively developed in recent years. **Chapter II** provides a brief explanation of the basics of micro-SPECT with (multi-) pinholes. Different system designs are introduced, including rotation-based and stationary devices. Stationary systems such as U-SPECT have the advantage of good temporal resolution for gated or dynamic studies. In addition, Chapter II introduces the combination of micro-SPECT and micro-CT, in which CT images can be used to supply anatomic information for locating the SPECT tracer, or to create attenuation maps for attenuation correction of SPECT images. Two types of combination, i.e. a click-over mode and an integrated mode, together with their realization in a few prototype and commercial systems known at the time are discussed and compared. The second half of Chapter II elaborates on applications in cardiovascular research that can be done with micro-SPECT or micro-SPECT/CT systems. These studies mainly benefit from the high spatial resolution of micro-SPECT systems and pharmacological research for novel radiolabelled molecules. Some applications, such as left ventricular function assessment, also benefit from high temporal resolution of micro-SPECT and ECG-gating techniques. A few CT applications are also included, such as investigation into vascular dynamics and calcification.

ECG gating is a technique that eliminates blurring of the SPECT images due to the motion of the heart, which is essential for left ventricular functional studies. Besides this, the quality and quantitation of heart images may also be influenced by respiration. Therefore, it raises the question that if simultaneous ECG and respiratory gating can further improve myocardial research. In the study of **Chapter III**, myocardial perfusion images of mice were acquired and reconstructed with ECG gating only or with both ECG- and respiratory-gating information. In addition, because animal positioning may affect blood flow and freedom of heart motion, we acquired those images by laying mice in supine and prone positions. Reconstructed images are blurred with different sized Gaussian kernels before analysing them in software packages dedicated for myocardial function assessment. Cardiac parameters such as left ventricular volumes and ejection fractions were obtained and compared for the different gating strategies, image filtering and animal positions. The results show that in general, the influence of respiratory gating and image filtering seems to be limited, while animal positioning affected these parameters for some mice. It means that respiratory gating is probably not necessary in most mouse cardiac studies even with sub-half-millimetre-resolution SPECT, which can save a lot of labour and time in performing acquisition and reconstruction.

Due to the small dimensions of rodents, attenuation is not a big effect in micro-SPECT, especially when imaging mice. With simple scatter correction methods for artefact removal, micro-SPECT images are usually considered sufficient for qualitative and semi-quantitative research. However sometimes, absolute quantification is definitely required, such as in diagnosis of triple vessel disease or in pharmacokinetic investigations. Besides scatter correction, image calibration and attenuation correction are key steps towards absolute quantitative SPECT. These have been thoroughly discussed in Chapter IV and V. **Chapter IV** describes a complete workflow of SPECT image quantification, including calibration (with a point source), scatter correction (energy-window method integrated with image reconstruction) and attenuation correction. An optical-contour-based Chang algorithm modified for multi-pinhole SPECT were proposed for uniform attenuation correction. In this method, the vertical and horizontal animal contours obtained from optical cameras were employed for creating 3D surfaces of the animals approximately. Within the 3D contour, a uniform attenuation coefficient that is associated with water and SPECT photon energy was assigned. The overall transmitted fraction (TF) of each voxel was calculated as an average of TFs along different projection paths. For ^{99m}Tc this technique improved SPECT quantification from having about 20% error to about 2% error on average in both a uniform phantom study and a rat study.

More accurate non-uniform attenuation correction can be achieved with the help of registered micro-CT images. In **Chapter V**, we evaluated a CT-based non-uniform Chang algorithm with more isotopes (i.e. ^{125}I, ^{201}Tl, ^{99m}Tc and ^{111}In). The experiments were performed using a U-SPECT-II/CT system, which followed the same steps as in the studies of Chapter IV, only with the uniform phantom replaced by a small-animal NEMA image quality phantom. Attenuation in SPECT images was corrected by using uniform Chang method based on optical contours and based on CT contours, and non-uniform Chang method based on CT images. Together with SPECT calibration and energy-window-based scatter correction, all the three attenuation correction methods lead to high quantitative accuracy for all the four isotopes (e.g. 2.1%, 3.3%, 2.0% and 2.0% on average in rat studies with non-uniform correction for ^{125}I, ^{201}Tl, ^{99m}Tc and ^{111}In, respectively), and the non-uniform Chang method shows superior accuracy except for ^{125}I images. We found that other factors such as accuracy of SPECT system modelling and scatter correction have more impact on the final quantitative accuracy than the selected attenuation correction methods.

When attempting to benefit from CT-based non-uniform attenuation correction, one should be aware of the accuracy of attenuation maps derived from CT images. The errors in the maps will certainly affect the attenuation correction and subsequently the quantitative accuracy of SPECT images, but the question is how big the effect is. **Chapter VI** provides a detailed discussion on this topic. We re-analysed the data set in Chapter V and introduced artificial errors in the attenuation maps. Two types of errors were emulated, i.e. misalignment between CT maps and SPECT images, by shifting the attenuation maps by up to 3 mm in different directions and rotating them by 15°; and deviations in attenuation coefficients, by altering the attenuation coefficients by ±10%. Absolute quantitative accuracy of SPECT images corrected with these suboptimal attenuation maps was examined. Unlike the general understanding in clinical SPECT, the errors we introduced in attenuation maps cause only small changes in quantitative accuracy. For instance, the changes in measured activities of ^{201}Tl, ^{99m}Tc and ^{111}In in the NEMA phantom were less than 1.7% by 3 mm shifting of attenuation maps, and less than 2.7% by ±10% altering of attenuation coefficients. Because the accuracy of attenuation maps in real studies is usually better than in the worst situations we emulated, we conclude that quantification of micro-SPECT images is quite robust to imperfections of attenuation maps. Therefore, the CT-based non-uniform Chang attenuation correction method is valuable and practical in micro-SPECT/CT.

Quantitative accuracy of PET is usually thought to be much better than that of SPECT, because of the problems with correcting for attenuation in clinical SPECT. In the past this was certainly the case, but today clinical SPECT has improved dramatically due to the use of accurate integrated hardware for obtaining attenuation maps and the use of accurate methods for corrections of distance-dependent detector blurring, scatter and attenuation effects. Therefore, SPECT images acquired with modern systems can have very good quantitative accuracy. In this thesis, we show that small-animal SPECT can also yield highly quantitative images, which makes it an excellent tool for preclinical studies. Moreover, Vaissier et al. have recently shown that SPECT can be used for fast dynamic scans [215]. Today mouse images can be acquired within from 1 second (organ) to 20 seconds (total body) with the U-SPECT^{+} system. This for instance, opens up the possibility for modelling and assessment of pharmaceutical kinetics that was only the domain of PET studies: in such studies, highly accurate quantification of activity concentration in tissues is required especially when blood/plasma samples are used for creating input functions. Many PET studies could be translated to the SPECT platform, and benefit from the sub-half-millimetre resolution of micro-SPECT and a wide range of available SPECT isotopes. SPECT has also the capability of performing multi-isotope studies—imaging two or more different tracers simultaneously, including PET tracers. All these possibilities show us promising prospects, but also raise challenges to further improvement and development of quantitative micro-SPECT.

Firstly, when imaging multiple isotopes simultaneously, scatter of high-energy photons emitted from one isotope can affect image noise level and quantification of images of other isotopes that emit lower-energy photons. Moreover, crosstalk between photopeaks can affect image noise level and quantitation for both isotopes. The energy-window-based scatter and background correction method may still be useful in such cases, but the optimal window settings for different combinations of isotopes still need to be investigated, especially when crosstalk of photopeaks exists.

Secondly, the capabilities of U-SPECT have recently been expanded to also image PET tracers simultaneously with SPECT tracers at sub-millimetre resolution level [34]. This device with the name VECTor uses dedicated pinhole technology to provide higher resolution PET images than that acquired with traditional coincidence PET. However, the

511 keV photons produced by electron–positron annihilation are difficult to collimate and shield compared to photons emitted by common SPECT isotopes. Novel designs such as pinhole clusters in the collimator and spiral bed-trajectories with scanning focus method, as well as better modelling of the system response including photon penetration of the collimator, have been implemented or are under thorough investigation and development in order to achieve better PET image quality and quantification. It would be an interesting topic to extend our research on scatter and attenuation correction to this pinhole PET system, which will be very useful and practical for preclinical PET and hybrid SPECT/PET studies in the future.

Thirdly, as we can see in the previous chapters, the quantification of ^{125}I is still not optimized. ^{125}I mainly produces gamma photons and X rays between 27 and 35 keV, which are close to the low end of the energy range used in preclinical SPECT applications. Therefore, the attenuation of ^{125}I photons is much stronger than that of other common SPECT isotopes. Moreover, the probability of coherent scattering is higher for ^{125}I, which is around 20% of the total scattering, while for ^{99m}Tc this proportion is only about 2%. Since the coherent scattering can hardly be corrected by using energy-window-based method, if we want to improve the quantitative accuracy of ^{125}I images, we should either improve the scatter correction of ^{125}I imaging especially for the coherent scattering, or take the coherent scattering into account in the attenuation correction with an overall compensation approach.

Finally yet importantly, the CT calibration as a step in SPECT quantification could be improved and automated. In order to convert a CT image into an attenuation map, the arbitrary units of CT voxel values should firstly be translated into physical units, such as the Hounsfield units, by using CT calibration factors. Traditionally the calibration factors are obtained by scanning known-density phantoms. However, phantom variables and non-uniform artefacts in phantom images are responsible for a measurable degradation in accuracy of CT calibration, and changes in X-ray tube settings may invalidate the calibration factors measured with another setting. Therefore, we are currently investigating to design and evaluate CT self-calibration methods, which only use the statistical information of the CT images themselves [216]. We hope that our future research and investigation could help with the improvement of quantitative small-animal SPECT/PET/CT.

Chapter VIII

Samenvatting en toekomstige ontwikkelingen

Dutch translation: Frans van der Have

De hoofdinhoud van dit proefschrift omvat twee aspecten die betrekking hebben op Single Photon Emission Computed Tomography (SPECT) en SPECT/Computed Tomography (CT) op kleine dieren met een hoge resolutie: (i) de toepassing van deze technieken in hartstudies en de daarbij behorende technische aspecten, en (ii) de kwantificatie van SPECT beelden.

Preklinisch cardiovasculair onderzoek door middel van modellen in kleine dieren heeft de laatste jaren een uitgebreide ontwikkeling doorgemaakt. **Hoofdstuk II** geeft een korte uitleg over de grondbeginselen van micro-SPECT met (meerdere) pinholes. Verschillende ontwerpen van systemen worden beschreven, waaronder die op rotatie gebaseerd zijn alsmede stationaire systemen. Stationaire systemen zoals de U-SPECT hebben als voordeel een goede tijdsresolutie voor gated of dynamische studies. Verder introduceert hoofdstuk II de combinatie van micro-SPECT en micro-CT, waarbij CT beelden kunnen worden gebruikt om anatomische informatie te verschaffen met het oog op het lokaliseren van de SPECT zoekstof of als verzwakkingsbeelden ten behoeve van verzwakkingscorrectie van de SPECT beelden. Twee mogelijke typen van deze combinatie, dat wil zeggen een click-over modus en een geïntegreerde modus worden behandeld en met elkaar vergeleken, samen met hun realisatie in enkele prototype en commercieel verkrijgbare systemen die in die tijd bekend waren. De tweede helft van Hoofdstuk II gaat dieper in op de toepassingen in cardiovasculair onderzoek dat gedaan kan worden met micro-SPECT of micro-SPECT/CT systemen. Deze studies hebben met name baat bij de hoge ruimtelijke resolutie van micro-SPECT systemen en bij farmacologisch onderzoek naar nieuwe radioactief gemerkte moleculen. Sommige toepassingen, zoals onderzoek naar de functie van de linker ventrikel, hebben bovendien baat bij een hoge resolutie van de micro-SPECT en bij de techniek van gating op het elektrocardiogram (ECG). Enkele CT toepassingen zijn ook opgenomen, zoals het onderzoek naar vaatdynamiek en calcificaties.

ECG gating is een techniek die de onscherpte ten gevolge van de beweging van het hart uit de SPECT beelden verwijdert, hetgeen essentieel is bij studies naar de functie van de linker ventrikel. Daarnaast kunnen de beeldkwaliteit en getalsmatige waarden van hartbeelden ook beïnvloed worden door de ademhaling. Daarom wordt de vraag opgeroepen of simultane gating van zowel ECG als ademhaling het hartspieronderzoek nog verder kan verbeteren. In de studie van **Hoofdstuk III** werden hartspierperfusiebeelden van muizen geacquireerd en gereconstrueerd, met slechts ECG gating en met zowel ECG als ademhalings gating informatie. Bovendien, omdat de positionering van het dier de bloedsomloop en de mogelijkheden voor het hart om te bewegen kan beïnvloeden, hebben we die beelden met de muis zowel liggend op de rug als liggend op de buik geacquireerd. De gereconstrueerde beelden worden gefilterd met Gaussische kernels van verschillende groottes voordat ze worden geanalyseerd in een gespecialiseerd software-pakket voor het beoordelen van hartspierfunctie. Aan het hart gerelateerde maten zoals volume van het linker ventrikel en ejectiefractie werden bepaald en met betrekking tot de verschillende wijzen van gating, mate van filteren en de verschillende posities van het dier met elkaar vergeleken. De resultaten laten zien dat in het algemeen het effect van ademhalingsgating en het filteren van het beeld beperkt lijken, terwijl de positionering van het dier deze maten voor sommige muizen wel beïnvloedt. Dit betekent dat ademhalingsgating waarschijnlijk niet nodig is in veel hartstudies in de muis, zelfs niet met SPECT met een sub-millimeter resolutie, hetgeen veel werk en tijd kan besparen bij het uitvoeren van de acquisitie en de reconstructie.

Vanwege de kleine afmetingen van knaagdieren speelt verzwakking geen grote rol in micro-SPECT, zeker niet als er muizen afgebeeld worden. Met eenvoudige correctiemethoden voor verstrooiing die artefacten verwijderen, zijn micro-SPECT beelden meestal goed genoeg voor kwalitatief en semi-kwantitatief onderzoek. Echter, soms is absolute kwantificatie zeker benodigd, zoals bij de diagnose van ernstige vernauwingen in de kransslagader of in farmacokinetische onderzoeken. Naast de correctie voor strooistraling zijn calibratie van beeldwaarden en verzwakkingscorrectie belangrijke stappen richting kwantitatieve SPECT. Deze dingen zijn grondig besproken in Hoofdstuk IV en V. **Hoofdstuk IV** beschrijft het totale proces van SPECT beeldkwantificatie, onder andere calibratie (met een puntbron), correctie voor strooistraling (een methode op basis van energie-windows die geïntegreerd is in de beeldreconstructie) en verzwakkingscorrectie. Een Chang algoritme dat is gebaseerd op optische contouren en aangepast voor SPECT met multi-pinholes werd voorgesteld voor uniforme verzwakkingscorrectie. In deze methode werden de verticale en horizontale contouren van het dier, verkregen uit optische camera's, gebruikt om 3D oppervlakken van de dieren bij benadering te genereren. Binnen de 3D contour wordt een uniforme verzwakkingscoëfficiënt toegekend die hoort bij water en de desbetreffende SPECT fotonenergie. De uiteindelijke transmissie fractie (TF) van elk voxel werd berekend als zijnde het gemiddelde van verschillende TF's langs verschillende projectierichtingen. Voor ^{99m}Tc zorgde deze techniek voor een verbetering in SPECT kwantificatie van een gemiddelde fout van ongeveer 20% naar ongeveer2%, zowel in een studie met een uniform gevuld fantoom als in een ratstudie.

Nog nauwkeuriger niet-uniforme verzwakkingscorrectie kan worden bereikt met behulp van geregistreerde micro-CT beelden. In **Hoofdstuk V** hebben we een op CT gebaseerd Chang algoritme geëvalueerd met verscheidene isotopen (d.w.z. ^{125}I, ^{201}Tl, ^{99m}Tc en ^{111}In). De experimenten werden gedaan op een U-SPECT-II/CT systeem, volgens dezelfde stappen als hoofdstuk IV, waarbij alleen het uniforme fantoom vervangen wordt door een kleine-dieren NEMA beeldkwaliteitsfantoom. De verzwakking in de SPECT beelden werd gecorrigeerd door de uniforme Chang methode te gebruiken die gebaseerd is op optische contouren, vervolgens een uniforme Chang methode gebaseerd op CT-contouren en als derde een niet-uniforme Chang methode gebaseerd op CT-contouren. Samen met SPECT calibratie en op energie-windows gebaseerde strooistralingscorrectie, bereiken alle drie de verzwakkingscorrectie methoden een hoge kwantitatieve nauwkeurigheid voor alle vier isotopen (bijvoorbeeld gemiddeld 2,1%, 3,3%, 2,0% en 2,0% in rat studies met niet-uniforme correctie voor respectievelijk ^{125}I, ^{201}Tl, ^{99m}Tc en ^{111}In) en de niet-uniforme Chang methode is nauwkeuriger behalve voor de ^{125}I beelden. We hebben gevonden dat andere factoren zoals de nauwkeurigheid van de SPECT modellering en strooistralingscorrectie een grotere invloed hebben o de uiteindelijke kwantitatieve nauwkeurigheid dan de keuze voor de methode van verzwakkingscorrectie.

Als men probeert profijt te halen uit op CT gebaseerde niet-uniforme verzwakkingscorrectie, moet men zich bewust zijn van de betrouwbaarheid van verzwakkingskaarten die afgeleid zijn van CT-beelden. De fouten in die kaarten zullen zeker de verzwakkingscorrectie en daaropvolgend de kwantitatieve nauwkeurigheid van de SPECT beelden beïnvloeden, maar de vraag is hoe groot die invloed is. **Hoofdstuk VI** geeft een gedetailleerde beschrijving van dit onderwerp. We hebben de gegevens uit Hoofdstuk V opnieuw geanalyseerd en kunstmatige fouten in de verzwakkingskaarten gestopt. Twee typen fouten werden nagebootst, namelijk een verkeerde uitlijning tussen de CT- en SPECT-beelden, door de verzwakkingskaarten over een afstand tot 3 mm te verschuiven in verschillende richtingen en ze over 15° te roteren; en afwijkingen in verzwakkingscoëfficiënten, door de verzwakkingscoëfficiënten met ±10% te veranderen. De absolute kwantitatieve nauwkeurigheid van SPECT beelden die met deze suboptimale verzwakkingskaarten waren gecorrigeerd, werd onderzocht. Anders dan wat er algemeen wordt aangenomen in klinische SPECT, veroorzaken de fouten die wij in de verzwakkingskaarten hebben geïntroduceerd, slechts kleine veranderingen in kwantitatieve nauwkeurigheid. Zo waren de veranderingen in de gemeten activiteiten van ^{201}Tl, ^{99m}Tc en ^{111}In in het NEMA fantoom bijvoorbeeld minder dan 1,7% bij een verschuiving van 3 mm van de verzwakkingskaart en minder dan 2.7% bij een ±10% verandering van de verzwakkingscoëfficiënten. Omdat de nauwkeurigheid van de verzwakkingskaarten in echte studies vaak beter is dan in deze slechtste gevallen waar we vanuit gegaan zijn, concluderen we dat de kwantificatie van micro-SPECT beelden in redelijk grote mate robuust is tegen onvolmaaktheden in verzwakkingskaarten. Daarom is de niet-uniforme op CT gebaseerde Chang verzwakkingscorrectie methode waardevol en praktisch toepasbaar in micro-SPECT/CT.

De kwantitatieve nauwkeurigheid van PET wordt algemeen aangenomen aanzienlijk beter te zijn dan die van SPECT, vanwege de problemen die er zijn bij het corrigeren van verzwakking in klinische SPECT. In het verleden was dit zeker het geval, maar vandaag de dag is klinische SPECT enorm verbeterd dankzij het gebruik van nauwkeurige geïntegreerde hardware voor het verkrijgen van verzwakkingskaarten en het gebruik van nauwkeurige methoden voor het corrigeren van de effecten van afstandsafhankelijke detectoronscherpte, strooistraling en verzwakking. Daarom kunnen SPECT beelden die met moderne systemen zijn opgenomen een zeer goede kwantitatieve nauwkeurigheid hebben. In dit proefschrift laten we zien dat ook kleine-dieren SPECT in hoge mate kwantitatieve beelden kan opleveren, hetgeen dit tot een uitmuntend stuk gereedschap maakt voor preklinische studies. Bovendien hebben Vaissier et al onlangs laten zien dat SPECT gebruikt kan worden voor snelle dynamische opnames [215]. Vandaag kunnen beelden van de muis worden geacquireerd binnen een tijd vanaf 1 seconde (orgaan) tot 20 seconden (gehele lichaam) met het U-SPECT^{+}-systeem. Dit maakt bijvoorbeeld het modelleren en bepalen van farmaceutische kinetiek mogelijk, hetgeen voorheen uitsluitend het domein van PET studies was: in zulke studies is een hoge mate van nauwkeurigheid vereist in de kwantificatie van activiteitsconcentraties in weefsels, in het bijzonder wanneer bloed/plasma monsters gebruikt worden voor het maken van de ingangsfuncties. Veel PET studies zouden naar het SPECT platform kunnen worden overgezet en daarmee profiteren van de resolutie van micro-SPECT die minder dan een halve millimeter bedraagt en daarnaast van het grote aantal beschikbare SPECT isotopen. SPECT heeft daarnaast ook de mogelijkheid dat er multi-isotoop-studies gedaan worden: het tegelijkertijd afbeelden van twee of meer zoekstoffen, inclusief PET zoekstoffen. Al deze mogelijkheden tonen ons veelbelovende vooruitzichten, maar roepen ook uitdagingen op voor de verdere verbetering en ontwikkeling van kwantitatieve micro-SPECT.

Ten eerste, wanneer meerdere isotopen tegelijkertijd worden afgebeeld, kan de strooistraling van fotonen met een hoge energie die worden uitgezonden door de ene isotoop het ruisniveau en de beeldkwantificatie van andere isotopen die een fotonen met een lagere energie uitzenden, beïnvloeden. Bovendien kan overspraak tussen de fotopieken het ruisniveau van het beeld en de kwantificatie voor beide isotopen beïnvloeden. De op energie windows gebaseerde methode voor het corrigeren van strooistraling en achtergrond kan in zulke gevallen nog steeds nuttig kunnen zijn, maar de optimale window instellingen voor verschillende combinaties van isotopen moeten nog onderzocht worden, in het bijzonder als er overspraak tussen fotopieken voorkomt.

Ten tweede kan de U-SPECT sinds kort ook PET zoekstoffen tegelijkertijd met SPECT zoekstoffen afbeelden met een resolutieniveau beneden een millimeter [34]. Dit instrument, VECTor genaamd, gebruikt speciaal voor dit doel ontwikkelde pinhole technologie om PET beelden met een hogere resolutie beschikbaar te maken dan de beelden die gemeten worden met traditionele PET die op coïncidentie gebaseerd is. Echter, de fotonen met een energie van 511 keV die gevormd worden door elektron-positron annihilatie, zijn moeilijk te collimeren en af te schermen vergeleken met de fotonen die door de veelgebruikte SPECT isotopen worden uitgezonden. Nieuwe ontwerpen zoals clusters van pinholes in de collimator en spiraalvormige beweging van het bed met een scanning focus methode en ook betere modellering van de systeemrespons die ook de fotondoorslag door de collimator omvat, zijn geïmplemeteerd of worden nu grondig onderzocht en ontwikkeld, opdat betere PET beeldkwaliteit en kwantificatie bereikt worden. Het zou een interessant onderwerp zijn om ons onderzoek uit te breiden naar correctie van strooistraling en verzwakking bij dit pinhole PET systeem, hetgeen erg bruikbaar en praktisch zal zijn voor preklinische PET en gemengde SPECT/PET studies in de toekomst.

Ten derde, zoals we kunnen zien in de voorgaande hoofdstukken, is de kwantificatie van ^{125}I nog niet geoptimaliseerd. ^{125}I produceert voornamelijk gamma- en röntgenfotonen met een energie tussen 27 en 35 keV; dat is dichtbij de laagste energie in het energiebereik dat in preklinische SPECT toepassingen gebruikt wordt. Daarom is de verzwakking van ^{125}I fotonen veel sterker dan die van andere veel voorkomende SPECT isotopen. Bovendien is de kans op coherente verstrooiing hoger voor ^{125}I, hetgeen ongeveer 20% van de totale verstrooiing is, terwijl dit voor ^{99m}Tc slechts 2% is. Omdat coherente verstrooiing nauwelijks gecorrigeerd kan worden door gebruik te maken van de op energie windows gebaseerde methode, moeten we, als we de kwantitatieve nauwkeurigheid van ^{125}I beelden willen verbeteren, ofwel de strooistralingscorrectie voor ^{125}I beeldvorming specifiek verbeteren voor coherente verstrooiing, ofwel de coherente verstrooiing meenemen in de verzwakkingscorrectie met een aanpak die alles compenseert.

Als laatste maar ook belangrijke punt, zou de CT kalibratie als een stap in de SPECT kwantificatie kunnen worden verbeterd en geautomatiseerd. Om een CT-beeld om te zetten in een verzwakkingskaart, zouden de willekeurige eenheden van de CT-voxelwaarden eerst moeten worden vertaald naar fysische eenheden, zoals Hounsfield eenheden, door middel van CT kalibratiefactoren. Traditioneel worden de kalibratiefactoren verkregen door fantomen met een bekende dichtheid te meten. Echter, fantoomveranderlijken en niet-uniforme artefacten in de fantoombeelden zijn verantwoordelijk voor een meetbare achteruitgang in nauwkeurigheid van de CT kalibratie; en veranderingen in de instellingen van de röntgenbuis kunnen de kalibratiefactoren die bij een andere instelling gemeten zijn, ongeldig maken. Daarom doen we nu onderzoek naar het ontwerp en de evaluatie van zelf-kalibratie methoden voor CT, die slechts gebruik maken van de statistische informatie vervat in de CT beelden zelf [216]. We hopen dat ons toekomstig onderzoek zou kunnen helpen bij het verbeteren van kwantitatieve SPECT/PET/CT voor kleine dieren.

References

[1] Massoud TF, Gambhir SS. Molecular imaging in living subjects: seeing fundamental biological processes in a new light. *Genes Dev*. 2003;17(5):545–80.

[2] Pysz MA, Gambhir SS, Willmann JK. Molecular imaging: current status and emerging strategies. *Clin Radiol*. 2010;65(7):500–16.

[3] Choy G, Choyke P, Libutti SK. Current advances in molecular imaging: noninvasive in vivo bioluminescent and fluorescent optical imaging in cancer research. *Mol Imaging*. 2003;2(4):303–12.

[4] Meikle SR, Kench P, Kassiou M, Banati RB. Small animal SPECT and its place in the matrix of molecular imaging technologies. *Phys Med Biol*. 2005;50(22):R45–61.

[5] Miao Y, Benwell K, Quinn TP. ^{99m}Tc- and ^{111}In-Labeled α-melanocyte-stimulating hormone peptides as imaging probes for primary and pulmonary metastatic melanoma detection. *J Nucl Med*. 2007;48(1):73–80.

[6] de Visser M, Bernard HF, Erion JL, Schmidt MA, Srinivasan A, Waser B et al. Novel ^{111}In-labelled bombesin analogues for molecular imaging of prostate tumours. *Eur J Nucl Med Mol Imaging*. 2007;34(8):1228–38.

[7] Zhang J, Nie L, Razavian M, Ahmed M, Dobrucki LW, Asadi A et al. Molecular imaging of activated matrix metalloproteinases in vascular remodeling. *Circulation*. 2008;118(19):1953–60.

[8] Habraken JB, de Bruin K, Shehata M, Booij J, Bennink R, van Eck Smit BL et al. Evaluation of high-resolution pinhole SPECT using a small rotating animal. *J Nucl Med*. 2001;42(12):1863–9.

[9] Wu MC, Hasegawa BH, Dae MW. Performance evaluation of a pinhole SPECT system for myocardial perfusion imaging of mice. *Med Phys*. 2002;29(12):2830–9.

[10] Schramm NU, Ebel G, Engeland U, Schurrat T, Behe M, Behr TM. High-resolution SPECT using multipinhole collimation. *IEEE Trans Nucl Sci*. 2003;50(3):315–20.

[11] Forrer F, Bernard B, Schramm NU, Hoppin JW, Lackas C, Valkema R et al. High sensitivity multi-pinhole animal-SPECT/CT with submillimetre resolution allows absolute in vivo quantification. *Eur J Nucl Med Mol Imaging*. 2006;33:S315.

[12] Funk T, Despres P, Barber WC, Shah KS, Hasegawa BH. A multipinhole small animal SPECT system with submillimeter spatial resolution. *Med Phys*. 2006;33(5):1259–68.

[13] Beekman F, van der Have F. The pinhole: gateway to ultra-high-resolution three-dimensional radionuclide imaging. *Eur J Nucl Med Mol Imaging*. 2007;34(2):151–61.

[14] Needham J. Science and civilization in China. Taipei: Caves Books Ltd.; 1986.

[15] O’Connor JJ, Robertson EF. Light through the ages: Ancient Greece to Maxwell. 2002. http://www-history.mcs.st-andrews.ac.uk/HistTopics/Light_1.html. Accessed 13 Jan 2013.

[16] Vallely P. How Islamic inventors changed the world. *The Independent*. 2006. http://www.independent.co.uk/news/science/how-islamic-inventors-changed-the-world-469452.html. Accessed 14 Jan 2013.

[17] Lindberg DC. A reconsideration of Roger Bacon’s theory of pinhole images. *Arch Hist Exact Sci*. 1970;6:214–23.

[18] Bellis M. History of photography—Pinhole cameras to the daguerreotype. http://inventors.about.com/od/pstartinventions/a/stilphotography.htm. Accessed 14 Jan 2013.

[19] O’Connor JJ, Robertson EF. Giambattista della Porta. 2010. http://www-history.mcs.st-andrews.ac.uk/Biographies/Porta.html. Accessed 14 Jan 2013.

[20] Grepstad J. Pinhole photography. 2003. http://photo.net/learn/pinhole/pinhole. Accessed 14 Jan 2013.

[21] McElroy DP, MacDonald LR, Beekman FJ, Wang YC, Patt BE, Iwanczyk JS et al. Performance evaluation of A-SPECT: A high resolution desktop pinhole SPECT system for imaging small animals. *IEEE Trans Nucl Sci*. 2002;49(5):2139–47.

[22] Furenlid LR, Wilson DW, Chen YC, Kim H, Pietraski PJ, Crawford MJ et al. FastSPECT II: A second-generation high-resolution dynamic SPECT imager. *IEEE Trans Nucl Sci*. 2004;51(3):631–5.

[23] Beekman FJ, van der Have F, Vastenhouw B, van der Linden AJA, van Rijk PP, Burbach JPH et al. U-SPECT-I: A novel system for submillimeter-resolution tomography with radiolabeled molecules in mice. *J Nucl Med*. 2005;46(7):1194–200.

[24] Metzler SD, Jaszczak RJ, Patil NH, Vemulapalli S, Akabani G, Chin BB. Molecular imaging of small animals with a triple-head SPECT system using pinhole collimation. *IEEE Trans Med Imaging*. 2005;24(7):853–62.

[25] Hesterman JY, Kupinski MA, Furenlid LR, Wilson DW, Barrett HH. The multi-module, multi-resolution system (M^3R): A novel small-animal SPECT system. *Med Phys*. 2007;34(3):987–93.

[26] van der Have F, Vastenhouw B, Ramakers RM, Branderhorst W, Krah JO, Ji C et al. U-SPECT-II: an ultra-high-resolution device for molecular small-animal imaging. *J Nucl Med*. 2009;50(4):599–605.

[27] Deleye S, Van Holen R, Verhaeghe J, Vandenberghe S, Stroobants S, Staelens S. Performance evaluation of small-animal multipinhole µSPECT scanners for mouse imaging. *Eur J Nucl Med Mol Imaging*. 2013;40(5):744–58.

[28] Bracewell RN. Strip integration in radio astronomy. *Aust J Phys*. 1956;9(2):198.

[29] Feldkamp LA, Davis LC, Kress JW. Practical cone-beam algorithm. *J Opt Soc Am A*. 1984;1(6):612–9.

[30] Lange K, Carson R. EM reconstruction algorithms for emission and transmission tomography. *J Comput Assist Tomogr*. 1984;8(2):306–16.

[31] Hudson HM, Larkin RS. Accelerated image reconstruction using ordered subsets of projection data. *IEEE Trans Med Imaging*. 1994;13(4):601–9.

[32] Branderhorst W, Vastenhouw B, Beekman FJ. Pixel-based subsets for rapid multi-pinhole SPECT reconstruction. *Phys Med Biol*. 2010;55(7):2023–34.

[33] Vastenhouw B, Beekman F. Submillimeter total-body murine imaging with U-SPECT-I. *J Nucl Med*. 2007;48(3):487–93.

[34] Goorden MC, van der Have F, Kreuger R, Beekman FJ. An efficient simulator for pinhole imaging of PET isotopes. *Phys Med Biol*. 2011;56(6):1617–34.

[35] Kreissl MC, Wu HM, Stout DB, Ladno W, Schindler TH, Zhang X et al. Noninvasive measurement of cardiovascular function in mice with high-temporal-resolution small-animal PET. *J Nucl Med*. 2006;47(6):974–80.

[36] Vastenhouw B, van der Have F, van der Linden AJA, von Oerthel L, Booij J, Burbach JPH et al. Movies of dopamine transporter occupancy with ultra-high resolution focusing pinhole SPECT. *Mol Psychiatr*. 2007;12(11):984–7.

[37] Recchia FA, Lionetti V. Animal models of dilated cardiomyopathy for translational research. *Vet Res Commun*. 2007;31 Suppl 1:35–41.

[38] Moon A. Mouse models of congenital cardiovascular disease. *Curr Top Dev Biol*. 2008;84:171–248.

[39] Franc BL, Acton PD, Mari C, Hasegawa BH. Small-animal SPECT and SPECT/CT: important tools for preclinical investigation. *J Nucl Med*. 2008;49(10):1651–63.

[40] Jaszczak RJ, Li J, Wang H, Zalutsky MR, Coleman RE. Pinhole collimation for ultra-high-resolution, small-field-of-view SPECT. *Phys Med Biol*. 1994;39(3):425–37.

[41] Ishizu K, Mukai T, Yonekura Y, Pagani M, Fujita T, Magata Y et al. Ultra-high resolution SPECT system using four pinhole collimators for small animal studies. *J Nucl Med*. 1995;36(12):2282–7.

[42] Walrand S, Jamar F, de Jong M, Pauwels S. Evaluation of novel whole-body high-resolution rodent SPECT (Linoview) based on direct acquisition of linogram projections. *J Nucl Med*. 2005;46(11):1872–80.

[43] Moore SC, Zimmerman RE, Mahmood A, Mellen R, Lim CB. A triple-detector multi-pinhole system for SPECT imaging of rodents. *J Nucl Med*. 2004;45(5):97P.

[44] Kastis GK, Barber HB, Barrett HH, Gifford HC, Pang IW, Patton DD et al. High resolution SPECT imager for three-dimensional imaging of small animals. *J Nucl Med*. 1998;39(5):9P.

[45] Liu Z, Kastis GA, Stevenson GD, Barrett HH, Furenlid LR, Kupinski MA et al. Quantitative analysis of acute myocardial infarct in rat hearts with ischemia-reperfusion using a high-resolution stationary SPECT system. *J Nucl Med*. 2002;43(7):933–9.

[46] Kupinski MA, Barrett HH, editors. Small-animal SPECT imaging. New York: Springer Science+Business Media, Inc.; 2005.

[47] Visser EP, Disselhorst JA, Brom M, Laverman P, Gotthardt M, Oyen WJG et al. Spatial resolution and sensitivity of the Inveon small-animal PET scanner. *J Nucl Med*. 2009;50(1):139–47.

[48] Yang YF, Tai YC, Siegel S, Newport DF, Bai B, Li QZ et al. Optimization and performance evaluation of the microPET II scanner for in vivo small-animal imaging. *Phys Med Biol*. 2004;49(12):2527–45.

[49] Tamaki N, Kuge Y, Tsukamoto E. The road to quantitation of regional myocardial uptake of tracer. *J Nucl Med*. 2001;42(5):780–1.

[50] Even-Sapir E, Keidar Z, Bar-Shalom R. Hybrid imaging (SPECT/CT and PET/CT)—improving the diagnostic accuracy of functional/metabolic and anatomic imaging. *Semin Nucl Med*. 2009;39(4):264–75.

[51] Seo Y, Mari C, Hasegawa BH. Technological development and advances in single-photon emission computed tomography/computed tomography. *Semin Nucl Med*. 2008;38(3):177–98.

[52] O'Connor MK, Kemp BJ. Single-photon emission computed tomography/computed tomography: basic instrumentation and innovations. *Semin Nucl Med*. 2006;36(4):258–66.

[53] Bockisch A, Freudenberg LS, Schmidt D, Kuwert T. Hybrid imaging by SPECT/CT and PET/CT: proven outcomes in cancer imaging. *Semin Nucl Med*. 2009;39(4):276–89.

[54] Tsui BM, Frey EC, LaCroix KJ, Lalush DS, McCartney WH, King MA et al. Quantitative myocardial perfusion SPECT. *J Nucl Cardiol*. 1998;5(5):507–22.

[55] Beekman FJ, de Jong HWAM, van Geloven S. Efficient fully 3-D iterative SPECT reconstruction with Monte Carlo-based scatter compensation. *IEEE Trans Med Imaging*. 2002;21(8):867–77.

[56] Zaidi H, Hasegawa B. Determination of the attenuation map in emission tomography. *J Nucl Med*. 2003;44(2):291–315.

[57] Bateman TM, Cullom SJ. Attenuation correction single-photon emission computed tomography myocardial perfusion imaging. *Semin Nucl Med*. 2005;35(1):37–51.

[58] Hwang AB, Taylor CC, VanBrocklin HF, Dae MW, Hasegawa BH. Attenuation correction of small animal SPECT images acquired with I-125-iodorotenone. *IEEE Trans Nucl Sci*. 2006;53(3):1213–20.

[59] Cherry SR. Multimodality in vivo imaging systems: Twice the power or double the trouble? *Annu Rev Biomed Eng*. 2006;8:35–62.

[60] Xiao J, de Wit TC, Staelens SG, Beekman FJ. Evaluation of 3D Monte Carlo-based scatter correction for ^{99m}Tc cardiac perfusion SPECT. *J Nucl Med*. 2006;47(10):1662–9.

[61] Xiao J, de Wit TC, Zbijewski W, Staelens SG, Beekman FJ. Evaluation of 3D Monte Carlo-based scatter correction for ^{201}Tl cardiac perfusion SPECT. *J Nucl*

Med. 2007;48(4):637–44.

[62] Hwang AB, Franc BL, Gullberg GT, Hasegawa BH. Assessment of the sources of error affecting the quantitative accuracy of SPECT imaging in small animals. *Phys Med Biol*. 2008;53(9):2233–52.

[63] Hugg JW, Uribe J, Jansen FP, Manjeshwar RM, Lai H, Pang JC et al. A small-animal microSPECT/microCT system with a stationary CZT detector ring and rotating multi-pinhole and multi-slit collimators. *J Nucl Med*. 2006;47(Suppl 1):231P.

[64] Yang YF, Rendig S, Siegel S, Newport DF, Cherry SR. Cardiac PET imaging in mice with simultaneous cardiac and respiratory gating. *Phys Med Biol*. 2005;50(13):2979–89.

[65] Vanhove C, Defrise M, Bossuyt A, Lahoutte T. Improved quantification in single-pinhole and multiple-pinhole SPECT using micro-CT information. *Eur J Nucl Med Mol Imaging*. 2009;36(7):1049–63.

[66] Wu C, Have Fvd, Vastenhouw B, Dierckx RA, Paans AM, Beekman FJ. Absolute quantitative focusing pinhole SPECT. *Fully3D*; 2009; Beijing, China.

[67] Chow PL, Stout DB, Komisopoulou E, Chatziioannou AF. A method of image registration for small animal, multi-modality imaging. *Phys Med Biol*. 2006;51(2):379–90.

[68] Loening AM, Gambhir SS. AMIDE: a free software tool for multimodality medical image analysis. *Mol Imaging*. 2003;2(3):131–7.

[69] Ji C, van der Have F, Gratama van Andel H, Ramakers R, Beekman F. Accurate coregistration between ultra-high-resolution micro-SPECT and circular cone-beam micro-CT scanners. *Int J Biomed Imaging*. 2010;2010:654506.

[70] Beekman F, Hutton BF. Multi-modality imaging on track. *Eur J Nucl Med Mol Imaging*. 2007;34(9):1410–4.

[71] MILabs. U-SPECT/CT. http://www.milabs.com/pages/preclinicalimaging/u-spectct.php. Accessed Nov 20 2009.

[72] Bioscan. NanoSPECT/CT in vivo preclinical imager. http://www.bioscan.com/molecular-imaging/nanospect-ct. Accessed Nov 20 2009.

[73] Schramm NU, Lackas C, Hoppin JW, Forrer F, de Jong M. The nanoSPECT/CT: A high-sensitivity small-animal SPECT/CT with submillimeter spatial resolution. *Eur J Nucl Med Mol Imaging*. 2006;33:S117.

[74] Schramm NU, Lackas C, Gershman B, Norenberg JP, deJong M. Improving resolution, sensitivity and applications for the NanoSPECT/CT: A high-performance SPECT/CT imager for small-animal research. *Eur J Nucl Med Mol Imaging*. 2007;34:S226–7.

[75] Acton PD, Kung HF. Small animal imaging with high resolution single photon emission tomography. *Nucl Med Biol*. 2003;30(8):889–95.

[76] Wu MC, Gao DW, Sievers RE, Lee RJ, Hasegawa BH, Dae MW. Pinhole

single-photon emission computed tomography for myocardial perfusion imaging of mice. *J Am Coll Cardiol*. 2003;42(3):576–82.

[77] Constantinesco A, Choquet P, Monassier L, Israel-Jost V, Mertz L. Assessment of left ventricular perfusion, volumes, and motion in mice using pinhole gated SPECT. *J Nucl Med*. 2005;46(6):1005–11.

[78] Lahoutte T. Monitoring left ventricular function in small animals. *J Nucl Cardiol*. 2007;14(3):371–9.

[79] Vanhove C, Lahoutte T, Defrise M, Bossuyt A, Franken PR. Reproducibility of left ventricular volume and ejection fraction measurements in rat using pinhole gated SPECT. *Eur J Nucl Med Mol Imaging*. 2005;32(2):211–20.

[80] Okada DR, Johnson G, Liu Z, Hocherman SD, Khaw BA, Okada RD. Early detection of infarct in reperfused canine myocardium using ^{99m}Tc-glucarate. *J Nucl Med*. 2004;45(4):655–64.

[81] Khaw BA, Nakazawa A, O'Donnell SM, Pak KY, Narula J. Avidity of technetium 99m glucarate for the necrotic myocardium: in vivo and in vitro assessment. *J Nucl Cardiol*. 1997;4(4):283–90.

[82] Khaw BA, Silva JD, Petrov A, Hartner W. Indium 111 antimyosin and Tc-99m glucaric acid for noninvasive identification of oncotic and apoptotic myocardial necrosis. *J Nucl Cardiol*. 2002;9(5):471–81.

[83] Johnson LL, Schofield L, Donahay T, Bouchard M, Poppas A, Haubner R. Radiolabeled arginine-glycine-aspartic acid peptides to image angiogenesis in swine model of hibernating myocardium. *JACC Cardiovasc Imaging*. 2008;1(4):500–10.

[84] Narula J, Petrov A, Pak KY, Lister BC, Khaw BA. Very early noninvasive detection of acute experimental nonreperfused myocardial infarction with ^{99m}Tc-labeled glucarate. *Circulation*. 1997;95(6):1577–84.

[85] Flotats A, Carrio I. Non-invasive in vivo imaging of myocardial apoptosis and necrosis. *Eur J Nucl Med Mol Imaging*. 2003;30(4):615–30.

[86] Ni Y, Marchal G, Yu J, Lukito G, Petre C, Wevers M et al. Localization of metalloporphyrin-induced "specific" enhancement in experimental liver tumors: comparison of magnetic resonance imaging, microangiographic, and histologic findings. *Acad Radiol*. 1995;2(8):687–99.

[87] Ni Y, Petre C, Miao Y, Yu J, Cresens E, Adriaens P et al. Magnetic resonance imaging-histomorphologic correlation studies on paramagnetic metalloporphyrins in rat models of necrosis. *Invest Radiol*. 1997;32(12):770–9.

[88] Maurer J, Strauss A, Ebert W, Bauer H, Felix R. Contrast-enhanced high resolution magnetic resonance imaging of pigmented malignant melanoma using Mn-TPPS4 and Gd-DTPA: experimental results. *Melanoma Res*. 2000;10(1):40–6.

[89] Agostinis P, Vantieghem A, Merlevede W, de Witte PA. Hypericin in cancer treatment: more light on the way. *Int J Biochem Cell Biol*. 2002;34(3):221–41.

[90] Ni Y, Huyghe D, Verbeke K, de Witte PA, Nuyts J, Mortelmans L et al. First

preclinical evaluation of mono-[^{123}I]iodohypericin as a necrosis-avid tracer agent. *Eur J Nucl Med Mol Imaging*. 2006;33(5):595–601.

[91] Fonge H, Vunckx K, Wang H, Feng Y, Mortelmans L, Nuyts J et al. Non-invasive detection and quantification of acute myocardial infarction in rabbits using mono-[^{123}I]iodohypericin microSPECT. *Eur Heart J*. 2008;29(2):260–9.

[92] Gottlieb RA, Engler RL. Apoptosis in myocardial ischemia-reperfusion. *Ann N Y Acad Sci*. 1999;874:412–26.

[93] Gottlieb RA, Burleson KO, Kloner RA, Babior BM, Engler RL. Reperfusion injury induces apoptosis in rabbit cardiomyocytes. *J Clin Invest*. 1994;94(4):1621–8.

[94] Brady NR, Hamacher-Brady A, Gottlieb RA. Proapoptotic BCL-2 family members and mitochondrial dysfunction during ischemia/reperfusion injury, a study employing cardiac HL-1 cells and GFP biosensors. *Biochim Biophys Acta*. 2006;1757(5–6):667–78.

[95] Blankenberg FG, Katsikis PD, Tait JF, Davis RE, Naumovski L, Ohtsuki K et al. In vivo detection and imaging of phosphatidylserine expression during programmed cell death. *Proc Natl Acad Sci U S A*. 1998;95(11):6349–54.

[96] Kang PM, Izumo S. Apoptosis and heart failure: A critical review of the literature. *Circ Res*. 2000;86(11):1107–13.

[97] Blankenberg F, Narula J, Strauss HW. In vivo detection of apoptotic cell death: a necessary measurement for evaluating therapy for myocarditis, ischemia, and heart failure. *J Nucl Cardiol*. 1999;6(5):531–9.

[98] Narula J, Haider N, Virmani R, DiSalvo TG, Kolodgie FD, Hajjar RJ et al. Apoptosis in myocytes in end-stage heart failure. *N Engl J Med*. 1996;335(16):1182–9.

[99] Hofstra L, Liem IH, Dumont EA, Boersma HH, van Heerde WL, Doevendans PA et al. Visualisation of cell death in vivo in patients with acute myocardial infarction. *Lancet*. 2000;356(9225):209–12.

[100] Narula J, Zaret BL. Noninvasive detection of cell death: from tracking epitaphs to counting coffins. *J Nucl Cardiol*. 2002;9(5):554–60.

[101] Fonge H, de Saint Hubert M, Vunckx K, Rattat D, Nuyts J, Bormans G et al. Preliminary in vivo evaluation of a novel ^{99m}Tc-labeled HYNIC-*cys*-annexin A5 as an apoptosis imaging agent. *Bioorg Med Chem Lett*. 2008;18(13):3794–8.

[102] Shirani J, Dilsizian V. Molecular imaging in heart failure. *Curr Opin Biotechnol*. 2007;18(1):65–72.

[103] Taki J, Higuchi T, Kawashima A, Tait JF, Kinuya S, Muramori A et al. Detection of cardiomyocyte death in a rat model of ischemia and reperfusion using ^{99m}Tc-labeled annexin V. *J Nucl Med*. 2004;45(9):1536–41.

[104] Shan D, Marchase RB, Chatham JC. Overexpression of TRPC3 increases apoptosis but not necrosis in response to ischemia-reperfusion in adult mouse cardiomyocytes. *Am J Physiol Cell Physiol*. 2008;294(3):C833–41.

[105] Boersma HH, Kietselaer BL, Stolk LM, Bennaghmouch A, Hofstra L, Narula J et al. Past, present, and future of annexin A5: from protein discovery to clinical applications. *J Nucl Med*. 2005;46(12):2035–50.

[106] Corsten MF, Reutelingsperger CP, Hofstra L. Imaging apoptosis for detecting plaque instability: rendering death a brighter facade. *Curr Opin Biotechnol*. 2007;18(1):83–9.

[107] Korngold EC, Jaffer FA, Weissleder R, Sosnovik DE. Noninvasive imaging of apoptosis in cardiovascular disease. *Heart Fail Rev*. 2008;13(2):163–73.

[108] Stodilka RZ, Blackwood KJ, Kong H, Prato FS. A method for quantitative cell tracking using SPECT for the evaluation of myocardial stem cell therapy. *Nucl Med Commun*. 2006;27(10):807–13.

[109] Jacob JL, Salis FV, Ruiz MA, Greco OT. Labeled stem cells transplantation to the myocardium of a patient with Chagas' disease. *Arq Bras Cardiol*. 2007;89(2):e10–1.

[110] Boersma HH, Tromp SC, Hofstra L, Narula J. Stem cell tracking: reversing the silence of the lambs. *J Nucl Med*. 2005;46(2):200–3.

[111] Zhou R, Thomas DH, Qiao H, Bal HS, Choi SR, Alavi A et al. In vivo detection of stem cells grafted in infarcted rat myocardium. *J Nucl Med*. 2005;46(5):816–22.

[112] Sharma AK, Dhingra S, Khaper N, Singal PK. Activation of apoptotic processes during transition from hypertrophy to heart failure in guinea pigs. *Am J Physiol Heart Circ Physiol*. 2007;293(3):H1384–90.

[113] Miyagawa M, Beyer M, Wagner B, Anton M, Spitzweg C, Gansbacher B et al. Cardiac reporter gene imaging using the human sodium/iodide symporter gene. *Cardiovasc Res*. 2005;65(1):195–202.

[114] Creemers EE, Cleutjens JP, Smits JF, Daemen MJ. Matrix metalloproteinase inhibition after myocardial infarction: a new approach to prevent heart failure? *Circ Res*. 2001;89(3):201–10.

[115] Su H, Spinale FG, Dobrucki LW, Song J, Hua J, Sweterlitsch S et al. Noninvasive targeted imaging of matrix metalloproteinase activation in a murine model of postinfarction remodeling. *Circulation*. 2005;112(20):3157–67.

[116] Jaffer FA, Sosnovik DE, Nahrendorf M, Weissleder R. Molecular imaging of myocardial infarction. *J Mol Cell Cardiol*. 2006;41(6):921–33.

[117] Zhang H, Cuevas J. sigma Receptor activation blocks potassium channels and depresses neuroexcitability in rat intracardiac neurons. *J Pharmacol Exp Ther*. 2005;313(3):1387–96.

[118] Collier TL, Waterhouse RN, Kassiou M. Imaging sigma receptors: applications in drug development. *Curr Pharm Des*. 2007;13(1):51–72.

[119] Verjans JW, Lovhaug D, Narula N, Petrov AD, Indrevoll B, Bjurgert E et al. Noninvasive imaging of angiotensin receptors after myocardial infarction. *JACC Cardiovasc Imaging*. 2008;1(3):354–62.

[120] Patel AD, Iskandrian AE. MIBG imaging. *J Nucl Cardiol*. 2002;9(1):75–94.

[121] Langer A, Freeman MR, Josse RG, Armstrong PW. Metaiodobenzylguanidine imaging in diabetes mellitus: assessment of cardiac sympathetic denervation and its relation to autonomic dysfunction and silent myocardial ischemia. *J Am Coll Cardiol*. 1995;25(3):610–8.

[122] Tomoda H, Yoshioka K, Shiina Y, Tagawa R, Ide M, Suzuki Y. Regional sympathetic denervation detected by iodine 123 metaiodobenzylguanidine in non-Q-wave myocardial infarction and unstable angina. *Am Heart J*. 1994;128(3):452–8.

[123] Samnick S, Scheuer C, Munks S, El-Gibaly AM, Menger MD, Kirsch CM. Technetium-99m labeled 1-(4-fluorobenzyl)-4-(2-mercapto-2-methyl-4-azapentyl)-4-(2-mercapto-2-methylpropylamino)-piperidine and iodine-123 metaiodobenzylguanidine for studying cardiac adrenergic function: a comparison of the uptake characteristics in vascular smooth muscle cells and neonatal cardiac myocytes, and an investigation in rats. *Nucl Med Biol*. 2004;31(4):511–22.

[124] Richter S, Schaefer A, Menger MD, Kirsch CM, Samnick S. Mapping of the cardiac sympathetic nervous system by single photon emission tomography with technetium-99m-labelled fluorobenzylpiperidine derivative (^{99m}Tc-FBPBAT): result of a feasibility study in a porcine model and an initial dosimetric estimation in humans. *Nucl Med Commun*. 2005;26(4):361–8.

[125] Choe YS, Lee KH. Targeted in vivo imaging of angiogenesis: present status and perspectives. *Curr Pharm Des*. 2007;13(1):17–31.

[126] Naghavi M, Libby P, Falk E, Casscells SW, Litovsky S, Rumberger J et al. From vulnerable plaque to vulnerable patient: a call for new definitions and risk assessment strategies: Part I. *Circulation*. 2003;108(14):1664–72.

[127] Langer HF, Haubner R, Pichler BJ, Gawaz M. Radionuclide imaging: a molecular key to the atherosclerotic plaque. *J Am Coll Cardiol*. 2008;52(1):1–12.

[128] Kolodgie FD, Petrov A, Virmani R, Narula N, Verjans JW, Weber DK et al. Targeting of apoptotic macrophages and experimental atheroma with radiolabeled annexin V: a technique with potential for noninvasive imaging of vulnerable plaque. *Circulation*. 2003;108(25):3134–9.

[129] Isobe S, Tsimikas S, Zhou J, Fujimoto S, Sarai M, Branks MJ et al. Noninvasive imaging of atherosclerotic lesions in apolipoprotein E-deficient and low-density-lipoprotein receptor-deficient mice with annexin A5. *J Nucl Med*. 2006;47(9):1497–505.

[130] Hartung D, Sarai M, Petrov A, Kolodgie F, Narula N, Verjans J et al. Resolution of apoptosis in atherosclerotic plaque by dietary modification and statin therapy. *J Nucl Med*. 2005;46(12):2051–6.

[131] Winter PM, Shukla HP, Caruthers SD, Scott MJ, Fuhrhop RW, Robertson JD et al. Molecular imaging of human thrombus with computed tomography. *Acad Radiol*. 2005;12 Suppl 1:S9–13.

[132] Iuliano L, Signore A, Vallabajosula S, Colavita AR, Camastra C, Ronga G et al. Preparation and biodistribution of 99m technetium labelled oxidized LDL in man. *Atherosclerosis*. 1996;126(1):131–41.

[133] Virgolini I, Rauscha F, Lupattelli G, Angelberger P, Ventura A, O'Grady J et al. Autologous low-density lipoprotein labelling allows characterization of human atherosclerotic lesions in vivo as to presence of foam cells and endothelial coverage. *Eur J Nucl Med*. 1991;18(12):948–51.

[134] Iuliano L, Signore A, Violi F. Uptake of oxidized LDL by human atherosclerotic plaque. *Circulation*. 1997;96(6):2093–4.

[135] Annovazzi A, Bonanno E, Arca M, D'Alessandria C, Marcoccia A, Spagnoli LG et al. ^{99m}Tc-interleukin-2 scintigraphy for the in vivo imaging of vulnerable atherosclerotic plaques. *Eur J Nucl Med Mol Imaging*. 2006;33(2):117–26.

[136] Schafers M, Riemann B, Kopka K, Breyholz HJ, Wagner S, Schafers KP et al. Scintigraphic imaging of matrix metalloproteinase activity in the arterial wall in vivo. *Circulation*. 2004;109(21):2554–9.

[137] Fujimoto S, Hartung D, Ohshima S, Edwards DS, Zhou J, Yalamanchili P et al. Molecular imaging of matrix metalloproteinase in atherosclerotic lesions: resolution with dietary modification and statin therapy. *J Am Coll Cardiol*. 2008;52(23):1847–57.

[138] Davies JR, Rudd JH, Weissberg PL, Narula J. Radionuclide imaging for the detection of inflammation in vulnerable plaques. *J Am Coll Cardiol*. 2006;47(8 Suppl):C57–68.

[139] Badea CT, Drangova M, Holdsworth DW, Johnson GA. In vivo small-animal imaging using micro-CT and digital subtraction angiography. *Phys Med Biol*. 2008;53(19):R319–50.

[140] Nahrendorf M, Badea C, Hedlund LW, Figueiredo JL, Sosnovik DE, Johnson GA et al. High-resolution imaging of murine myocardial infarction with delayed-enhancement cine micro-CT. *Am J Physiol Heart Circ Physiol*. 2007;292(6):H3172–8.

[141] Mukundan S, Jr., Ghaghada KB, Badea CT, Kao CY, Hedlund LW, Provenzale JM et al. A liposomal nanoscale contrast agent for preclinical CT in mice. *AJR Am J Roentgenol*. 2006;186(2):300–7.

[142] Rabin O, Manuel Perez J, Grimm J, Wojtkiewicz G, Weissleder R. An X-ray computed tomography imaging agent based on long-circulating bismuth sulphide nanoparticles. *Nat Mater*. 2006;5(2):118–22.

[143] Detombe SA, Ford NL, Xiang F, Lu X, Feng Q, Drangova M. Longitudinal follow-up of cardiac structure and functional changes in an infarct mouse model using retrospectively gated micro-computed tomography. *Invest Radiol*. 2008;43(7):520–9.

[144] Toyota E, Fujimoto K, Ogasawara Y, Kajita T, Shigeto F, Matsumoto T et al. Dynamic changes in three-dimensional architecture and vascular volume of

transmural coronary microvasculature between diastolic- and systolic-arrested rat hearts. *Circulation*. 2002;105(5):621–6.

[145] Li JJ, Zhu CG, Yu B, Liu YX, Yu MY. The role of inflammation in coronary artery calcification. *Ageing Res Rev*. 2007;6(4):263–70.

[146] Clarke M, Bennett M. The emerging role of vascular smooth muscle cell apoptosis in atherosclerosis and plaque stability. *Am J Nephrol*. 2006;26(6):531–5.

[147] Ritman EL, Bolander ME, Fitzpatrick LA, Turner RT. Micro-CT imaging of structure-to-function relationship of bone microstructure and associated vascular involvement. *Technol Health Care*. 1998;6(5–6):403–12.

[148] Persy V, Postnov A, Neven E, Dams G, De Broe M, D'Haese P et al. High-resolution X-ray microtomography is a sensitive method to detect vascular calcification in living rats with chronic renal failure. *Arterioscler Thromb Vasc Biol*. 2006;26(9):2110–6.

[149] Boyd HL, Gunn RN, Marinho NV, Karwatowski SP, Bailey DL, Costa DC et al. Non-invasive measurement of left ventricular volumes and function by gated positron emission tomography. *Eur J Nucl Med Mol Imaging*. 1996;23(12):1594–602.

[150] Rajappan K, Livieratos L, Camici PG, Pennell DJ. Measurement of ventricular volumes and function: a comparison of gated PET and cardiovascular magnetic resonance. *J Nucl Med*. 2002;43(6):806–10.

[151] Slart RH, Bax JJ, de Jong RM, de Boer J, Lamb HJ, Mook PH et al. Comparison of gated PET with MRI for evaluation of left ventricular function in patients with coronary artery disease. *J Nucl Med*. 2004;45(2):176–82.

[152] Slart RH, Bax JJ, van Veldhuisen DJ, van der Wall EE, Dierckx RA, Jager PL. Imaging techniques in nuclear cardiology for the assessment of myocardial viability. *Int J Cardiovasc Imaging*. 2006;22(1):63–80.

[153] Boucher L, Rodrigue S, Lecomte R, Benard F. Respiratory gating for 3-dimensional PET of the thorax: feasibility and initial results. *J Nucl Med*. 2004;45(2):214–9.

[154] Lamare F, Ledesma Carbayo MJ, Cresson T, Kontaxakis G, Santos A, Le Rest CC et al. List-mode-based reconstruction for respiratory motion correction in PET using non-rigid body transformations. *Phys Med Biol*. 2007;52(17):5187–204.

[155] Klein GJ, Reutter BW, Ho MH, Reed JH, Huesman RH. Real-time system for respiratory-cardiac gating in positron tomography. *IEEE Trans Nucl Sci*. 1998;45(4):2139–43.

[156] Livieratos L, Rajappan K, Stegger L, Schafers K, Bailey DL, Camici PG. Respiratory gating of cardiac PET data in list-mode acquisition. *Eur J Nucl Med Mol Imaging*. 2006;33(5):584–8.

[157] Martinez-Moller A, Zikic D, Botnar RM, Bundschuh RA, Howe W, Ziegler SI et al. Dual cardiac-respiratory gated PET: implementation and results from a feasibility study. *Eur J Nucl Med Mol Imaging*. 2007;34(9):1447–54.

[158] Buther F, Dawood M, Stegger L, Wubbeling F, Schafers M, Schober O et al. List mode-driven cardiac and respiratory gating in PET. *J Nucl Med*. 2009;50(5):674–81.

[159] Gigengack F, Ruthotto L, Burger M, Wolters CH, Jiang XY, Schafers KP. Motion correction in dual gated cardiac PET using mass-preserving image registration. *IEEE Trans Med Imaging*. 2012;31(3):698–712.

[160] Goetz C, Monassier L, Choquet P, Constantinesco A. Assessment of right and left ventricular function in healthy mice by blood-pool pinhole gated SPECT. *C R Biol*. 2008;331(9):637–47.

[161] de Kemp RA, Epstein FH, Catana C, Tsui BM, Ritman EL. Small-animal molecular imaging methods. *J Nucl Med*. 2010;51(Suppl):18S–32S.

[162] Golestani R, Wu C, Tio RA, Zeebregts CJ, Petrov AD, Beekman FJ et al. Small-animal SPECT and SPECT/CT: application in cardiovascular research. *Eur J Nucl Med Mol Imaging*. 2010;37(9):1766–77.

[163] Strydhorst JH, Leenen FH, Ruddy TD, Wells RG. Reproducibility of serial left ventricle perfusion, volume, and ejection fraction measurements using multiplexed multipinhole SPECT in healthy rats and rats after myocardial infarction. *J Nucl Med*. 2011;52(8):1285–92.

[164] Goethals LR, De Geeter F, Vanhove C, Roosens B, Devos H, Lahoutte T. Improved quantification in pinhole gated myocardial perfusion SPECT using micro-CT and ultrasound information. *Contrast Media Mol Imaging*. 2012;7(2):167–74.

[165] Vera P, Manrique A, Pontvianne V, Hitzel A, Koning R, Cribier A. Thallium-gated SPECT in patients with major myocardial infarction: Effect of filtering and zooming in comparison with equilibrium radionuclide imaging and left ventriculography. *J Nucl Med*. 1999;40(4):513–21.

[166] Wright GA, McDade M, Martin W, Hutton I. Quantitative gated SPECT: the effect of reconstruction filter on calculated left ventricular ejection fractions and volumes. *Phys Med Biol*. 2002;47(8):N99–105.

[167] Pai M, Yang YJ, Im KC, Hong IK, Yun SC, Kang DH et al. Factors affecting accuracy of ventricular volume and ejection fraction measured by gated Tl-201 myocardial perfusion single photon emission computed tomography. *Int J Cardiovasc Imaging*. 2006;22(5):671–81.

[168] Kakhki VRD, Sadeghi R. Gated myocardial perfusion SPECT in patients with a small heart: Effect of zooming and filtering. *Clin Nucl Med*. 2007;32(5):404–6.

[169] Lavender FM, Meades RT, Al-Nahhas A, Nijran KS. Factors affecting the measurement of left ventricular ejection fraction in myocardial perfusion imaging. *Nucl Med Commun*. 2009;30(5):350–5.

[170] Berman D, Germano G, Lewin H, Kang XP, Kavanagh PB, Tapnio P et al. Comparison of post-stress ejection fraction and relative left ventricular volumes by automatic analysis of gated myocardial perfusion single-photon emission

computed tomography acquired in the supine and prone positions. *J Nucl Cardiol*. 1998;5(1):40–7.

[171] Schaefer WM, Lipke CS, Kuhl HP, Koch KC, Kaiser HJ, Reinartz P et al. Prone versus supine patient positioning during gated ^{99m}Tc-sestamibi SPECT: effect on left ventricular volumes, ejection fraction, and heart rate. *J Nucl Med*. 2004;45(12):2016–20.

[172] Yap K, Campbell P, Cherk M, McGrath C, Kalff V. Effect of prone versus supine positioning on left ventricular ejection fraction (LVEF) and heart rate using ECG gated Tl-201 myocardial perfusion scans and gated cardiac blood pool scans. *J Med Imaging Radiat Oncol*. 2012;56(5):525–31.

[173] Klein S, Staring M, Murphy K, Viergever MA, Pluim JP. elastix: a toolbox for intensity-based medical image registration. *IEEE Trans Med Imaging*. 2010;29(1):196–205.

[174] Rentmeester MCM, van der Have F, Beekman FJ. Optimizing multi-pinhole SPECT geometries using an analytical model. *Phys Med Biol*. 2007;52(9):2567–81.

[175] Beekman FJ, Kamphuis C, Hutton BF, van Rijk PP. Half-fanbeam collimators combined with scanning point sources for simultaneous emission-transmission imaging. *J Nucl Med*. 1998;39(11):1996–2003.

[176] Kaplan MS, Haynor DR, Vija H. A differential attenuation method for simultaneous estimation of SPECT activity and attenuation distributions. *IEEE Trans Nucl Sci*. 1999;46(3):535–41.

[177] El Fakhri G, Buvat I, Benali H, Todd-Pokropek A, Di Paola R. Relative impact of scatter, collimator response, attenuation, and finite spatial resolution corrections in cardiac SPECT. *J Nucl Med*. 2000;41(8):1400–8.

[178] King M, Farncombe T. An overview of attenuation and scatter correction of planar and SPECT data for dosimetry studies. *Cancer Biother Radiopharm*. 2003;18(2):181–90.

[179] de Jong HWAM, Beekman FJ. Rapid SPECT simulation of downscatter in non-uniform media. *Phys Med Biol*. 2001;46(3):621–35.

[180] de Jong HW, Beekman FJ, Viergever MA, van Rijk PP. Simultaneous ^{99m}Tc/^{201}Tl dual-isotope SPET with Monte Carlo-based down-scatter correction. *Eur J Nucl Med Mol Imaging*. 2002;29(8):1063–71.

[181] de Wit TC, Xiao J, Nijsen JF, van het Schip FD, Staelens SG, van Rijk PP et al. Hybrid scatter correction applied to quantitative holmium-166 SPECT. *Phys Med Biol*. 2006;51(19):4773–87.

[182] Schillaci O. Hybrid SPECT/CT: a new era for SPECT imaging? *Eur J Nucl Med Mol Imaging*. 2005;32(5):521–4.

[183] Hwang AB, Hasegawa BH. Attenuation correction for small animal SPECT imaging using x-ray CT data. *Med Phys*. 2005;32(9):2799–804.

[184] Chang LT. A method for attenuation correction in radionuclide computed

tomography. *IEEE Trans Nucl Sci*. 1978;25(1):638–43.

[185] Beekman FJ, Vastenhouw B. Design and simulation of a high-resolution stationary SPECT system for small animals. *Phys Med Biol*. 2004;49(19):4579–92.

[186] Blanckaert P, Burvenich I, Staelens S, De Bruyne S, Moerman L, Wyffels L et al. Effect of cyclosporin A administration on the biodistribution and multipinhole μSPECT imaging of [^{123}I]R91150 in rodent brain. *Eur J Nucl Med Mol Imaging*. 2009;36(3):446–53.

[187] van der Have F, Vastenhouw B, Rentmeester M, Beekman FJ. System calibration and statistical image reconstruction for ultra-high resolution stationary pinhole SPECT. *IEEE Trans Med Imaging*. 2008;27(7):960–71.

[188] Ogawa K, Harata Y, Ichihara T, Kubo A, Hashimoto S. A practical method for position-dependent Compton-scatter correction in single photon emission CT. *IEEE Trans Med Imaging*. 1991;10(3):408–12.

[189] Bowsher JE, Johnson VE, Turkington TG, Jaszczak RJ, Floyd CE, Coleman RE. Bayesian reconstruction and use of anatomical a priori information for emission tomography. *IEEE Trans Med Imaging*. 1996;15(5):673–86.

[190] van der Have F, Beekman FJ. Photon penetration and scatter in micro-pinhole imaging: a Monte Carlo investigation. *Phys Med Biol*. 2004;49(8):1369–86.

[191] van der Have F, Beekman FJ. Penetration, scatter and sensitivity in channel micro-pinholes for SPECT: A Monte Carlo investigation. *IEEE Trans Nucl Sci*. 2006;53(5):2635–45.

[192] Hoang B, Lee H, Reilly RM, Allen C. Noninvasive monitoring of the fate of ^{111}In-labeled block copolymer micelles by high resolution and high sensitivity microSPECT/CT imaging. *Mol Pharm*. 2009;6(2):581–92.

[193] Chen CL, Wang Y, Lee JJ, Tsui BM. Toward quantitative small animal pinhole SPECT: assessment of quantitation accuracy prior to image compensations. *Mol Imaging Biol*. 2009;11(3):195–203.

[194] Gullberg GT, Huesman RH, Malko JA, Pelc NJ, Budinger TF. An attenuated projector-backprojector for iterative SPECT reconstruction. *Phys Med Biol*. 1985;30(8):799–816.

[195] Wu C, van der Have F, Vastenhouw B, Dierckx RA, Paans AM, Beekman FJ. Absolute quantitative total-body small-animal SPECT with focusing pinholes. *Eur J Nucl Med Mol Imaging*. 2010;37(11):2127–35.

[196] Hutton BF, Buvat I, Beekman FJ. Review and current status of SPECT scatter correction. *Phys Med Biol*. 2011;56(14):R85–112.

[197] Staelens SG, de Wit TC, Lemahieu IA, Beekman FJ. Degradation of myocardial perfusion SPECT images caused by contaminants in thallous (^{201}Tl) chloride. *Eur J Nucl Med Mol Imaging*. 2008;35(5):922–32.

[198] LaCroix KJ, Tsui BMW, Hasegawa BH, Brown JK. Investigation of the use of X-ray CT images for attenuation compensation in SPECT. *IEEE Trans Nucl Sci*. 1994;41(6):2793–9.

[199] Chantler CT. Detailed tabulation of atomic form factors, photoelectric absorption and scattering cross section, and mass attenuation coefficients in the vicinity of absorption edges in the soft X-ray ($Z = 30–36$, $Z = 60–89$, $E = 0.1–10$ keV)—addressing convergence issues of earlier work. *J Synchrotron Radiat*. 2001;8(4):1124.

[200] Kagadis GC, Loudos G, Katsanos K, Langer SG, Nikiforidis GC. In vivo small animal imaging: current status and future prospects. *Med Phys*. 2010;37(12):6421–42.

[201] Vaneycken I, Devoogdt N, Van Gassen N, Vincke C, Xavier C, Wernery U et al. Preclinical screening of anti-HER2 nanobodies for molecular imaging of breast cancer. *FASEB J*. 2011;25(7):2433–46.

[202] Vegt E, Melis M, Eek A, de Visser M, Brom M, Oyen WJG et al. Renal uptake of different radiolabelled peptides is mediated by megalin: SPECT and biodistribution studies in megalin-deficient mice. *Eur J Nucl Med Mol Imaging*. 2011;38(4):623–32.

[203] Umeda IO, Tani K, Tsuda K, Kobayashi M, Ogata M, Kimura S et al. High resolution SPECT imaging for visualization of intratumoral heterogeneity using a SPECT/CT scanner dedicated for small animal imaging. *Ann Nucl Med*. 2012;26(1):67–76.

[204] Wu C, de Jong JR, Gratama van Andel HA, van der Have F, Vastenhouw B, Laverman P et al. Quantitative multi-pinhole small-animal SPECT: uniform versus non-uniform Chang attenuation correction. *Phys Med Biol*. 2011;56(18):N183–93.

[205] Tonge CM, Manoharan M, Lawson RS, Shields RA, Prescott MC. Attenuation correction of myocardial SPECT studies using low resolution computed tomography images. *Nucl Med Commun*. 2005;26(3):231–7.

[206] Tonge CM, Ellul G, Pandit M, Lawson RS, Shields RA, Arumugam P et al. The value of registration correction in the attenuation correction of myocardial SPECT studies using low resolution computed tomography images. *Nucl Med Commun*. 2006;27(11):843–52.

[207] Goetze S, Brown TL, Lavely WC, Zhang Z, Bengel FM. Attenuation correction in myocardial perfusion SPECT/CT: effects of misregistration and value of reregistration. *J Nucl Med*. 2007;48(7):1090–5.

[208] Kennedy JA, Israel O, Frenkel A. Directions and magnitudes of misregistration of CT attenuation-corrected myocardial perfusion studies: incidence, impact on image quality, and guidance for reregistration. *J Nucl Med*. 2009;50(9):1471–8.

[209] Tsui BM, Kraitchman DL. Recent advances in small-animal cardiovascular imaging. *J Nucl Med*. 2009;50(5):667–70.

[210] Wyckhuys T, Staelens S, Van Nieuwenhuyse B, Deleye S, Hallez H, Vonck K et al. Hippocampal deep brain stimulation induces decreased rCBF in the hippocampal formation of the rat. *Neuroimage*. 2010;52(1):55–61.

[211] Branderhorst W, Vastenhouw B, van der Have F, Blezer EL, Bleeker WK,

Beekman FJ. Targeted multi-pinhole SPECT. *Eur J Nucl Med Mol Imaging*. 2011;38(3):552–61.

[212] Visser EP, Harteveld AA, Meeuwis APW, Disselhorst JA, Beekman FJ, Oyen WJG et al. Image quality phantom and parameters for high spatial resolution small-animal SPECT. *Nucl Instrum Meth A*. 2011;654(1):539–45.

[213] Brown S, Bailey DL, Willowson K, Baldock C. Investigation of the relationship between linear attenuation coefficients and CT Hounsfield units using radionuclides for SPECT. *Appl Radiat Isot*. 2008;66(9):1206–12.

[214] Ay MR, Shirmohammad M, Sarkar S, Rahmim A, Zaidi H. Comparative assessment of energy-mapping approaches in CT-based attenuation correction for PET. *Mol Imaging Biol*. 2011;13(1):187–98.

[215] Vaissier PE, Goorden MC, Vastenhouw B, van der Have F, Ramakers RM, Beekman FJ. Fast spiral SPECT with stationary gamma-cameras and focusing pinholes. *J Nucl Med*. 2012;53(8):1292–9.

[216] Wu C, Beekman FJ. Histogram-based small-animal CT calibration with evaluation for quantitative micro-SPECT. *IEEE NSS/MIC/RTSD*; 2012; Anaheim, CA, USA.

Acknowledgments

It is a challenge to finish a PhD project. It would have been impossible for me to reach this final chapter of my thesis without help from other people. Therefore, I would like to express my gratitude towards all of you who turned this thesis into reality.

First and foremost, I would like to thank Prof. Freek Beekman for giving me the opportunity to conduct this PhD project. I am indebted to you for your guidance, insightful advice and encouragement. I would also like to thank Prof. Rudi Dierckx for letting me join the research group. The thesis would not have existed without your priceless support, suggestions and comments. I would also like to mention my daily supervisor, Dr. Johan de Jong, who has always encouraged his students to develop their ideas. I am deeply grateful for your invaluable help with the article and presentation preparations.

I would like to thank the members of the Reading Committee, Prof. Anne Paans, Prof. Ronald Boellaard and Prof. Marion de Jong, for spending time in reading and approving my thesis. Anne, you also helped me a lot at the beginning of my stay in Groningen, which made my start here quite smooth.

I would also like to thank Dr. Frans van der Have, Dr. Brendan Vastenhouw, Dr. Hugo Gratama van Andel and Dr. Erik Maddox. I have learnt much from your working enthusiasm, creative thinking and meticulous scholarship. I benefited from your experience and practical advice both in carrying out experiments and in understanding the theories underlying them. I would also like to express my appreciation to Dr. Marlies Goorden and Pieter Vaissier, for those profound discussions on research questions, results and manuscripts.

I also greatly appreciate the help from Dr. Riemer Slart in nuclear cardiology, and the collaboration with Reza in my first journal article. I would also like to mention Dr. Aren van Waarde for his invaluable assistance in drafting and correcting manuscripts. I really appreciate your help.

In the course of my appreciation for Woutjan, I recollect clearly the days when we attended the Fully3D meeting together. We have shared memories of sights, performances and food in Beijing, China. I would also like to thank Marc, my roommate at the time when we joined the IEEE MIC congress. I was so glad that you liked the Chinese movie we watched. I would especially like to thank you for introducing me to “The Book” four months ago which made it much easier to produce this book.

I would like to thank Dr. Antoon Willemsen, Roel, Sergiy, Marcel, Noortje and Mehrsima by mentioning that although physicists seems to be only a minority, we perform a vital role in the department! Jurgen, Ruud and Inge, I could not have participated in animal studies without your animal expertise and precise operation. A separate note of appreciation is for Klaas Willem, for your technical support in all kind of computer issues. I would also like to express my gratitude to Annie van Zanten, Ineke ten Have and Sarita

Evers for your friendliness and guidance, in helping me with all the papers and formalities.

My sincere thanks should be given to all my office mates: Vladimir, Siddesh, Khayum, Soumen, Shiva, Willem Jan, Andrea… all of you together made a very pleasant working atmosphere. I cannot forget those evenings and nights in the office working, resting and chatting with you. I also admire my neighbours: Valentina, Leila, Inês, Anna, Nisha, Nathalie, Zilin… for all the “positive energy” and happiness that you brought in, especially those from the “girls’ room”.

Big thanks to the entire NGMB department of UMCG, Section RD&M of TU Delft and MILabs. I am also grateful to GSMS, UMCG, RuG and MILabs for financial support.

“Last but not least”, I would like to thank all my Chinese friends and friends’ friends and family I met here, especially 考博士+考博士’s+考博士’s’s，小铮铮，小赵，N(ature)B强，毛博士 et al. Let us 更加紧密的团结在以考博士为核心的某神教周围，创造机会再聚首涮火锅……

To my dear beloved 小畅畅, you entered my life in my most difficult time and warmed my heart with your concern, kindness and smile. You showed me a lot of your consideration and support for the needs in my research and work. Thank you so much for everything you have done for me.

最后，最真挚的感谢我亲爱的父母。没有你们就没有我的生命，以及我曾经和将要经历的一切。谢谢你们给与我的所有无私的亲情，无论是理解，支持，担心还是关爱。谢谢你们。

Chao Wu 吴 超
26 July 2013 2013 年 7 月 26 日

Publications

Peer-reviewed international journal articles:

- **Wu C**, Vaissier PEB, Vastenhouw B, de Jong JR, Slart RHJA, Beekman FJ. Influence of respiratory gating and image filtering on high-resolution ECG-gated murine cardiac SPECT. *submitted*.

- **Wu C**, Gratama van Andel HA, Laverman P, Boerman OC, Beekman FJ. Effects of attenuation map accuracy on attenuation-corrected micro-SPECT images. *EJNMMI Res.* 2013;3(1):7.

- **Wu C**, de Jong JR, Gratama van Andel HA, van der Have F, Vastenhouw B, Laverman P et al. Quantitative multi-pinhole small-animal SPECT: uniform versus non-uniform Chang attenuation correction. *Phys Med Biol.* 2011;56(18):N183–93.

- **Wu C**, van der Have F, Vastenhouw B, Dierckx RA, Paans AM, Beekman FJ. Absolute quantitative total-body small-animal SPECT with focusing pinholes. *Eur J Nucl Med Mol Imaging.* 2010;37(11):2127–35.

- Golestani R[*], **Wu C**[*], Tio RA, Zeebregts CJ, Petrov AD, Beekman FJ et al. Small-animal SPECT and SPECT/CT: application in cardiovascular research. *Eur J Nucl Med Mol Imaging.* 2010;37(9):1766–77.
  [*] Authors contributed equally.

Abstracts and conference papers:

- **Wu C**, Vastenhouw B, Vaissier PEB, de Jong JR, Slart RHJA, Beekman FJ. Influence of respiratory gating, image filtering and animal positioning on high-resolution ECG-gated murine cardiac SPECT. *EANM*; 2013; Lyon, France.

- **Wu C**, Beekman FJ. Histogram-based small-animal CT calibration with evaluation for quantitative micro-SPECT. *IEEE NSS/MIC/RTSD*; 2012; Anaheim, CA, USA.

- **Wu C**, Laverman P, Boerman OC, Beekman FJ. Effects of attenuation map inaccuracies on quantitative micro-SPECT. *WMIC*; 2012; Dublin, Ireland.

- **Wu C**, Vastenhouw B, de Jong JR, Dierckx RAJO, Beekman FJ. Dual-gated cardiac SPECT imaging in mice. *IEEE NSS/MIC/RTSD*; 2011; Valencia, Spain.

- **Wu C**, de Jong JR, Gratama van Andel HA, van der Have F, Vastenhouw B, Laverman P et al. Evaluation of CT-based attenuation correction for small-animal SPECT in rats. *IEEE NSS/MIC/RTSD*; 2011; Valencia, Spain.

- **Wu C**, de Jong JR, Gratama van Andel HA, van der Have F, Vastenhouw B, Laverman P et al. Chang-based attenuation correction in small-animal SPECT/CT. *EMIM*; 2011; Leiden, the Netherlands.

- **Wu C**, de Jong JR, Terwisscha van Scheltinga A, Sijbesma JWA, Lub-de Hooge MN, Dierckx RAJO et al. Molecular imaging in mice using a MILabs U-SPECT-II camera. *EANM*; 2010; Vienna, Austria.

- **Wu C**, van der Have F, de Jong JR, Dierckx RAJO, Paans AMJ, Beekman FJ. Contour-based attenuation correction for multi-pinhole SPECT. *EANM*; 2010; Vienna, Austria.

- **Wu C**, van der Have F, Vastenhouw B, Dierckx RA, Paans AM, Beekman FJ. Absolute quantitative focusing pinhole SPECT. *Fully3D*; 2009; Beijing, China.

- **Wu C**, Vastenhouw B, van der Have F, Dierckx RA, Beekman FJ. High-resolution cardiac rat SPECT: Effect of dose and acquisition time. *IEEE NSS/MIC*; 2008; Dresden, Germany.

Curriculum vitae

Chao Wu (Chinese: 吴超) (Yichang, China, 1982) graduated from secondary school in 2000 and obtained a MSc degree in Information and Communication Engineering at Tsinghua University (Beijing, China) in 2007. He performed his graduation project in Department of Electronic Engineering, where he worked on large-image compression algorithms for hardware implementation in the group of Prof. Li Zhang. Right after obtaining his degree, he went to the Netherlands and started his PhD research on quantitative multi-pinhole SPECT under supervision of Prof. Freek Beekman and Prof. Rudi Dierckx at Department of Nuclear Medicine and Molecular Imaging, University Medical Center Groningen, University of Groningen. In February 2012 he started as a post-doctoral researcher at Delft University of Technology, and also works on scientific software development in MILabs B.V. (Utrecht) from 2013.